UNIVERSITAT DE BARCELONA

Dynamics of the late-winter ENSO teleconnection to the North Atlantic-European region

Bianca Mezzina

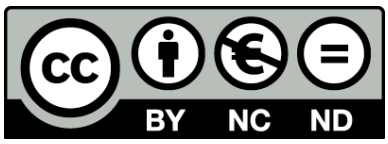

PhD Thesis

Dynamics of the late-winter ENSO teleconnection to the North Atlantic-European region

Author:
Bianca Mezzina

Advisors:
Javier García Serrano
Ileana Bladé Mendoza

Universitat de Barcelona

Dynamics of the late-winter ENSO teleconnection to the North Atlantic-European region

Programa de doctorado en física

Autora:
Bianca Mezzina

Directores:
Javier García Serrano
Ileana Bladé Mendoza

Tutor:
Alberto Manrique Oliva

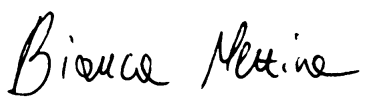

The search for knowledge is not nourished by certainty: it is nourished by a radical absence of certainty. Thanks to the acute awareness of our ignorance, we are open to doubt and can continue to learn and to learn better.

– C. Rovelli, *Helgoland*

Summary

The El Niño-Southern Oscillation (ENSO) is a natural mode of climate variability in the tropical Pacific, which not only perturbs the local atmosphere, but whose impacts can also reach remote, extra-tropical regions through atmospheric teleconnections. While the atmospheric response to ENSO and the dynamics of its teleconnections are well assessed in certain locations, such as the North Pacific-American sector, it is not the case for the North Atlantic-European (NAE) sector. The NAE region is largely dominated by internal variability: detecting an ENSO-forced signal, even if small, in this domain, and properly capturing the pathways of the ENSO-NAE teleconnection in general circulation models is important to potentially improve seasonal predictions. To do so, it is first essential to fully understand the driving mechanisms of the ENSO-NAE teleconnection. In this thesis, the dynamics of this teleconnection are assessed in late winter (January–March), the season in which a significant and robust ENSO-related signal has been reported in the literature.

Part of this well-known late-winter ENSO signal is a sea-level pressure (SLP) dipole in the North Atlantic. It is assessed that this "canonical" dipole is mostly driven by tropospheric dynamics and is related to the large-scale Rossby wave train triggered from the tropical Pacific by the anomalous upper-level divergence associated with ENSO. The wave train crosses the North Pacific, bends over North America/Canada and finally reaches the western North Atlantic, projecting onto the mid-latitude lobe of the "canonical" SLP dipole with a vertical structure that tilts westward with height.

The "canonical" SLP dipole is known to be reminiscent of the surface signature of the North Atlantic Oscillation (NAO), which is the dominant mode of variability in the North Atlantic. The relationship between the ENSO-forced response in the NAE region and the NAO is then examined using observations and SST-forced atmospheric simulations, and by considering both the linear

component of the ENSO teleconnection (linear regressions) and the two phases of ENSO (El Niño and La Niña) separately. It is found that no further similarities are evident apart from the surface SLP signature, and it is suggested that ENSO and the NAO are largely unrelated.

Another issue tackled in this thesis is the (a)symmetry of the atmospheric signal associated with El Niño and La Niña, which show roughly opposite patterns of sea surface temperature (SST) anomalies in the tropical Pacific but not necessarily a symmetric atmospheric response. Using a set of sensitivity experiments with anomalous SSTs that represent symmetric El Niño- and La Niña-like forcings, it is noticed that in three state-of-the-art models the extra-tropical response in the troposphere is slightly asymmetric in amplitude and longitudinal location. However, it is highlighted that the mechanisms at play, in particular concerning the response in the NAE region, are the same for El Niño and La Niña.

The ENSO impact on the Northern Hemisphere polar stratosphere is also studied, since a stratospheric pathway of the ENSO-NAE teleconnection has been suggested in the literature, and an ENSO signal in the polar stratosphere has been previously reported. In the same set of experiments with symmetric El Niño- and La Niña-like forcing, it is assessed that, similarly to the troposphere, the stratospheric response to La Niña is symmetric in structure to that of El Niño, but with smaller amplitude. This response is found in both the lower and middle-upper stratosphere and is suggested to be related to the upward propagation of the ENSO-forced tropospheric Rossby wave train, and specifically to its center of action located over North America/Canada. In the middle-upper stratosphere, the anomalies project onto a wavenumber-1 pattern and show a westward tilt with height that indicates upward wave propagation rather than wave-breaking, as previously suggested.

Finally, it is noticed that the well-established "canonical" dipole is mostly located over the North Atlantic, while less is known about the ENSO signal over the European continent. A novel ray-tracing approach that considers zonal asymmetries in the background flow is developed to examine potential tropospheric pathways of the ENSO teleconnection to Europe in coupled historical simulations and observations. In some cases, a SLP pattern featuring a single anomaly over Europe is present, which appears to be linked to the ENSO wave train emanated from the tropical Pacific via a split over northern North America or via reflection due to zonal inhomogeneities in the background flow. Alternatively, a wave-like pattern with two opposite-signed SLP anomalies over Europe is observed, which is suggested to be related to a secondary wave train emerging from the tropical Atlantic.

Contents

Chapter 1

Introduction

Seasonal prediction aims at estimating the average climate conditions during the following months and essentially relies on the influence of slowly-varying boundary conditions on the atmosphere. Sea surface temperatures (SSTs), in particular, represent a major source of seasonal predictability. When we talk about SSTs, we cannot but think of the El Niño-Southern Oscillation (ENSO), as it constitutes the primary mode of SST variability – and of interannual climate variability in general. Despite occurring in the tropical Pacific, ENSO's atmospheric influence extends well beyond that region through so-called *teleconnections*, which can reach the extra-tropics up to the North Atlantic-European (NAE) region. Understanding the mechanisms driving the ENSO-NAE teleconnection is crucial for the feasibility of reliable seasonal predictions in this sector and is the main objective of this thesis.

1.1 A brief review of ENSO and its teleconnections

1.1.1 ENSO basics

ENSO is usually described as a coupled ocean-atmosphere oscillation that occurs naturally in the tropical Pacific region. While not an oscillation in the strict sense, it can be viewed as a fluctuation between two extreme phases about a neutral state.

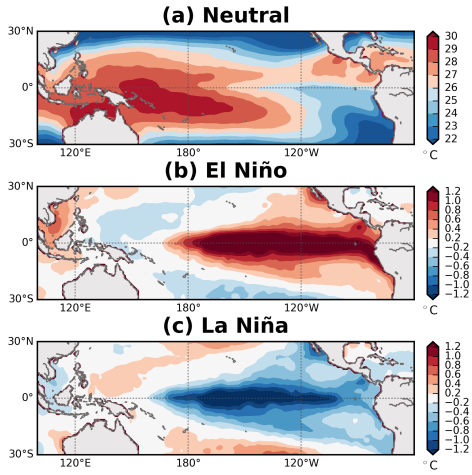

Figure 1.1: (a) SST average during neutral ENSO years; composite of SST anomalies for (b) El Niño and (c) La Niña years. HadISST (Titchner and Rayner 2014), 1901–2014, December-February. Years selected according to ±1 standard deviation of the Niño3.4 index.

Even under neutral conditions, the SST pattern in the tropical Pacific is not zonally symmetric, since colder waters are usually found towards the eastern part of the basin, compared to a warmer pool located in the western part (Fig. 1.1a). This longitudinal SST gradient is accompanied with a sea-level pressure (SLP) high over the eastern tropical Pacific and a SLP low over the warm pool, while westward trade winds blow at surface (Fig. 1.2a). Rising motions associated with the low pressure and buoyant air yield convection and upper-level divergence at the tropopause over the Maritime Continent and north-eastern Australia, while sinking air over the eastern Pacific is associated with upper-level convergence. The mean zonal flow at upper levels is eastward, hence opposite with respect to the surface, and closes the large-scale east-west cell known as the Walker circulation.

Once every 2–5 years, the SST pattern roughly reverses: the usually cold waters over the eastern tropical Pacific are replaced by an anomalous tongue of warm water extending from South America to the central tropical Pacific, and the iconic signature in the SST anomalies reveals that an El Niño event

is developing (Fig. 1.1b). The Walker circulation is perturbed accordingly, and its upward branch shifts from the western to the central tropical Pacific, where anomalous upper-level divergence is now found, as well as increased convection and precipitation (Fig. 1.2b). At surface, the trade winds weaken – or even reverse – and the SLP pattern is also disrupted, with anomalous low pressure prevailing in the central tropical Pacific. Other times, a La Niña event sets up instead, whereby an opposite pattern of SST anomalies dominates the tropical Pacific (Fig. 1.1c). The associated atmospheric response is essentially a reinforcement of the circulation during neutral conditions, with stronger trade winds at surface and increased upper-level divergence (convergence) over the western (eastern) part of the basin (Fig. 1.2c).

Although the ultimate mechanisms triggering El Niño or La Niña events are still not entirely clear (e.g. Timmermann et al. 2018), the first anomalies typically develop during summer, and the mature stage is reached between November and January, but the anomalous conditions can persist for more than a year.

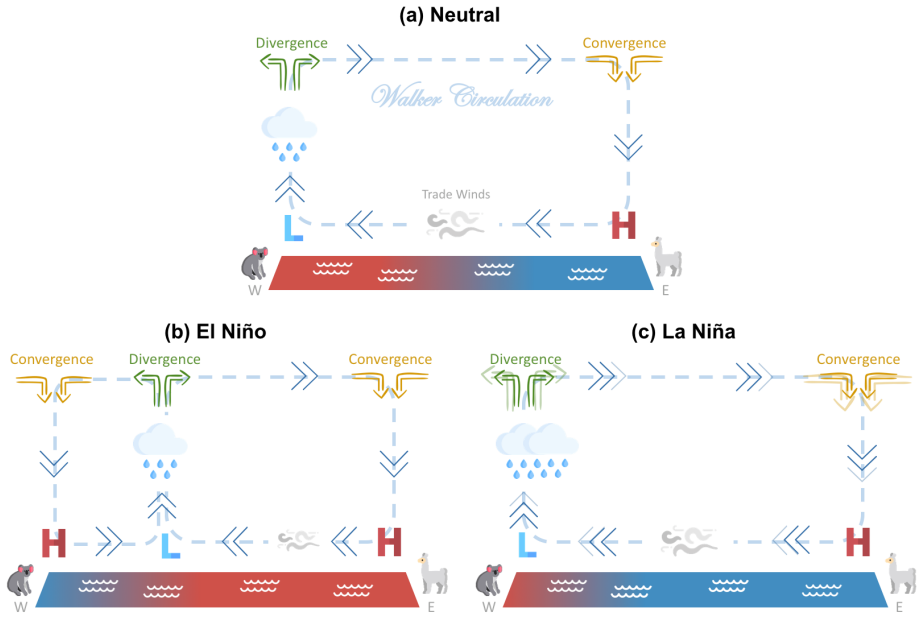

Figure 1.2: Schematic view of the atmospheric circulation associated with ENSO.

The distribution and intensity of the SST anomalies and the local atmospheric response can vary significantly from one event to the other, which contributes to the challenge of isolating a robust and significant extra-tropical signal associated with ENSO. Several ENSO "flavors" have been identified, dependent on the longitude of the SST anomaly peak (see Capotondi et al. 2015 for a review), but in this thesis the focus is on the conventional eastern Pacific (EP) ENSO, with a typical distribution of the SST anomalies as shown in Fig. 1.1.

1.1.2 ENSO teleconnections: the main wave train

A pillar of our understating of the ENSO extra-tropical teleconnection is the large-scale Rossby wave train first described theoretically by Hoskins and Karoly (1981) and in observations by Horel and Wallace (1981). Its structure consists of three anomalous centers of action in the upper-tropospheric circulation, of alternating sign and with a characteristic curved path (Fig. 1.3). The first center, a cyclone in the case of El Niño, is located over the North Pacific and reinforces the climatological Aleutian Low in the middle-lower troposphere. The perturbation then propagates northward and eastward, and the following anomaly is found roughly over Canada, an anticyclone in the case of El Niño. The wave train finally bends equatorward and its tail, again a cyclone, is located at the edge between North America and the North Atlantic Ocean. Accordingly, the North Pacific jet is strengthened and shifted southward, while the North Atlantic jet is only affected at its entrance.

The overall, barotropic wave train structure is reminiscent of the Pacific-North America pattern, but the two have been shown to be distinct (see Nigam and Baxter 2015 for a review), and while the Tropical-Northern Hemisphere pattern has also been invoked to describe the wave train (e.g. Trenberth et al. 1998), hereafter this response will be referred to as just "the main wave train". Furthermore, this main wave train is considered here to be the extra-tropical response only, i.e. roughly north of 30°N, since it is not clearly related to the pair of subtropical anticyclones – in the case of El Niño – that are part of the baroclinic Gill–Matsuno response to the tropical heating, and that are driven by different mechanisms. The main wave train can be observed in the monthly/seasonal mean soon after the SST peak in the tropical Pacific but is fully established only from January onward (e.g. Bladé et al. 2008, King et al. 2018) and persists until spring.

The fundamental trigger of the main wave train are the upper-level divergence anomalies associated with ENSO in the tropical Pacific (see previous section), which perturb the climatological vorticity field. The dynamics of the main wave

train can be approximately described as:

$$\frac{d(\zeta + f)}{dt} = S \tag{1.1}$$

Where $\zeta = \frac{\partial v}{\partial x} - \frac{\partial u}{\partial y}$ is the vertical component of the relative vorticity and $f = 2\Omega \sin \phi$ is the Coriolis parameter or planetary vorticity. The left-hand side represents the material derivative of the absolute vorticity $(\zeta + f)$, and describes the propagation of barotropic, horizontal Rossby waves. On the right-hand side, S is a generic source term that can be defined using different levels of complexity to try to encapsulate the effective Rossby wave forcing, which in the simplest case features only a simplified stretching term $-fD$, where D is the divergence (e.g. Sardeshmukh and Hoskins 1988).

The main wave train associated with La Niña exhibits roughly the same structure, with opposite-signed centers of action (positive–negative–positive), but since the anomalies in the upper-level divergence over the tropical Pacific are not symmetric between the two phases (*cf.* Fig. 1.2b and c), it can be expected that the extra-tropical response is not fully symmetric either (e.g. Hoerling et al. 2001), a topic that will be addressed in Chapters 3 and 4.

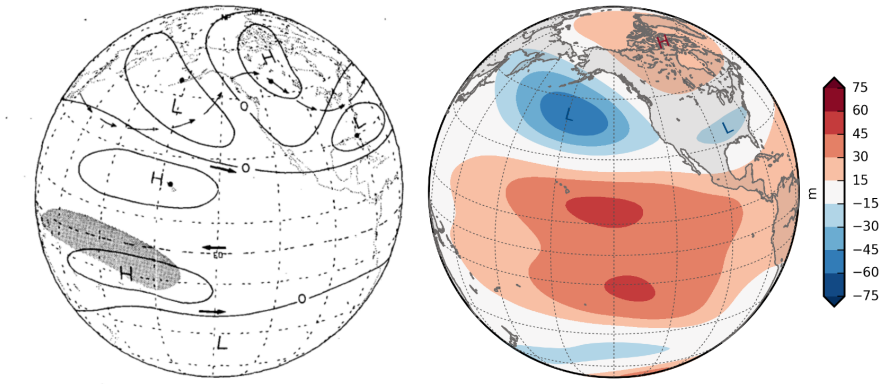

Figure 1.3: Left: Schematic of the winter upper-tropospheric geopotential height anomalies associated with El Niño, from Horel and Wallace (1981). Right: linear regression of observed 200-hPa geopotential height anomalies onto the Niño3.4 index. ERA-20CR (Poli et al. 2016), 1901-2010, January–March.

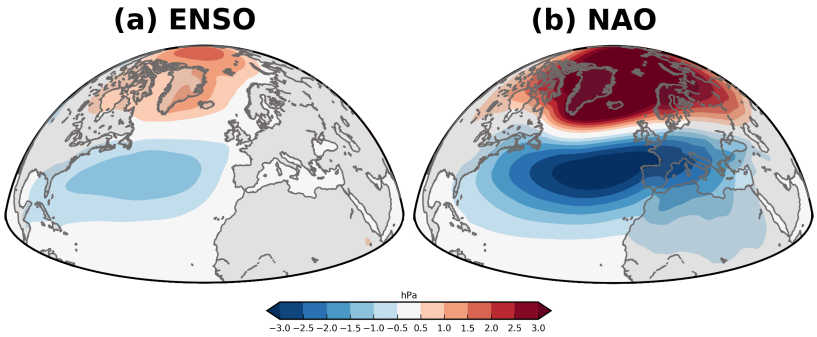

Figure 1.4: Linear regression of observed SLP anomalies onto (a) the Niño3.4 index and (b) the NAO index. ERA-20CR (Poli et al. 2016), 1901-2010, January–March.

1.1.3 The ENSO-NAE teleconnection

In the NAE region, the impacts and dynamics of the ENSO teleconnection are still partly unsettled, but a robust and significant signal in surface temperature, SLP and precipitation has been reported at least in late winter (January–March, JFM; see Brönnimann 2007 for a review). For SLP, and in the case of El Niño, the response consists of a negative anomaly in the mid-latitude North Atlantic and a positive anomaly at high latitudes (Fig. 1.4a), which together form the "canonical" dipole representing the late-winter ENSO signature.

The canonical dipole is often described as resembling or projecting onto the negative phase of the North Atlantic Oscillation (NAO), whose characteristic SLP pattern is also a dipole over the NAE region (Fig. 1.4b; see Hurrell and Deser 2009 for a review). The NAO is the dominant mode of variability in the North Atlantic and is considered to be largely internally-generated, but a possible forced component linked to ENSO would be valuable for increasing regional predictability. Whether a dynamical relationship between these two modes of variability exists, beyond the apparent surface similarity, will be discussed in Chapters 2 and 3.

The mechanisms leading to the canonical dipole are subject to debate, in particular whether tropospheric dynamics are dominating, as opposed to stratospheric processes. Concerning the so-called tropospheric pathway, while it is clear that the tail of the main wave train reaches the western North Atlantic

(Fig. 1.3), there is no agreement on its relationship with the mid-latitude surface anomaly of the same sign. This topic will be explored in Chapters 2 and 3.

On the other hand, the hypothesis of a stratospheric pathway relies on the fact that ENSO has been reported to impact the Northern Hemisphere polar stratosphere by warming and decelerating – in the case of El Niño – the climatological stratospheric polar vortex (see Domeisen et al. 2019 for a review). The stratospheric anomalies may then propagate downwards and affect the NAE surface climate, contributing to the establishment and/or persistence of the canonical dipole. The impact of ENSO on the stratosphere itself, however, still has many unclear aspects, such as the (a)symmetry of the response to El Niño and La Niña and the underlying dynamics. This topic will be examined in Chapter 4.

Finally, the canonical dipole mostly covers the central-western North Atlantic, while the ENSO signal over the eastern part of the basin and the European continent is not fully established, an issue made difficult by the fact that the ENSO response in this sector varies depending on the data, period and methods used. Chapter 5 is dedicated to investigating this issue and to examining potential tropospheric pathways of the ENSO teleconnection to Europe with a theoretical approach.

1.2 Thesis structure

The core of this thesis embodies four research articles, presented as self-contained chapters. Their titles, which give a hint of the main topic at hand, are indicated in Table 1.1, as well as the corresponding chapter number.

Ch.	Article	Title
2	Mezzina et al. 2020	Dynamics of the ENSO teleconnection and NAO variability in the North Atlantic–European late winter
3	Mezzina et al. 2021a	Multi-model assessment of the late-winter extratropical response to El Niño and La Niña
4	Mezzina et al. 2021b	Multi-model assessment of the late-winter stratospheric response to El Niño and La Niña
5	Mezzina et al. 2022	Tropospheric pathways of the late-winter ENSO teleconnection to Europe

Table 1.1: Correspondence between chapters and research articles.

To understand the conceptual and methodological framework of these studies, designed to complement each other, it is useful to first break down the main dynamical aspects that they address.

1.2.1 Troposphere versus stratosphere

The vertical axis in Fig. 1.5 depicts schematically whether the troposphere, the stratosphere or both are considered in each chapter.

The tropospheric main wave train described in Sect. 1.1.2 is, as a matter of fact, mentioned in all the chapters, since it is the dominant extra-tropical response to ENSO, and the first feature to examine before any further step. A diagnostic that is common to all chapters, although in varying form, is the map of 200-hPa anomalous geopotential height (Fig. 1.3b is an example), which is a convenient way to detect the main wave train and is expected to resemble the well-known figure of Horel and Wallace (1981) (Fig. 1.3a), whether in model or reanalysis data.

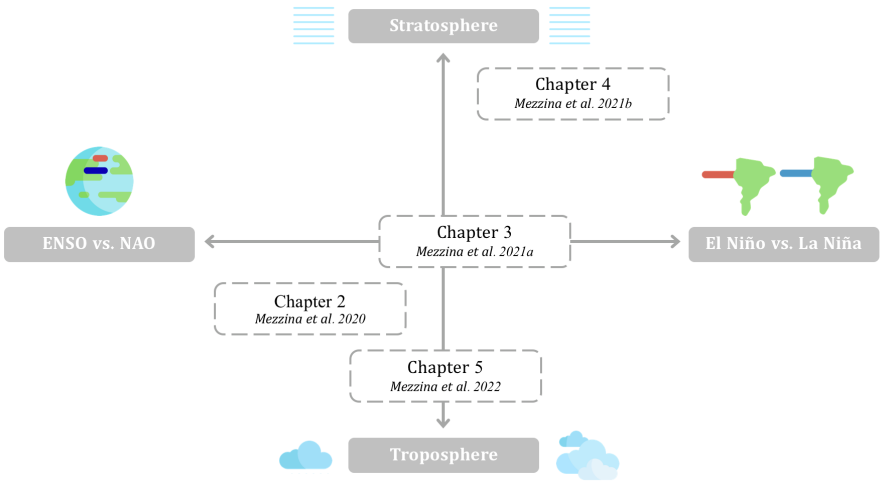

Figure 1.5: Schematic representation of the thesis structure in terms of the topics addressed in the different chapters.

In Chapter 2, the structure of the main wave train is examined and compared to the upper-level signature of the NAO, via longitude-latitude maps and vertical cross-sections. The main wave train is also central in Chapter 3, where its generation is thoroughly analyzed starting from the SST anomalies in the tropical Pacific, with focus on the differences between El Niño and La Niña. A specific form of the source term in Equation 1.1, the Tropical Rossby Wave Source, is examined, to take into account the interaction between the anomalous upper-level divergent flow and the climatological rotational flow. In these two chapters, placed in the central-bottom part of Fig. 1.5, the ENSO stratospheric response is shown at some lower-stratospheric levels (30 and 50 hPa), but not discussed in detail.

In Chapter 5, the target is again the troposphere, but a broader perspective is adopted and other pathways are investigated in addition to the main wave train, in order to explain different signals over Europe. The stratosphere is not examined in this study, which hence appears at the very bottom of Fig. 1.5.

In contrast, Chapter 4 is found at the top of Fig. 1.5, since it is fully focused on the impacts of ENSO on the polar stratosphere, distinguishing between lower (up to 50 hPa) and upper stratosphere (up to 1 hPa). Similarly to Chapter 3, a systematic comparison between the responses to El Niño and La Niña is carried out, and maps of geopotential height and temperature at several stratospheric levels are examined after looking at zonal-mean vertical cross sections. The usual 200-hPa maps serve as well, since at high latitudes the tropopause is located below this level, and the tropospheric main wave train is again invoked to explain the origin of the stratospheric response, further linking this chapter to the other ones.

1.2.2 El Niño, La Niña and the NAO

The horizontal axis of Fig. 1.5 shows a schematic distribution of the chapters in terms of two key themes: the relationship between ENSO and the NAO, and the (a)symmetry of the atmospheric response to El Niño and La Niña (see Sects. 1.1.2 and 1.1.3).

Chapter 2 is located at the extreme left, since the linear component of the ENSO teleconnection and the NAO are systematically compared in observations. Later, their signatures are further separated in atmosphere-only simulations with prescribed observed SSTs by considering the ensemble means, which maximize the forced component, versus residuals, which emphasize the internal component.

Chapter 3 is placed in the middle, since both the El Niño/La Niña asymmetry and the relationship with the NAO are discussed, this time in the framework of

Figure 1.6: Schematic representation of the thesis structure in terms of the models and experiments analyzed in the different chapters.

a set of atmosphere-only sensitivity experiments (see Sect. 1.2.3).

Chapter 5 is also located halfway, but for the opposite reason: only the linear ENSO teleconecction is examined, so the El Niño/La Niña asymmetry is not considered, but no comparison with the NAO is carried out either.

Finally, an assessment of the (a)symmetry of the response to El Niño and La Niña is carried out in the polar stratosphere in Chapter 4, which is then placed at the extreme right of Fig. 1.5.

1.2.3 Models and experiments

Another aspect that is relevant for the thesis' framework is the increasing complexity of the models and experiments analyzed (Fig. 1.6).

In Chapter 2, the analysis is based on two ensembles of AMIP[1]-like experiments, i.e. atmosphere-only simulations forced with time-varying observed SSTs. In particular, two models are considered: one of intermediate-complexity and another which is state-of-the-art. This kind of simulations is relatively straightforward – with some caution – to compare with reanalysis spanning the same period of the forcing SSTs, which are also examined in the chapter. The ENSO contribution to the models' predictive skill is also assessed.

[1]Atmospheric Model Intercomparison Project, a standard experimental protocol for global atmospheric general circulation models

In Chapters 3 and 4, three atmosphere-only, state-of-the-art models are used, but, in this case, a set of sensitivity experiments with idealized forcing is analyzed: the anomalous SSTs used as boundary conditions, in fact, only cover the tropical Pacific, and are designed to mimic a canonical, strong ENSO event, with El Niño and La Niña considered separately. A multi-model assessment of the tropospheric and stratospheric signals is performed by analyzing the ensemble-mean (forced) response in each model.

Finally, historical runs of ocean-atmosphere coupled models are examined in Chapter 5, where two versions of the same state-of-the-art model, with different vertical resolution in the atmosphere, are used.

1.3 Objectives

The overall objective of this thesis is to provide a comprehensive analysis of the ENSO–NAE teleconnection in late winter (JFM), and more specifically:

1. To establish the main dynamical mechanisms underlying the canonical ENSO-NAE dipole (Chapters 2, 3, 4)

2. To understand whether the ENSO response in the NAE region is associated with NAO variability, and if other common aspects are present apart from the similarity in their dipolar SLP patterns (Chapters 2, 3)

3. To diagnose asymmetries in the tropospheric response related to El Niño and La Niña, and to elucidate their cause (Chapter 3)

4. To assess the robustness and asymmetry of the signal linked to El Niño and La Niña in the lower and middle-upper polar stratosphere, and to provide a dynamical interpretation for the response (Chapter 4)

5. To explore potential paths of the tropospheric ENSO teleconnection to Europe and their role in favouring different observed responses, and to reconcile them with the theoretical basis of linear Rossby wave propagation (Chapter 5)

Chapter 2

Dynamics of the ENSO teleconnection and NAO variability in the North Atlantic–European late winter

This chapter contains the research article Mezzina et al. 2020 and addresses objectives 1 and 2 from Sect. 1.3.

Mezzina, B., García-Serrano, J., Bladé, I., & Kucharski, F. (2020). Dynamics of the ENSO Teleconnection and NAO Variability in the North Atlantic–European Late Winter. *J. Clim.*, *33*(3), 907–923. https://doi.org/10.1175/JCLI-D-19-0192.1

Dynamics of the ENSO Teleconnection and NAO Variability in the North Atlantic–European Late Winter

BIANCA MEZZINA

Barcelona Supercomputing Center, Barcelona, Spain

JAVIER GARCÍA-SERRANO

Barcelona Supercomputing Center, and Group of Meteorology, Universitat de Barcelona, Barcelona, Spain

ILEANA BLADÉ

Group of Meteorology, Universitat de Barcelona, Barcelona, Spain

FRED KUCHARSKI

Abdus Salam International Centre for Theoretical Physics, Trieste, Italy

(Manuscript received 8 March 2019, in final form 30 September 2019)

ABSTRACT

The winter extratropical teleconnection of El Niño–Southern Oscillation (ENSO) in the North Atlantic–European (NAE) sector remains controversial, concerning both the amplitude of its impacts and the underlying dynamics. However, a well-established response is a late-winter (January–March) signal in sea level pressure (SLP) consisting of a dipolar pattern that resembles the North Atlantic Oscillation (NAO). Clarifying the relationship between this "NAO-like" ENSO signal and the actual NAO is the focus of this study. The ENSO–NAE teleconnection and NAO signature are diagnosed by means of linear regression onto the sea surface temperature (SST) Niño-3.4 index and an EOF-based NAO index, respectively, using long-term reanalysis data (NOAA-20CR, ERA-20CR). While the similarity in SLP is evident, the analysis of anomalous upper-tropospheric geopotential height, zonal wind, and transient-eddy momentum flux, as well as precipitation and meridional eddy heat flux, suggests that there is no dynamical link between the phenomena. The observational results are further confirmed by analyzing two 10-member ensembles of atmosphere-only simulations (using an intermediate-complexity and a state-of-the-art model) with prescribed SSTs over the twentieth century. The SST-forced variability in the Northern Hemisphere is dominated by the extratropical ENSO teleconnection, which provides modest but significant SLP skill in the NAE midlatitudes. The regional internally generated variability, estimated from residuals around the ensemble mean, corresponds to the NAO pattern. It is concluded that distinct dynamics are at play in the ENSO–NAE teleconnection and NAO variability, and caution is advised when interpreting the former in terms of the latter.

1. Introduction

While it is no news that El Niño–Southern Oscillation (ENSO) is a primary source of global predictability, improving seasonal forecasts in the extratropics is constrained by the large internal variability and challenged by the limited understanding of the ENSO teleconnections. In this work, we clarify some aspects of the late-winter ENSO teleconnection to the North Atlantic–European (NAE) region by investigating its relationship with the North Atlantic Oscillation (NAO).

In the North Pacific–American (NPA) sector, the wintertime ENSO teleconnection shows a well-known surface response: a reinforcement of the climatological Aleutian low is observed for positive ENSO events (El Niño, i.e., warm SST anomalies in the central-eastern tropical Pacific), while a signal of opposite sign is expected for negative ones [see Trenberth et al. (1998) and Alexander et al. (2002) for reviews]. This feature is part of the surface signature of a tropospheric large-scale Rossby wave train that propagates from the tropical Pacific toward high latitudes with a distinctive eastward-arching shape (Hoskins and Karoly 1981; Horel and Wallace 1981). This wave train is not fully established in

Corresponding author: Bianca Mezzina, bianca.mezzina@bsc.es

DOI: 10.1175/JCLI-D-19-0192.1

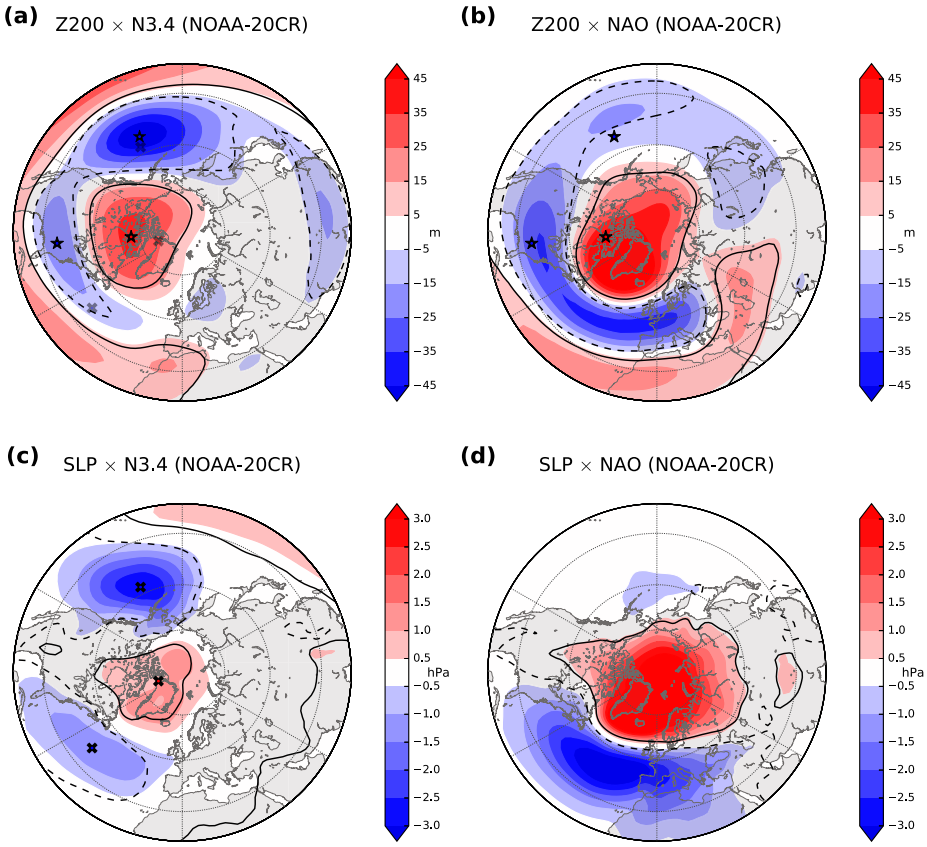

FIG. 1. Regression maps of circulation anomalies in JFM using NOAA-20CR (1901–2014). (top) Z200 regressed onto the (a) N3.4 and (b) NAO index. (bottom) SLP regressed onto the (c) N3.4 and (d) NAO index. Contours indicate statistically significant areas at 95% confidence level. The symbol × indicates the approximate center of action in the regression of SLP onto N3.4; the symbol ★ is the same, but for Z200.

observations until January (e.g., Wang and Fu 2000; Bladé et al. 2008), although the standard winter season used to analyze ENSO teleconnections is December–February (DJF). Furthermore, this ENSO-forced pattern over the NPA region is different from the internal Pacific–North America (PNA) mode: the two patterns are in fact almost in spatial quadrature (Nigam 2003) and have distinct time scales [see Nigam and Baxter (2014) for a review]. In the NPA sector, the description in terms of tropospheric Rossby wave propagation accounts for most of the observed ENSO impacts in several fields, such as precipitation and temperature [see Trenberth et al. (1998) for a review].

In the NAE sector the situation is more intricate, as the amplitude of the impacts is weaker and less statistically significant, due to the dominant internal variability, and the underlying dynamics driving the ENSO teleconnection are still unsettled. However, a modest but systematic ENSO signal, robust and stationary over the last 300 years, has been identified in late winter [January–March (JFM)] for surface temperature, precipitation, and sea level pressure [see Brönnimann (2007) for a review]. A simple approach to reveal this "canonical" ENSO signal in sea level pressure (SLP) is by linear regression onto the Niño-3.4 index, as in Fig. 1c (details in section 2). The strongest extratropical signal is in the North Pacific sector, the deepened Aleutian low mentioned above, but a significant response is also present in the North Atlantic, with one positive center located at high latitudes, covering Greenland and part of Canada, and one negative center at about 40°N, extending from the eastern coast of the United States to almost the eastern boundary of the basin. This ENSO-related dipole is often termed "NAO-like," alluding to the North Atlantic Oscillation, the dominant mode of variability in the NAE region. Indeed, the NAO spatial

signature also exhibits a dipole in sea level pressure, as shown in Fig. 1d, where an NAO index was defined and used for the linear regression. The depicted pattern, well established in the literature [see Hurrell et al. (2003) and Hurrell and Deser (2009) for reviews], corresponds to the negative NAO phase and, despite the overall larger amplitude and spatial extent, a similarity to the pattern associated with ENSO is evident. This visual resemblance is confirmed by the spatial correlation between the two patterns in Figs. 1c and 1d, which is 0.87 over the NAE sector (20°–90°N, 90°W–40°E).

The main aim of this work is to understand whether the response to ENSO in the NAE sector should be interpreted as associated with NAO variability, beyond the similarity in their surface signatures. While doing so, we will also examine some features of the tropospheric pathway of the ENSO–NAE teleconnection; the more recent, widely discussed stratospheric pathway hypothesis (e.g., Cagnazzo and Manzini 2009; Polvani et al. 2017) will not be addressed in this manuscript. Additionally, we discuss the contribution of ENSO to the predictive skill of two atmospheric models.

ENSO events involve a variety of spatiotemporal patterns (Timmermann et al. 2018); along with the "conventional" eastern Pacific (EP) ENSO, several studies identified a second mode, the central Pacific (CP) ENSO, with SST anomalies peaking around the date line [see Capotondi et al. (2015) for a review]. Although not all events fit exclusively in one category, recent works pointed at different, possibly nonlinear extratropical impacts related to the two types of ENSO (e.g., Graf and Zanchettin 2012; Zhang et al. 2015, 2019). In this study, we focus on the so-called conventional ENSO, for which robust atmospheric teleconnections to the Northern Hemisphere have been established (e.g., DeWeaver and Nigam 2002; Hoerling and Kumar 2002; Kumar et al. 2005); these teleconnections are linearly related to Niño-3.4 SST variability (Zhang et al. 2016).

An added value of this work is to provide an analysis of the ENSO–NAE teleconnection from a JFM perspective: although DJF- and JFM-based analyses lead to comparable SLP patterns (not shown; cf. Deser et al. 2017), as they are both dominated by the JF response, several studies have reported intraseasonal (month to month) differences in the ENSO–NAE teleconnection, such as a shift in the SLP response in the Atlantic basin from a monopole in November–December to a dipole in January–February (see King et al. 2018; Ayarzagüena et al. 2018, and references therein). More generally, the entire ENSO-forced wave train in the Northern Hemisphere shows marked differences between December and January (when the classical wave-like response really emerges; e.g., Livezey and Mo 1987; Alexander et al. 2002) that are not well captured by models, which tend to simulate January-like patterns in both months (Bladé et al. 2008). For these reasons, many authors suggest avoiding December when studying the winter ENSO–NAE teleconnection and indicate JFM as a more suitable choice than DJF [e.g., Bladé et al. 2008; Fereday et al. 2008; see Brönnimann (2007) for a review]. With this fully JFM-based study, we follow their recommendation and hope that it will encourage other authors to adopt the same practice.

We begin by examining the ENSO and NAO signals in several atmospheric fields in observations and continue by considering model outputs from an intermediate-complexity AGCM (atmospheric general circulation model) and a state-of-the-art one. Finally, the skill of the two models is evaluated with and without the effects of ENSO.

2. Data and methods

a. *Observational data*

The primary dataset is the NOAA Twentieth-Century Reanalysis v2c (NOAA-20CR), a long record (1851–2014) of global atmospheric fields reconstructed by assimilating surface pressure and using observed sea surface temperature (SST) and sea ice distribution as boundary conditions. The atmospheric model has T62 horizontal spectral resolution and 28 levels in the vertical (L28), up to ~2.5 hPa (Compo et al. 2011). We repeated our analyses using the ECMWF twentieth-century reanalysis (ERA-20CR) dataset, which is another long-term reanalysis (1900–2010) with similar boundary conditions and assimilation system, but higher resolution: T159L91, with the top at 0.01 hPa (Poli et al. 2016). We found no appreciable differences in most cases (see Fig. A1 in the appendix) as the troposphere behaves similarly in the two products, but dissimilarities do emerge in the stratosphere (see Fig. A2). Other datasets used are the GPCC Full Data Reanalysis (v7) at 0.5° × 0.5° resolution for precipitation (Schneider et al. 2011) and the Met Office HadISST1.1 for SST (Rayner et al. 2003).

b. *Models*

We analyze integrations of the International Center for Theoretical Physics (ICTP) AGCM (v. 41), nicknamed SPEEDY (Simplified Parameterizations, Primitive-Equation Dynamics), forced with observed SST anomalies (HadISST1.1). The simulations consist of a 10-member ensemble over the period 1901–2014. SPEEDY is an intermediate-complexity AGCM with a coarse horizontal resolution (T30 in the standard configuration used here) and eight vertical levels, with a crude lower stratosphere (the top two layers are at 100 and 30 hPa). These features and the simplified parameterizations allow a low computational cost, but still the model compares reasonably well with

observations in relevant climate aspects and atmospheric teleconnections (Kucharski et al. 2013, and references therein).

The ECMWF ERA-20CM dataset is a 10-member ensemble of atmosphere-only integrations forced with SST and sea ice cover from HadISST2, for the period 1899 to 2010 (Hersbach et al. 2015). The AGCM is an adaptation of the Integrated Forecasting System (IFS) version cy38r1, with the same resolution as ERA-20CR (T159L91).

c. Methods

We focus on the period from 1901 to 2014 (1901–2010 for ERA-20CM, 1901–2013 for GPCC); choosing long-term records responds to the need of working with a large set of ENSO events to avoid sampling issues (Deser et al. 2017), but our results fully agree with previous findings obtained using shorter periods [e.g., NCEP–NCAR in Brönnimann (2007); ERA-40 in García-Serrano et al. (2011); ERA-Interim in Zhang et al. (2016)]. All fields are linearly detrended after computing JFM averages.

In the reanalysis, we obtain the spatial signatures of ENSO and the NAO with linear regressions. For ENSO, we use the Niño-3.4 index (N3.4), defined as the area-averaged SST anomalies over 5°S–5°N, 170°–120°W. This index is commonly used to describe the conventional ENSO (e.g., Deser et al. 2010) and its teleconnections (e.g., Sterl et al. 2007; Yang and DelSole 2012); using the Niño-3 index (SST anomalies averaged over 5°S–5°N, 150°–90°W) provides identical patterns (not shown). We use EOF analysis to compute the NAO index as the first principal component (PC) of SLP over the NAE domain (20°–90°N, 90°W–40°E). For the sake of comparison with the ENSO regressions, we choose the NAO index associated with a negative NAO phase.

In the models, the experimental setup enables us to ideally separate the forced and internal variability, which are intrinsically mixed in the observations. The ensemble mean mostly contains the response to the prescribed forcing, while the deviations from the ensemble mean, emerging from having perturbed the initial conditions in the different members, represent the atmospheric internal variability unrelated to the boundary forcing. In section 3b, we separately study the patterns arising from the forced and internal variability using EOF analysis. An index describing the leading boundary-forced component is defined as the first PC of the ensemble-mean SLP in the Northern Hemisphere (20°–90°N); the regression maps of ensemble-mean variables onto this index represent the "forced" response. To estimate the internally generated variability in the NAE sector, we first compute the residuals around the ensemble mean for all 10 members; then, we use the concatenated residual time series as input for another EOF analysis and for linear regressions onto the corresponding leading PC of the SLP.

In the second part of section 3a, we diagnose the dynamics involved in the teleconnection patterns using transient-eddy momentum flux ($u'v'$) to examine synoptic-scale waves, and meridional eddy heat flux (v^*T^*) for planetary-scale waves. To obtain $u'v'$, we apply a 24-h filter (e.g., Wallace et al. 1988; Chang and Fu 2002) to daily data of zonal and meridional wind from NOAA-20CR to retain high-frequency variability, and compute monthly means of their daily covariance. The term v^*T^* is computed from the same daily data but with no time filtering; instead, we consider the daily deviations from the zonal mean for each variable and again produce monthly-mean covariances (e.g., Newman and Nash 2000; Hinssen and Ambaum 2010).

Finally, in section 3b(2) we evaluate the skill of the models in ensemble-mean fields by computing the anomaly correlation coefficient (ACC) with NOAA-20CR. As this is a point-by-point evaluation, the data are previously regridded by interpolating from higher to lower resolutions. To assess statistical significance, we use a two-tailed t test for correlation in the regressions and a one-tailed t test in the case of ACC, both at a 95% confidence level. To avoid too liberal statistical thresholds, we use an effective sample size that takes into account the autocorrelation of the time series (Bretherton et al. 1999).

3. Results

a. Observational teleconnections

1) Regression maps

Despite sharing some common features at the surface, the ENSO and NAO teleconnections show little similarity when considering their upper-level signatures. In the regression map of 200-hPa geopotential height (Z200) onto the N3.4 index, the familiar ENSO-forced Rossby wave train is evident (Fig. 1a). The upper-tropospheric counterpart of the deepened Aleutian low is prominent among the series of centers arching eastward across the Pacific and North America, with maximum amplitude exceeding 50 m; a weaker negative anomaly (maximum ~ 25 m) is centered over the eastern United States, well to the west of the corresponding feature at the surface (its approximate center is marked with a faded black cross), as further discussed in section 3a(2). There is no significant response over the eastern North Atlantic or Europe. In contrast, the negative lobe of the upper-level signature of the NAO (Fig. 1b) covers the entire NAE sector, spreading far into continental Europe. The zonally elongated, almost annular-shaped anomalies, which project on the circumglobal waveguide pattern (Branstator 2002; García-Serrano and Haarsma 2017), are weak over the

North Pacific (up to −20 m, about half the values in the North Atlantic). The closest feature in the two patterns is the positive anomaly north of 60°N, but a closer inspection reveals marked differences, as the NAO-related anomalies are again more zonally symmetric and stronger, with a broader extent and centered in a different location (cf. the anomaly in Fig. 1b with the star marking the approximate location of the ENSO-related center in Fig. 1a). Note also that the temporal correlation between the N3.4 and NAO indices is only 0.24, indicating a shared variance of less than 6%.

The anomalies in the upper-level zonal circulation also differ between the two modes, as can be seen in the top panels of Fig. 2, which show the regression maps of 200-hPa zonal wind (U200) onto the N3.4 and NAO indices and the corresponding climatology (thick contours). Not surprisingly, the strongest response to ENSO occurs again in the North Pacific (Fig. 2a), where a reinforced zonal flow south of 40°N (maximum values above 5 m s^{-1}) is found; a band of negative, weaker anomalies (−1 to −2 m s^{-1}) is present around 50°N. The overall result is a lengthening and equatorward displacement of the North Pacific jet. A similar dipolar anomaly along latitude bands is present in the North Atlantic: however, the amplitudes are slightly weaker (the positive anomalies are now less than 4 m s^{-1}) and the anomalies are mainly confined to the western part of the basin. In contrast, the anomalous pattern associated with the NAO (Fig. 2b) exhibits strong anomalies throughout the entire NAE sector (amplitudes above 5 m s^{-1} in both signs) that influence the exit of the North Atlantic jet.

The middle panels of Fig. 2 show the regression maps of transient-eddy momentum flux at 200 hPa ($u'v'200$), a diagnostic for eddy–mean flow interaction. Concerning the NAO (Fig. 2d), the anomalous momentum carried by synoptic-scale eddies appears key in shaping the associated circulation and precipitation patterns (Fig. 2f): the equatorward flux of westerly momentum (blue shading) in the exit region of the North Atlantic eddy-driven jet, with convergence of eddy momentum flux around 35°N, is consistent with the meridional displacement of the jet exit. The storm tracks are also shifted equatorward so that the synoptic disturbances tend to be diverted toward southern Europe, leading to the wet–dry dipole in precipitation typical of the NAO (Fig. 2f). In the case of ENSO, anomalous transient-eddy activity accompanies the large-scale impact on the North Pacific atmospheric circulation linked to the Rossby wave train [Fig. 2c; see Trenberth et al. (1998) for review]. In contrast to the NAO, the exit of the North Atlantic jet is not affected (Figs. 2a,c), leading to nonsignificant impacts on European precipitation (Fig. 2e; e.g., Mariotti et al. 2002).

2) VERTICAL CROSS SECTIONS

As noticed earlier, the ENSO-related negative anomaly in Z200 in the NAE is centered over the eastern United States (around 80°W; Fig. 1a). To explore the relationship between this center of action and the anomaly of the same sign at surface, centered eastward at roughly 50°W, we first examine the vertical structure of the anomalous geopotential height field (Z). A height–longitude cross section averaged over 30°–40°N is examined, consistent with the approximate location of the two centers of action; the linear regression onto the N3.4 index (Fig. 3a) shows that the surface and upper-level negative anomalies are part of the same vertical structure, with three main features: a limited longitudinal extent, as opposed to the NAO, which shows a broader structure (Fig. 3b); a well-defined maximum around 200 hPa, as expected for a forced Rossby wave train (e.g., Ambrizzi and Hoskins 1997); and a westward tilt with height. This tilt is a well-known aspect of vertically propagating large-scale Rossby wave trains (e.g., Lau 1979; Hsu and Wallace 1985), but in the context of the ENSO–NAE teleconnection it has barely been addressed (García-Serrano et al. 2011), despite being an important dynamical feature of this teleconnection. Figure 3c shows the regression of v^*T^* (where the asterisks denote deviations from the zonal mean; see section 2) in the same cross section: an anomalous positive heat flux collocated with the tilted geopotential height anomaly dominates the signal in the ENSO case, consistent with the westward tilt with height (e.g., Vallis 2006). Unlike for ENSO, the NAO v^*T^* anomalies are stronger close to the surface rather than at upper levels (Fig. 3d), which is consistent with an NAO-related change in the baroclinic region of eddy genesis (e.g., Vallis and Gerber 2008; Gerber and Vallis 2009). Additionally, as expected from the horizontal maps of Fig. 1, the NAO geopotential height anomalies (Fig. 3b) show a wider structure and less westward tilt with height than their ENSO counterpart (Fig. 3c). Note that the well-known equivalent barotropic structure of the NAO is not readily apparent in this cross section due to the southwest–northeast orientation of the anomalies in the North Atlantic (cf. the negative center in Fig. 1b with the parallels at 30° and 50°N), but is revealed by recomputing the cross section along the latitude of maximum Z200 anomalies (as shown in Fig. A3).

b. *Simulated teleconnections*

1) FORCED AND INTERNAL VARIABILITY IN THE MODELS

The SST-forced variability in the two models is examined by considering the ensemble mean of the AMIP-like

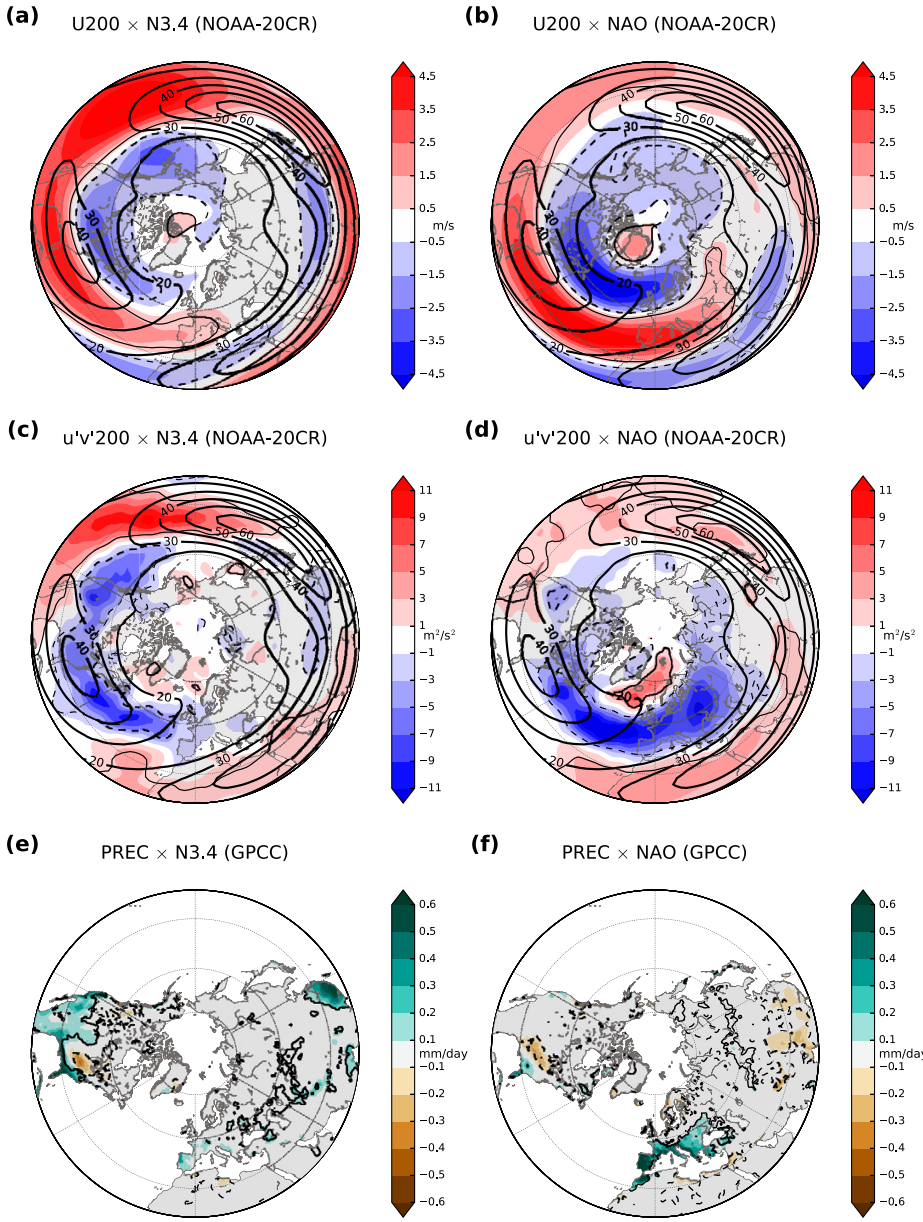

FIG. 2. As in Fig. 1, but for (top) U200, (middle) $u'v'200$, and (bottom) precipitation from GPCC (1901–2013). Thick contours in (a)–(d) indicate the JFM climatology of U200.

10-member simulations. Figures 4c and 5c show the leading EOFs of the ensemble-mean SLP in SPEEDY and ERA-20CM, respectively, north of 20°N; that is, the patterns maximizing the SST-forced variance of SLP in the Northern Hemisphere. The associated fraction of explained variance is 44.9% for SPEEDY, and 47.7% for ERA-20CM. The spatial patterns are, for both models, reminiscent of the canonical ENSO teleconnection in the extratropics: the black marks help the eye spot the similarity, as they indicate the approximate location of the main centers of action in the observational teleconnection (Fig. 1c). Both models show a

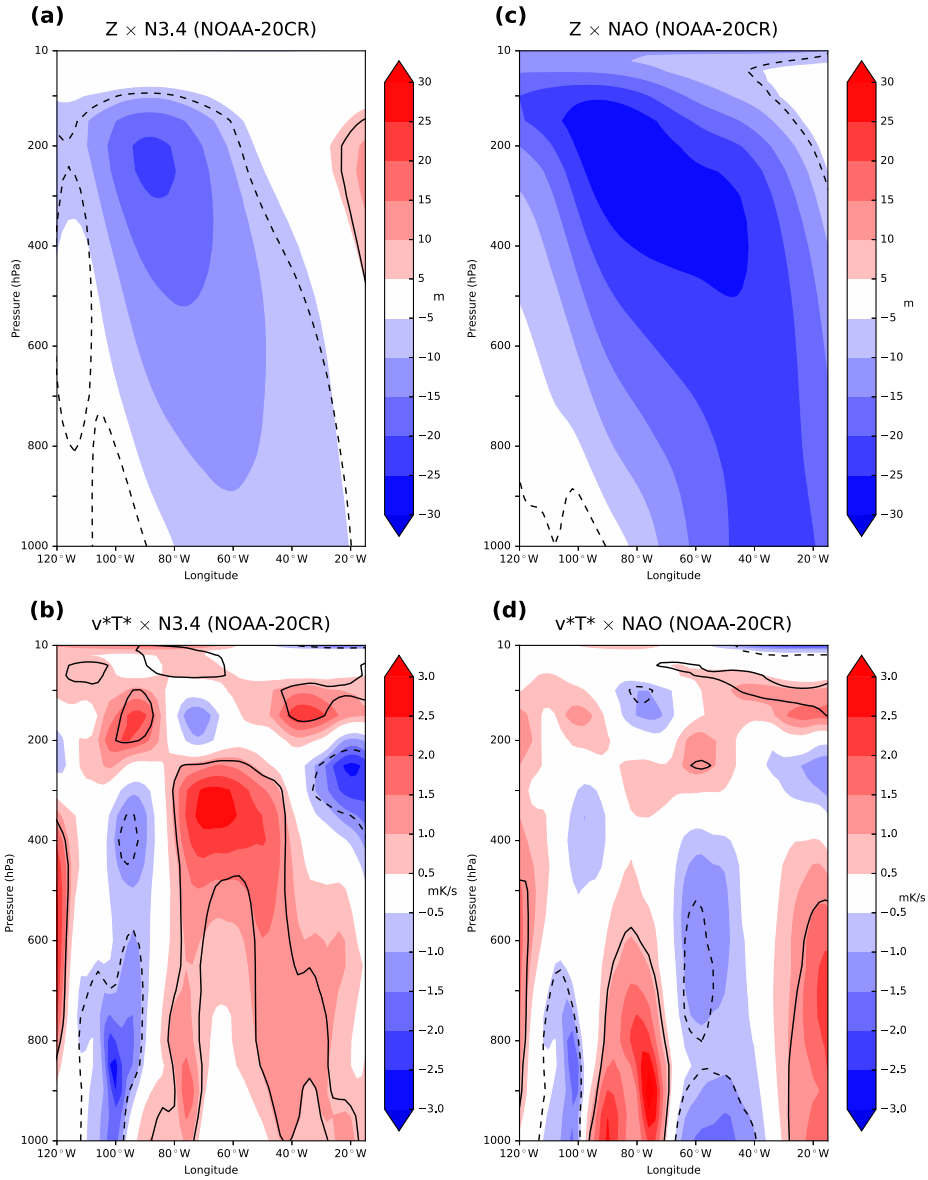

FIG. 3. As in Fig. 1, but for height–longitude profiles of (top) geopotential height and (bottom) v^*T^* averaged over 30°–40°N.

signal in the North Pacific indicative of a strengthening of the Aleutian low, and negative anomalies in the North Atlantic approximately at the location of the mid-latitude center of action that is part of the observed ENSO–NAE dipole, with amplitudes that are also comparable. There are, however, some differences in shape and extent. In particular, the negative SLP signal in SPEEDY is at a maximum farther into the eastern North Atlantic, whereas the positive anomalies at high latitudes are weaker and more confined with respect to observations; the opposite happens in the polar region in ERA-20CM (cf. Fig. 1c with Figs. 5c and 6c). These differences between models and observations are likely due to imperfect formulations and biases in the models,

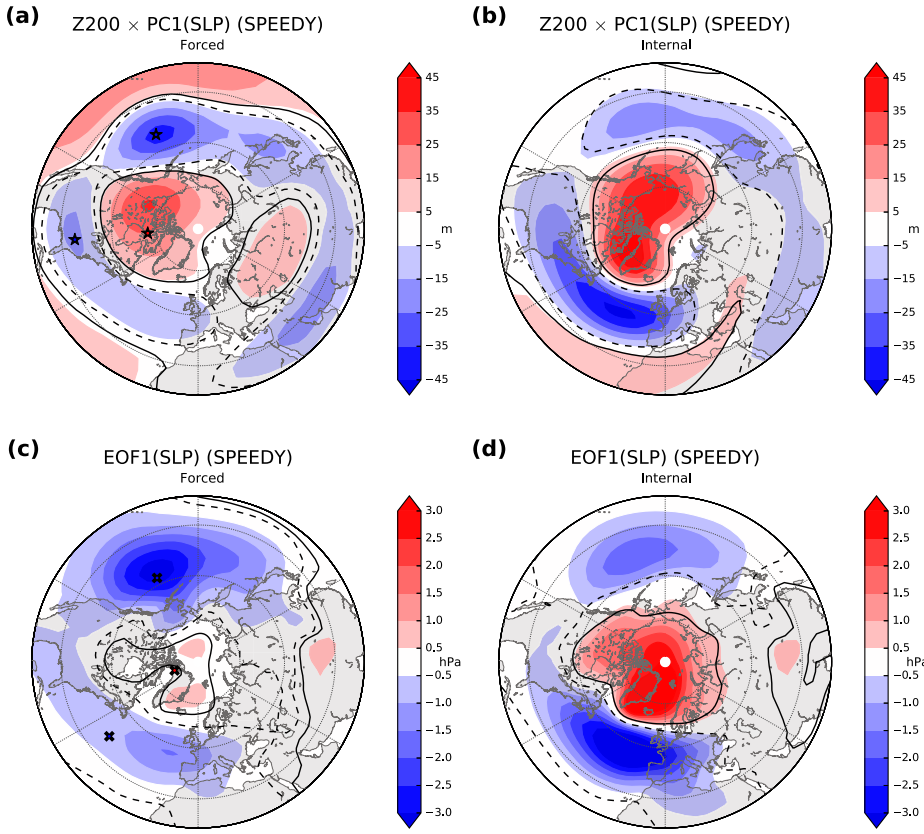

FIG. 4. Forced and internal variability in SPEEDY (JFM; 1901–2014). (a) Linear regression of ensemble-mean Z200 anomalies onto the first PC of ensemble-mean SLP north of 20°N. (b) Linear regression of residual Z200 anomalies onto the first PC of residual SLP in the NAE domain. (c) EOF1 of ensemble-mean SLP north of 20°N. (d) EOF1 of residual SLP in the NAE domain. Contours indicate statistically significant areas at 95% confidence level. The × and ★ symbols show the locations of the ENSO teleconnection in NOAA-20CR (see Fig. 1).

although it has to be acknowledged that substantial uncertainty resides in both in situ and reanalysis data. However, internal atmospheric variability may dominate any discrepancy.

The fact that ENSO dominates the SST-forced variability in the Northern Hemisphere is confirmed by examining the corresponding anomalies in the upper troposphere, here illustrated by regressing the ensemble-mean Z200 onto the leading principal component of ensemble-mean SLP (Figs. 4a and 5a). The resulting maps strongly resemble the ENSO response (Fig. 1a) with the highs and lows closely reproducing the location of the observed ENSO-induced wave train (cf. black marks). In in the NAE region, the negative center over the western North Atlantic is accompanied by a second one farther east, toward Europe (more evident in ERA20-CM, present but not significant in Fig. 1a); this secondary center of action has been suggested to be the result of a wave train split (García-Serrano et al. 2011) or the signature of a pathway involving the stratosphere (Cagnazzo and Manzini 2009). We can verify that ENSO is indeed responsible for this boundary-forced variability by examining the SST patterns associated with the SLP principal components. The distinctive signature of ENSO in the tropical Pacific is evident in the regression maps of Fig. 6, together with well-known ENSO signals in other basins, such as the warming of the Indian Ocean and parts of the subtropical Atlantic [e.g., see Alexander et al. (2002) for a review]. Finally, the connection between these SST-forced EOFs and ENSO is confirmed by the correlation of the SLP principal components with the N3.4 index: 0.87 for SPEEDY and 0.82 for ERA-20CM.

We now focus on the internally generated variability, as described in section 2c. The first EOF of the residual

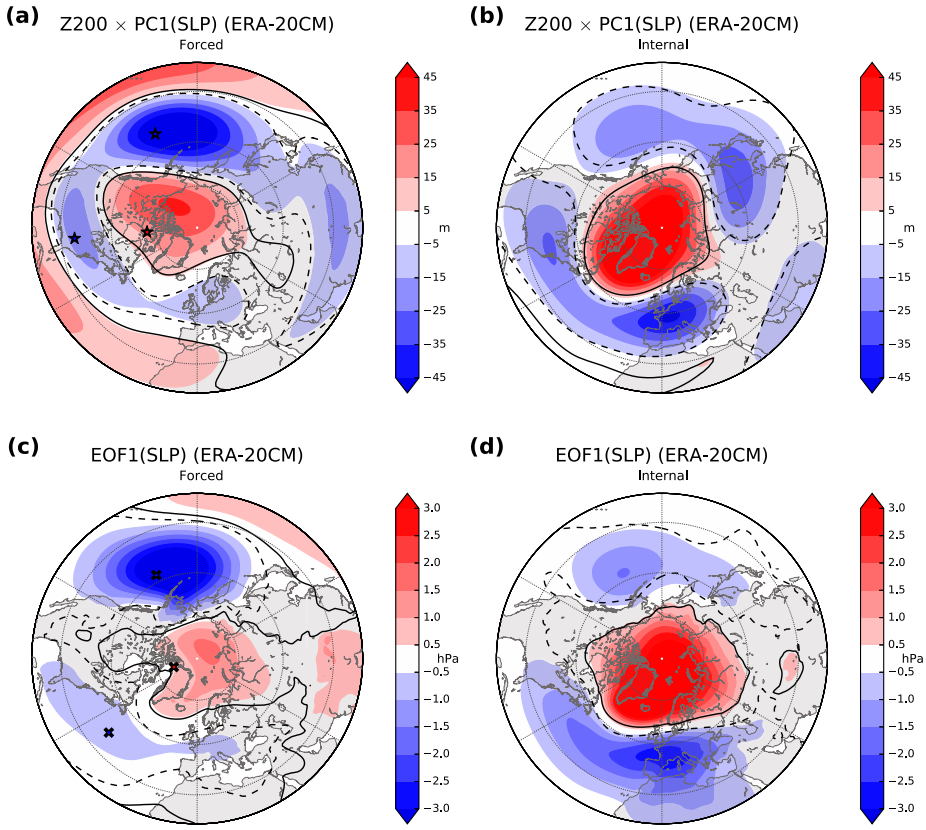

FIG. 5. As in Fig. 4, but in ERA-20CM (JFM; 1901–2010).

SLP over the NAE is the regional mode explaining the largest fraction of internal variance (47.8% for SPEEDY and 43.7% for ERA-20CM), and the associated patterns are shown in Figs. 4d and 5d. In the North Atlantic, the similarity with the dipolar signature of the observed NAO is clear (cf. Fig. 1d), with minor differences in location. In both models, anomalies of smaller amplitude in phase with those in the Atlantic basin, absent in the observational NAO (Fig. 1d; see also Fig. A1d), are present in the North Pacific, possibly related to model biases in the local atmospheric circulation (at least in SPEEDY, which overestimates the eddy activity there; see García-Serrano and Haarsma 2017). Similar remarks apply to Z200 (Figs. 4b and 5b), as in both cases the patterns strongly resemble the upper-level, circumglobal signature of the observed NAO (cf. Fig. 1b).

2) SKILL

We complement the analysis by evaluating the predictive skill of the ensemble means in capturing observed variability, using NOAA-20CR as reference. In both models, the ACC (i.e., correlation between reanalysis and ensemble-mean anomalies; see section 2) maps of Z200 show areas of moderate to high skill (0.4–0.7) in the North Pacific and North Atlantic (Fig. 7, top panels) that can be attributed to the Rossby wave train associated with ENSO: the regions with higher values approximately correspond to the centers of action in the SST-forced patterns (Figs. 4a and 5a). The skill is more modest at the surface (bottom panels in Fig. 7); still, both models show significant SLP skill in the eastern North Pacific and western North Atlantic at midlatitudes. The SST-forced variability that is present at high latitudes is masked by the large total variability, leading to poor, not significant skill: indeed, the standard deviation of SLP has well-known maxima at high latitudes over the North Pacific, the North Atlantic, and the Siberian coast, a feature that is reproduced by the models (Figs. 8c,d). In other words, the signal-to-noise ratio is low at high latitudes, while it is high enough in midlatitudes to allow for some predictability and significant skill. To estimate how much of this midlatitude skill is ENSO-related, we

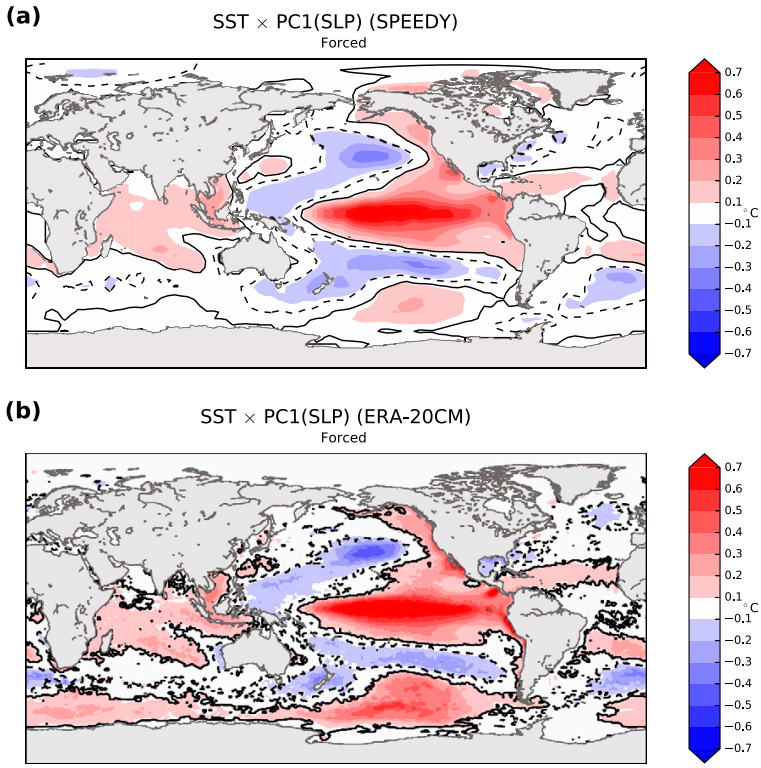

FIG. 6. Linear regression of JFM ensemble-mean SST anomalies onto the first PC of ensemble-mean SLP north of 20°N in (a) SPEEDY (1901–2014; Fig. 4c) and (b) ERA-20CM (1901–2010; Fig. 5c). Contours indicate statistically significant areas at 95% confidence level.

remove the linear contribution of ENSO by using the residuals of the linear regression onto the N3.4 index to recompute the ACC of SLP. Without ENSO, the skill drops in most regions (Figs. 8a,b). The North Atlantic is left with no significant values, except for a small region around Newfoundland (slightly more extended in SPEEDY), approximately corresponding to the node of the ENSO-related and NAO dipolar patterns (Figs. 4c,d and 5c) and to a relative minimum in total variability (Figs. 8c,d). Some ENSO-unrelated skill is also found in the subtropical North Atlantic, which may indicate predictability originating from the tropical Atlantic. The SLP skill that is present at midlatitudes in the North Atlantic, at least in the western and central parts of the basin (Figs. 7c,d), is therefore likely related to the tail of the ENSO-forced wave train and its westward tilt with height discussed in section 3a.

It has to be acknowledged that some skill discussed here may arise from SST anomalies that are in part driven by atmospheric processes and would not necessarily be predictable in a coupled framework; hence, it may not translate into actual predictability.

4. Summary and discussion

In the first part, we compared the three-dimensional structure of the observed late-winter (JFM) ENSO and NAO atmospheric anomalies in the Northern Hemisphere, the starting point of the study being the similarity between the surface signature of ENSO and the NAO over the NAE sector (Figs. 1c,d). A linear approach with reanalysis data spanning the twentieth century reveals that this similarity is limited to the surface and does not extend to the upper troposphere: not only are the regression maps of Z200 onto the N3.4 and NAO indices distinct in their spatial structure (Figs. 1a,b), but more importantly the patterns suggest different mechanisms involved. The anomalous centers in SLP associated with ENSO are linked to the well-known Rossby wave train crossing the NPA sector. A nonlinear approach, such as the use of separate

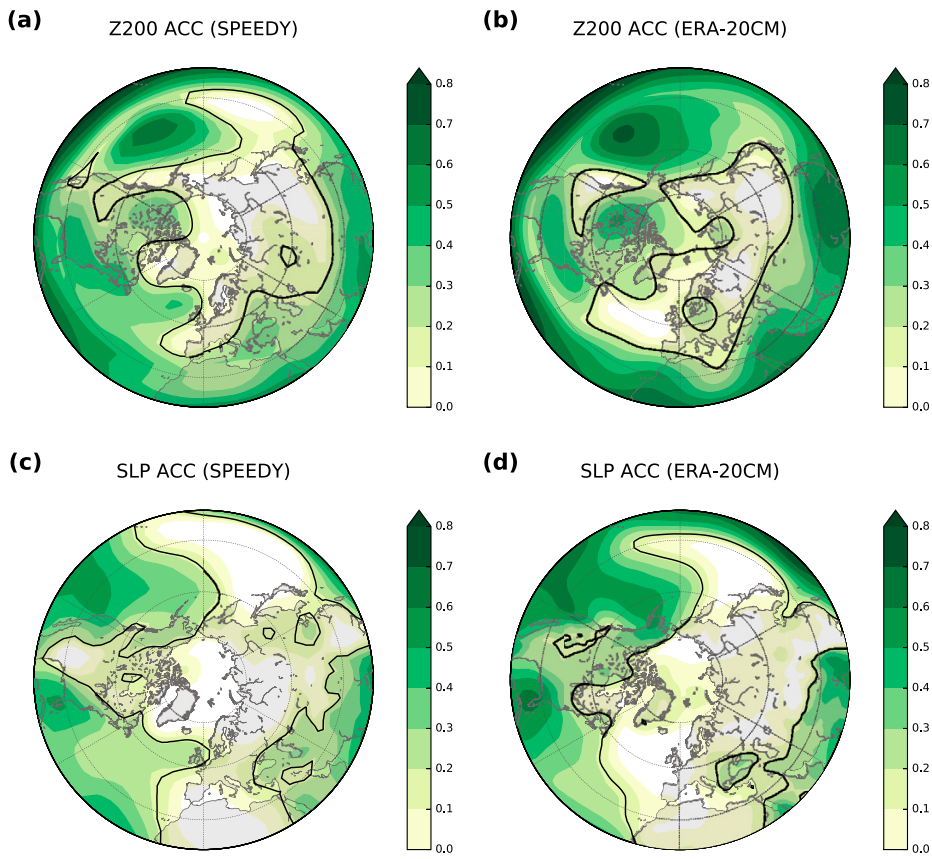

FIG. 7. Anomaly correlation coefficient (ACC) maps of (a) Z200 and (c) SLP ensemble-mean detrended anomalies in SPEEDY with respect to NOAA-20CR (JFM; 1901–2014). (b),(d) As in (a),(c), but in ERA-20CM (1901–2010). Contours indicate statistically significant areas at 95% confidence level.

composites for El Niño and La Niña, provides similar results concerning the ENSO–NAE teleconnection (not shown), in agreement with Deser et al. (2017) and Garfinkel et al. (2019), who found no significant nonlinearities in SLP for DJF, and Ayarzagüena et al. (2018), who assessed linearity in JF. In contrast, the upper-level circulation anomalies associated with the NAO display a more zonally symmetric pattern reminiscent of the circumglobal waveguide pattern, which is linked to the zonal propagation of disturbances trapped in the westerly jet (Branstator 2002; García-Serrano and Haarsma 2017). These patterns related to ENSO and the NAO are not new, but in this context they provide clear evidence that the two teleconnections are widely different.

The use of transient-eddy momentum fluxes highlights further differences. The anomalous $u'v'200$ associated with the NAO (Fig. 2d) strongly affects the circulation over the North Atlantic and Europe, influencing the exit of the eddy-driven jet and displacing the preferred meridional location of the storm tracks, in line with the notion that the NAO is tightly related to the variability of the North Atlantic jet (e.g., Vallis and Gerber 2008; Gerber and Vallis 2009). The comparison with the corresponding ENSO pattern reveals weaker transient-eddy convergence acting closer to the core of the eddy-driven jet, rather than affecting the storm tracks (Fig. 2c). Thus, synoptic-scale systems and their two-way interaction with the climatological flow appear to be a fundamental aspect of the NAO, but are relatively minor actors in the ENSO–NAE teleconnection. This essential difference is also reflected in the precipitation patterns associated with the two modes (Figs. 2e,f): the shift in the North Atlantic storm track due to anomalous eddy activity accounts for the wet–dry dipole over Europe typical of the NAO

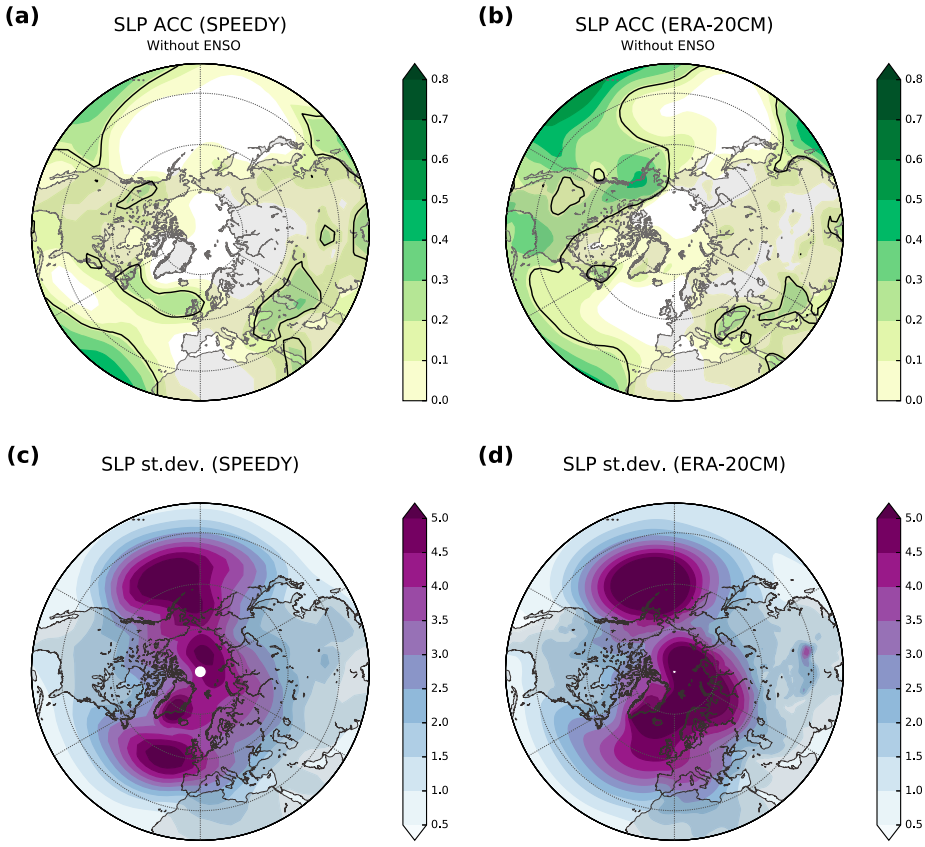

FIG. 8. (a),(b) As in Figs. 7c and 7d, respectively, but using the residual anomalies of the linear regression onto N3.4. (c),(d) Interannual standard deviation of SLP across all 10 members in SPEEDY and ERA-20CM, respectively.

[see Hurrell et al. (2003) and Hurrell and Deser (2009) for reviews]. In contrast, the lack of significant ENSO-related precipitation anomalies over Europe is consistent with the minor impact ENSO has on the regional storm track.

The notion that ENSO and the NAO are independent, with the latter largely encompassing internal variability, is supported by the results obtained with two ensembles of AGCM simulations used to separate SST-forced and internally generated variability. The main assumption is that the ensemble mean retains the forced atmospheric component arising from the imposed, interannually varying SSTs. In practice, some internal variability is probably still present, given the relatively small ensemble size (10 members) and the high level of stochastic noise in the NAE region (e.g., Deser et al. 2017). For clarity, we stress that in ERA-20CM the prescribed forcing also features sea ice concentration (unlike in SPEEDY) and that the prescribed SST field is itself an ensemble, accounting for observational uncertainty. There are no other assumptions concerning the forced component or the source of the signals: ENSO is not a priori singled out. However, the leading SST-forced component in the Northern Hemisphere circulation appears to be strongly related to ENSO: first, it shows similarities with the observed ENSO teleconnection, at the surface and particularly in the upper troposphere (cf. the left panels of Figs. 4 and 5 with Figs. 1a,c); second, its signature in the SST field projects on that of ENSO; finally, there is a strong temporal correlation with the N3.4 index. Our results are consistent with the recent work by Zhang et al. (2016), who used a similar approach to revisit and study the forced atmospheric teleconnections in an AGCM with 50 members; from their analysis, based on the 500-hPa geopotential height (DJF) for the period 1979–2014, the first boundary-forced EOF mode in the

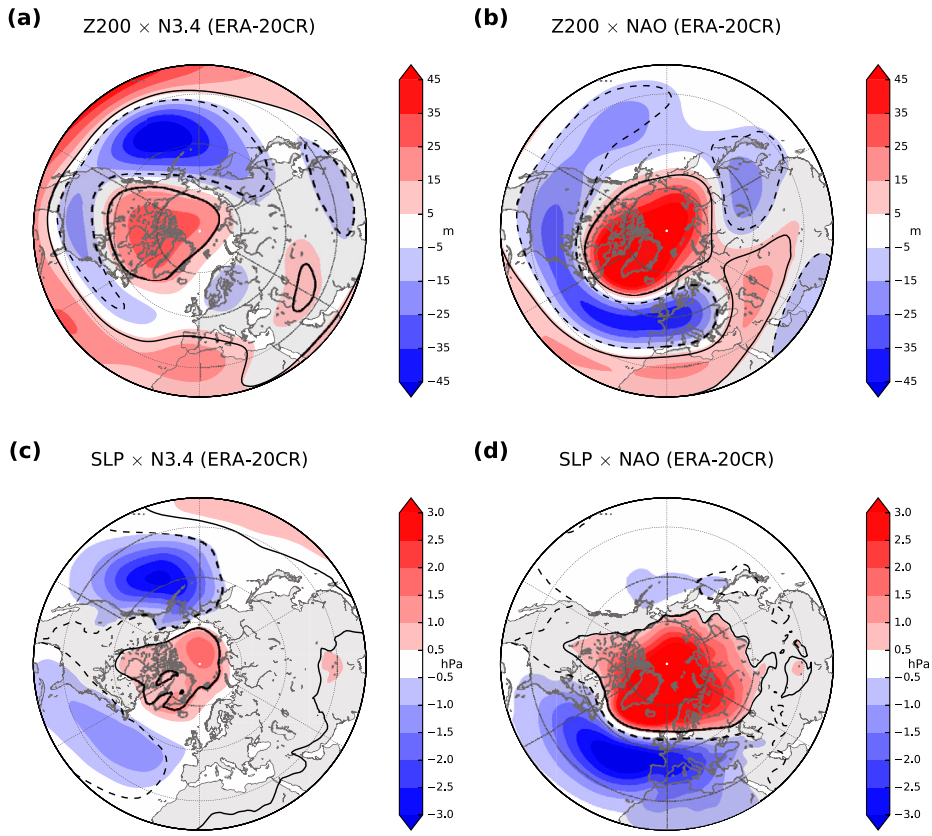

FIG. A1. As in Fig. 1, but using ERA-20CR (1901–2010).

Northern Hemisphere corresponds to the linear, symmetric response to ENSO and its PC is highly correlated with the Niño-3.4 index (0.9), thus describing the same canonical teleconnection of ENSO addressed here.

On the other hand, the analysis carried out using the residuals (right panels of Figs. 4 and 5) shows that the NAO arises from internal atmospheric processes and that boundary forcing does not play a key role in driving the NAO at interannual time scales. The comparison between the SST-forced and internally generated patterns in two very different models supports the hypothesis that the atmospheric responses to ENSO and the NAO emerge from separate dynamics and are not physically linked. This idea was already suggested by several previous works: van Oldenborgh et al. (2000), Giannini et al. (2001), Czaja et al. (2002), Handoh et al. (2006), and Hu et al. (2013), among others.

Examining the forced variability in the two models allows for some interesting considerations on the canonical ENSO–NAE teleconnection. The two AGCMs are widely different in spatial resolution, parameterizations, and overall complexity, and most importantly in how they treat the stratosphere: ERA-20CM features a fully resolved stratosphere with 91 model levels, while in SPEEDY only two levels crudely represent the lower stratosphere. Despite that, they both capture the surface signature of ENSO in the Euro-Atlantic sector reasonably well (Figs. 4c and 5c). This result shows that the tropospheric pathway for the teleconnection is properly reproduced in both models (Figs. 4a and 5a) and suggests that the stratosphere may not play a major role in forcing the canonical signal, although further investigation is needed.

Finally, an assessment of the models' skill in capturing observed variability shows results in agreement with estimates of potential predictability by Kumar et al. (2005). In addition, it emerges that the large-scale wave train associated with ENSO, and in particular its tail and vertically tilted structure, may account for the modest

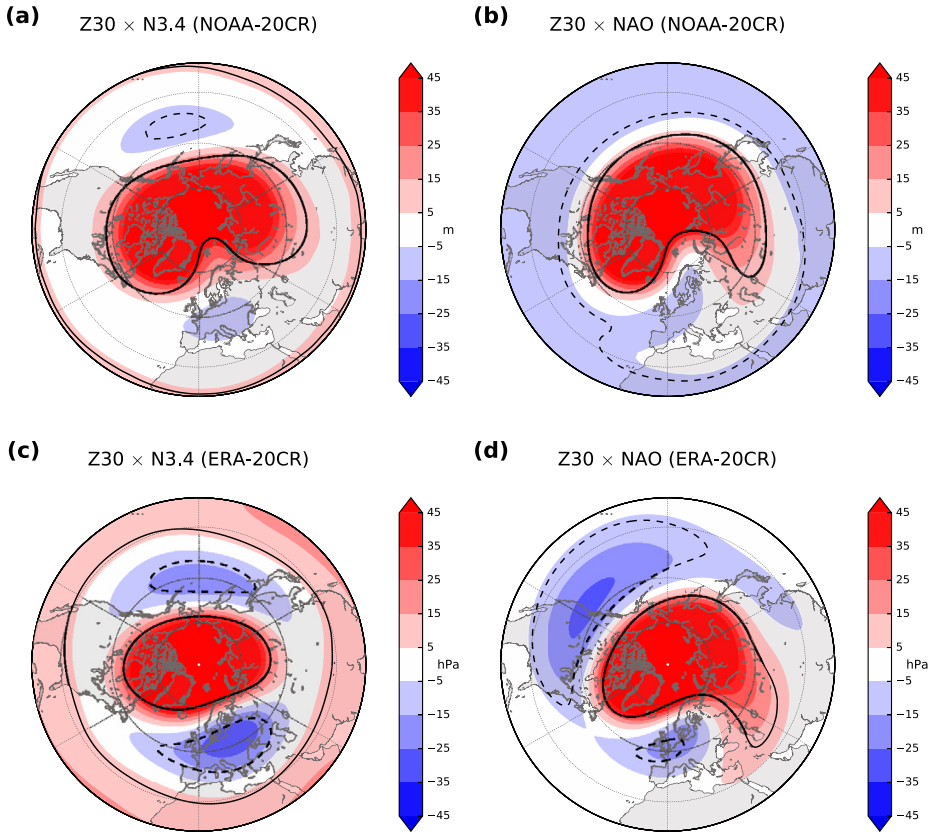

FIG. A2. (a),(b) Regression map of Z30 anomalies in JFM using NOAA-20CR (1901–2014) onto the N3.4 and NAO index, respectively. (c),(d) As in (a),(b), but using ERA-20CR (1901–2010). Contours indicate statistically significant areas at 95% confidence level.

but significant skill in the western-central North Atlantic at midlatitudes.

5. Conclusions

The main objective of this work was to understand if the similarity between the dipolar pattern of SLP anomalies in the NAE associated with ENSO in late winter (JFM) and the surface NAO signature is indicative of other common aspects and possibly of a relationship between these two phenomena.

Our conclusion is that the late-winter ENSO–NAE teleconnection is dynamically distinct from the NAO, with differences in terms of both signatures and involved mechanisms. Considering the upper-level dynamics is crucial, since the contrast already emerges between the ENSO-induced arching wave train propagating northeastward, with no dipole over the Atlantic basin, and the circumglobal, more zonally symmetric perturbations related to the NAO. The differences are evident in other fields and diagnostics, such as transient-eddy momentum flux, meridional eddy heat flux, and precipitation, indicating the need to go beyond the SLP anomalies when characterizing the ENSO response in the NAE sector.

Thus, a more general term such as ''dipole-like'' or simply ''dipole over the Atlantic'' should be preferred to the widely used ''NAO-like'' when discussing the ''canonical'' winter surface signature of the ENSO–NAE teleconnection. We also suggest that the relative amplitudes of Aleutian low anomalies and dipolar anomalies in the North Atlantic may be used as a simple metric to interpret whether anomalous dipolar structures in the NAE region are related to the ENSO teleconnection or, instead, to the hemispheric signature of the NAO.

Finally, we highlight that ENSO, which is shown to dominate the forced variability in the Northern Hemisphere, contributes to the North Atlantic midlatitude predictability at the surface.

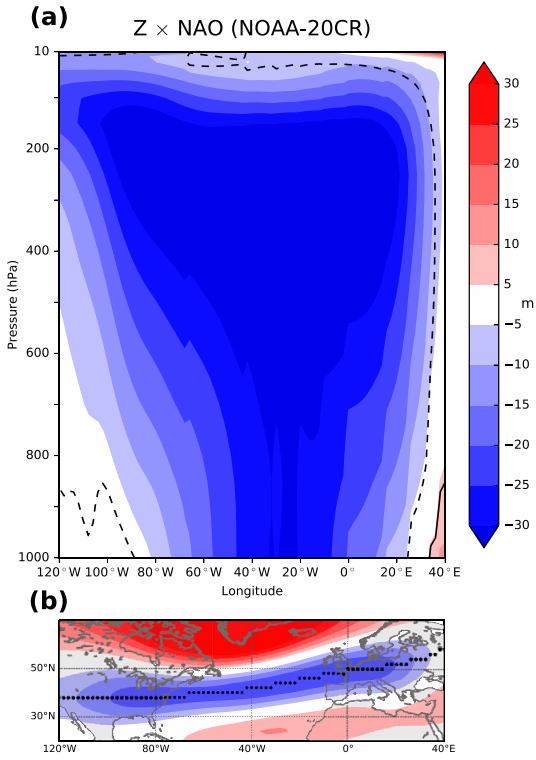

FIG. A3. (a) As in Fig. 3b, but instead of averaging over 30°–40°N we consider cross sections at varying latitudes along (b) the path that marks the maximum (negative) values in the regression of Z200 onto the NAO index.

Acknowledgments. This work received funding from the Spanish MINECO-funded DANAE project (CGL2015-68342-R). B.M. and J.G.-S. were supported by the ''Contratos Predoctorales para la Formación de Doctores'' (BES-2016-076431) and ''Ramón y Cajal'' (RYC-2016-21181) programmes, respectively. Technical support at BSC (Computational Earth Sciences group) is sincerely acknowledged. The authors are thankful to the two anonymous reviewers for their comments, which helped to improve the clarity of the manuscript.

APPENDIX

Additional Results

As mentioned in the main text (section 2a), the analysis carried out with NOAA-20CR was repeated using ERA-20CR. Figure A1 shows the regression maps onto the N3.4 and NAO index of SLP and Z200, to be compared with Fig. 1. In Fig. A2, the corresponding patterns in the lower stratosphere (30 hPa) from the two datasets are compared. As both reanalyses only assimilate surface data, they should be used with caution above the tropopause (Fujiwara et al. 2017). NOAA-20CR, in particular, has coarser vertical resolution with respect to ERA-20CM (L28 vs L91) and is known to be affected by strong biases in the stratosphere (Compo et al. 2011).

Figure A3a shows the NAO vertical structure of geopotential height anomalies along the path of latitudes corresponding to the maximum values in the regressions of Z200 (shown in Fig. A3b), as discussed in section 3a(2).

REFERENCES

Alexander, M. A., I. Bladé, M. Newman, J. R. Lanzante, N.-C. Lau, and J. D. Scott, 2002: The atmospheric bridge: The influence of ENSO teleconnections on air–sea interaction over the global oceans. *J. Climate*, **15**, 2205–2231, https://doi.org/10.1175/1520-0442(2002)015<2205:TABTIO>2.0.CO;2.

Ambrizzi, T., and B. J. Hoskins, 1997: Stationary Rossby-wave propagation in a baroclinic atmosphere. *Quart. J. Roy. Meteor. Soc.*, **123**, 919–928, https://doi.org/10.1002/qj.49712354007.

Ayarzagüena, B., S. Ineson, N. J. Dunstone, M. P. Baldwin, and A. A. Scaife, 2018: Intraseasonal effects of El Niño–Southern Oscillation on North Atlantic climate. *J. Climate*, **31**, 8861–8873, https://doi.org/10.1175/JCLI-D-18-0097.1.

Bladé, I., M. Newman, M. A. Alexander, and J. D. Scott, 2008: The late fall extratropical response to ENSO: Sensitivity to coupling and convection in the tropical west Pacific. *J. Climate*, **21**, 6101–6118, https://doi.org/10.1175/2008JCLI1612.1.

Branstator, G., 2002: Circumglobal teleconnections, the jet stream waveguide, and the North Atlantic Oscillation. *J. Climate*, **15**, 1893–1910, https://doi.org/10.1175/1520-0442(2002)015<1893:CTTJSW>2.0.CO;2.

Bretherton, C. S., M. Widmann, V. P. Dymnikov, J. M. Wallace, and I. Bladé, 1999: The effective number of spatial degrees of freedom of a time-varying field. *J. Climate*, **12**, 1990–2009, https://doi.org/10.1175/1520-0442(1999)012<1990:TENOSD>2.0.CO;2.

Brönnimann, S., 2007: Impact of El Niño–Southern Oscillation on European climate. *Rev. Geophys.*, **45**, RG3003, https://doi.org/10.1029/2006RG000199.

Cagnazzo, C., and E. Manzini, 2009: Impact of the stratosphere on the winter tropospheric teleconnections between ENSO and the North Atlantic and European region. *J. Climate*, **22**, 1223–1238, https://doi.org/10.1175/2008JCLI2549.1.

Capotondi, A., and Coauthors, 2015: Understanding ENSO diversity. *Bull. Amer. Meteor. Soc.*, **96**, 921–938, https://doi.org/10.1175/BAMS-D-13-00117.1.

Chang, E. K., and Y. Fu, 2002: Interdecadal variations in Northern Hemisphere winter storm track intensity. *J. Climate*, **15**, 642–658, https://doi.org/10.1175/1520-0442(2002)015<0642:IVINHW>2.0.CO;2.

Compo, G. P., and Coauthors, 2011: The Twentieth Century Reanalysis Project. *Quart. J. Roy. Meteor. Soc.*, **137**, 1–28, https://doi.org/10.1002/qj.776.

Czaja, A., P. van der Vaart, and J. Marshall, 2002: A diagnostic study of the role of remote forcing in tropical Atlantic variability. *J. Climate*, **15**, 3280–3290, https://doi.org/10.1175/1520-0442(2002)015<3280:ADSOTR>2.0.CO;2.

Deser, C., M. A. Alexander, S.-P. Xie, and A. S. Phillips, 2010: Sea surface temperature variability: Patterns and mechanisms. *Annu. Rev. Mar. Sci.*, **2**, 115–143, https://doi.org/10.1146/annurev-marine-120408-151453.

——, I. R. Simpson, K. A. McKinnon, and A. S. Phillips, 2017: The Northern Hemisphere extratropical atmospheric circulation response to ENSO: How well do we know it and how do we evaluate models accordingly? *J. Climate*, **30**, 5059–5082, https://doi.org/10.1175/JCLI-D-16-0844.1.

DeWeaver, E., and S. Nigam, 2002: Linearity in ENSO's atmospheric response. *J. Climate*, **15**, 2446–2461, https://doi.org/10.1175/1520-0442(2002)015<2446:LIESAR>2.0.CO;2.

Fereday, D. R., J. R. Knight, A. A. Scaife, C. K. Folland, and A. Philipp, 2008: Cluster analysis of North Atlantic–European circulation types and links with tropical Pacific sea surface temperatures. *J. Climate*, **21**, 3687–3703, https://doi.org/10.1175/2007JCLI1875.1.

Fujiwara, M., and Coauthors, 2017: Introduction to the SPARC Reanalysis Intercomparison Project (S-RIP) and overview of the reanalysis systems. *Atmos. Chem. Phys.*, **17**, 1417–1452, https://doi.org/10.5194/acp-17-1417-2017.

García-Serrano, J., and R. J. Haarsma, 2017: Non-annular, hemispheric signature of the winter North Atlantic Oscillation. *Climate Dyn.*, **48**, 3659–3670, https://doi.org/10.1007/s00382-016-3292-3.

——, B. Rodríguez-Fonseca, I. Bladé, P. Zurita-Gotor, and A. de la Cámara, 2011: Rotational atmospheric circulation during North Atlantic-European winter: The influence of ENSO. *Climate Dyn.*, **37**, 1727–1743, https://doi.org/10.1007/s00382-010-0968-y.

Garfinkel, C. I., I. Weinberger, I. P. White, L. D. Oman, V. Aquila, and Y.-K. Lim, 2019: The salience of nonlinearities in the boreal winter response to ENSO: North Pacific and North America. *Climate Dyn.*, **52**, 4429–4446, https://doi.org/10.1007/s00382-018-4386-x.

Gerber, E. P., and G. K. Vallis, 2009: On the zonal structure of the North Atlantic Oscillation and annular modes. *J. Atmos. Sci.*, **66**, 332–352, https://doi.org/10.1175/2008JAS2682.1.

Giannini, A., M. A. Cane, and Y. Kushnir, 2001: Interdecadal changes in the ENSO teleconnection to the Caribbean region and the North Atlantic Oscillation. *J. Climate*, **14**, 2867–2879, https://doi.org/10.1175/1520-0442(2001)014<2867:ICITET>2.0.CO;2.

Graf, H.-F., and D. Zanchettin, 2012: Central Pacific El Niño, the "subtropical bridge," and Eurasian climate. *J. Geophys. Res.*, **117**, D01102, https://doi.org/10.1029/2011JD016493.

Handoh, I. C., A. J. Matthews, G. R. Bigg, and D. P. Stevens, 2006: Interannual variability of the tropical Atlantic independent of and associated with ENSO: Part I. The north tropical Atlantic. *Int. J. Climatol.*, **26**, 1937–1956, https://doi.org/10.1002/joc.1343.

Hersbach, H., C. Peubey, A. Simmons, P. Berrisford, P. Poli, and D. Dee, 2015: ERA-20CM: A twentieth-century atmospheric model ensemble. *Quart. J. Roy. Meteor. Soc.*, **141**, 2350–2375, https://doi.org/10.1002/qj.2528.

Hinssen, Y. B., and M. H. Ambaum, 2010: Relation between the 100-hPa heat flux and stratospheric potential vorticity. *J. Atmos. Sci.*, **67**, 4017–4027, https://doi.org/10.1175/2010JAS3569.1.

Hoerling, M. P., and A. Kumar, 2002: Atmospheric response patterns associated with tropical forcing. *J. Climate*, **15**, 2184–2203, https://doi.org/10.1175/1520-0442(2002)015<2184:ARPAWT>2.0.CO;2.

Horel, J. D., and J. M. Wallace, 1981: Planetary-scale atmospheric phenomena associated with the Southern Oscillation. *Mon. Wea. Rev.*, **109**, 813–829, https://doi.org/10.1175/1520-0493(1981)109<0813:PSAPAW>2.0.CO;2.

Hoskins, B. J., and D. J. Karoly, 1981: The steady linear response of a spherical atmosphere to thermal and orographic forcing. *J. Atmos. Sci.*, **38**, 1179–1196, https://doi.org/10.1175/1520-0469(1981)038<1179:TSLROA>2.0.CO;2.

Hsu, H., and J. M. Wallace, 1985: Vertical structure of wintertime teleconnection patterns. *J. Atmos. Sci.*, **42**, 1693–1710, https://doi.org/10.1175/1520-0469(1985)042<1693:VSOWTP>2.0.CO;2.

Hu, Z.-Z., A. Kumar, B. Huang, W. Wang, J. Zhu, and C. Wen, 2013: Prediction skill of monthly SST in the North Atlantic Ocean in NCEP Climate Forecast System version 2. *Climate Dyn.*, **40**, 2745–2759, https://doi.org/10.1007/s00382-012-1431-z.

Hurrell, J. W., and C. Deser, 2009: North Atlantic climate variability: The role of the North Atlantic Oscillation. *J. Mar. Syst.*, **78**, 28–41, https://doi.org/10.1016/j.jmarsys.2008.11.026.

——, Y. Kushnir, G. Ottersen, and M. Visbeck, 2003: An overview of the North Atlantic Oscillation. *The North Atlantic Oscillation: Climatic Significance and Environmental Impact*, *Geophys. Monogr.*, Vol. 134, Amer. Geophys. Union, 1–35.

King, M. P., I. Herceg-Bulić, I. Bladé, J. García-Serrano, N. Keenlyside, F. Kucharski, C. Li, and S. Sobolowski, 2018: Importance of late fall ENSO teleconnection in the Euro-Atlantic sector. *Bull. Amer. Meteor. Soc.*, **99**, 1337–1343, https://doi.org/10.1175/BAMS-D-17-0020.1.

Kucharski, F., F. Molteni, M. P. King, R. Farneti, I. Kang, and L. Feudale, 2013: On the need of intermediate complexity general circulation models: A "SPEEDY" example. *Bull. Amer. Meteor. Soc.*, **94**, 25–30, https://doi.org/10.1175/BAMS-D-11-00238.1.

Kumar, A., Q. Zhang, P. Peng, and B. Jha, 2005: SST-forced atmospheric variability in an atmospheric general circulation model. *J. Climate*, **18**, 3953–3967, https://doi.org/10.1175/JCLI3483.1.

Lau, N.-C., 1979: The observed structure of tropospheric stationary waves and the local balances of vorticity and heat. *J. Atmos. Sci.*, **36**, 996–1016, https://doi.org/10.1175/1520-0469(1979)036<0996:TOSOTS>2.0.CO;2.

Livezey, R. E., and K. C. Mo, 1987: Tropical–extratropical teleconnections during the Northern Hemisphere winter. Part II: Relationships between monthly mean Northern Hemisphere circulation patterns and proxies for tropical convection. *Mon. Wea. Rev.*, **115**, 3115–3132, https://doi.org/10.1175/1520-0493(1987)115<3115:TETDTN>2.0.CO;2.

Mariotti, A., N. Zeng, and K.-M. Lau, 2002: Euro-Mediterranean rainfall and ENSO—A seasonally varying relationship. *Geophys. Res. Lett.*, **29**, 1621, https://doi.org/10.1029/2001GL014248.

Newman, P. A., and E. R. Nash, 2000: Quantifying the wave driving of the stratosphere. *J. Geophys. Res.*, **105**, 12 485–12 497, https://doi.org/10.1029/1999JD901191.

Nigam, S., 2003: Teleconnections. *Encyclopedia of Atmospheric Sciences*, J. R. Holton, J. A. Pyle, and J. A. Curry, Eds., Vol. 6, Academic Press, 2243–2269.

——, and S. Baxter, 2014: Teleconnections. *Encyclopedia of Atmospheric Sciences*, 2nd ed. G. North, F. Zhang, and J. Pyle, Eds., Academic Press/Elsevier Science, 90–109.

Poli, P., and Coauthors, 2016: ERA-20C: An atmospheric reanalysis of the twentieth century. *J. Climate*, **29**, 4083–4097, https://doi.org/10.1175/JCLI-D-15-0556.1.

Polvani, L. M., L. Sun, A. H. Butler, J. H. Richter, and C. Deser, 2017: Distinguishing stratospheric sudden warmings from ENSO as key drivers of wintertime climate variability over the

North Atlantic and Eurasia. *J. Climate*, **30**, 1959–1969, https://doi.org/10.1175/JCLI-D-16-0277.1.

Rayner, N. A., D. E. Parker, E. B. Horton, C. K. Folland, L. V. Alexander, D. P. Rowell, E. C. Kent, and A. Kaplan, 2003: Global analyses of sea surface temperature, sea ice, and night marine air temperature since the late nineteenth century. *J. Geophys. Res.*, **108**, 4407, https://doi.org/10.1029/2002JD002670.

Schneider, U., A. Becker, P. Finger, A. Meyer-Christoffer, B. Rudolf, and M. Ziese, 2011: GPCC full data reanalysis version 6.0 at 0.5°: Monthly land-surface precipitation from rain-gauges built on GTS-based and historic data. GPCC, accessed 20 January 2017, https://doi.org/10.5676/DWD_GPCC/FD_M_V7_050.

Sterl, A., G. J. van Oldenborgh, W. Hazeleger, and G. Burgers, 2007: On the robustness of ENSO teleconnections. *Climate Dyn.*, **29**, 469–485, https://doi.org/10.1007/s00382-007-0251-z.

Timmermann, A., and Coauthors, 2018: El Niño–Southern Oscillation complexity. *Nature*, **559**, 535–545, https://doi.org/10.1038/s41586-018-0252-6.

Trenberth, K. E., G. W. Branstator, D. Karoly, A. Kumar, N.-C. Lau, and C. Ropelewski, 1998: Progress during TOGA in understanding and modeling global teleconnections associated with tropical sea surface temperatures. *J. Geophys. Res.*, **103**, 14 291–14 324, https://doi.org/10.1029/97JC01444.

Vallis, G. K., 2006: *Atmospheric and Oceanic Fluid Dynamics*. Cambridge University Press, 745 pp.

——, and E. P. Gerber, 2008: Local and hemispheric dynamics of the North Atlantic Oscillation, annular patterns and the zonal index. *Dyn. Atmos. Oceans*, **44**, 184–212, https://doi.org/10.1016/j.dynatmoce.2007.04.003.

van Oldenborgh, G. J., G. Burgers, and A. Klein Tank, 2000: On the El Niño teleconnection to spring precipitation in Europe. *Int. J. Climatol.*, **20**, 565–574, https://doi.org/10.1002/(SICI)1097-0088(200004)20:5<565::AID-JOC488>3.0.CO;2-5.

Wallace, J. M., G. Lim, and M. L. Blackmon, 1988: Relationship between cyclone tracks, anticyclone tracks and baroclinic waveguides. *J. Atmos. Sci.*, **45**, 439–462, https://doi.org/10.1175/1520-0469(1988)045<0439:RBCTAT>2.0.CO;2.

Wang, H., and R. Fu, 2000: Winter monthly mean atmospheric anomalies over the North Pacific and North America associated with El Niño SSTs. *J. Climate*, **13**, 3435–3447, https://doi.org/10.1175/1520-0442(2000)013<3435:WMMAAO>2.0.CO;2.

Yang, X., and T. DelSole, 2012: Systematic comparison of ENSO teleconnection patterns between models and observations. *J. Climate*, **25**, 425–446, https://doi.org/10.1175/JCLI-D-11-00175.1.

Zhang, T., M. P. Hoerling, J. Perlwitz, and T. Xu, 2016: Forced atmospheric teleconnections during 1979–2014. *J. Climate*, **29**, 2333–2357, https://doi.org/10.1175/JCLI-D-15-0226.1.

Zhang, W., L. Wang, B. Xiang, L. Qi, and J. He, 2015: Impacts of two types of La Niña on the NAO during boreal winter. *Climate Dyn.*, **44**, 1351–1366, https://doi.org/10.1007/s00382-014-2155-z.

——, Z. Wang, M. F. Stuecker, A. G. Turner, F.-F. Jin, and X. Geng, 2019: Impact of ENSO longitudinal position on teleconnections to the NAO. *Climate Dyn.*, **52**, 257–274, https://doi.org/10.1007/s00382-018-4135-1.

Chapter 3

Multi-model assessment of the late-winter extra-tropical response to El Niño and La Niña

This chapter contains the research article Mezzina et al. 2021a and addresses objectives 1, 2 and 3 from Sect. 1.3.

Mezzina, B., García-Serrano, J., Bladé, I., Palmeiro, F. M., Batté, L., Ardilouze, C., Benassi, M., & Gualdi, S. (2021a). Multi-model assessment of the late-winter extra-tropical response to El Niño and La Niña. *Clim. Dyn.*, 1–22. https://doi.org/10.1007/s00382-020-05415-y

Climate Dynamics
https://doi.org/10.1007/s00382-020-05415-y

Multi-model assessment of the late-winter extra-tropical response to El Niño and La Niña

Bianca Mezzina[1] · Javier García-Serrano[1,2] · Ileana Bladé[2] · Froila M. Palmeiro[2] · Lauriane Batté[3] · Constantin Ardilouze[3] · Marianna Benassi[4] · Silvio Gualdi[4,5]

Received: 10 April 2020 / Accepted: 7 August 2020

Abstract
El Niño-Southern Oscillation (ENSO) is known to affect the Northern Hemisphere tropospheric circulation in late-winter (January–March), but whether El Niño and La Niña lead to symmetric impacts and with the same underlying dynamics remains unclear, particularly in the North Atlantic. Three state-of-the-art atmospheric models forced by symmetric anomalous sea surface temperature (SST) patterns, mimicking strong ENSO events, are used to robustly diagnose symmetries and asymmetries in the extra-tropical ENSO response. Asymmetries arise in the sea-level pressure (SLP) response over the North Pacific and North Atlantic, as the response to La Niña tends to be weaker and shifted westward with respect to that of El Niño. The difference in amplitude can be traced back to the distinct energy available for the two ENSO phases associated with the non-linear diabatic heating response to the total SST field. The longitudinal shift is embedded into the large-scale Rossby wave train triggered from the tropical Pacific, as its anomalies in the upper troposphere show a similar westward displacement in La Niña compared to El Niño. To fully explain this shift, the response in tropical convection and the related anomalous upper-level divergence have to be considered together with the climatological vorticity gradient of the subtropical jet, i.e. diagnosing the tropical Rossby wave source. In the North Atlantic, the ENSO-forced SLP signal is a well-known dipole between middle and high latitudes, different from the North Atlantic Oscillation, whose asymmetry is not indicative of distinct mechanisms driving the teleconnection for El Niño and La Niña.

Keywords ENSO · NAO · Atmospheric teleconnections · Climate modeling

1 Introduction

The teleconnection of El Niño-Southern Oscillation (ENSO) to the North Atlantic-European (NAE) sector is a long-explored topic that, however, is still controversial in several aspects. A first cornerstone on the topic—and starting point of this study—was set in a review by Brönnimann (2007), who concluded that a robust ENSO signal exists over the NAE region in late winter (January to March, JFM): a dipole in sea-level pressure (SLP) with centers over the mid-latitude and high-latitude North Atlantic (see "Appendix 1"). He referred to this signal as "canonical", though acknowledging the existence of other, "non-canonical" views. While Brönnimann (2007) described this canonical pattern as "*close to symmetric*" for El Niño and La Niña, recent studies revisiting the topic and targeting linearities/non-linearities deliver contradictory results, with some reporting a symmetric signal (e.g. Deser et al. 2017; Ayarzagüena et al. 2018; Weinberger et al. 2019) and others claiming asymmetry (e.g.

Electronic supplementary material The online version of this article (https://doi.org/10.1007/s00382-020-05415-y) contains supplementary material, which is available to authorized users.

✉ Bianca Mezzina
bianca.mezzina@bsc.es

[1] Barcelona Supercomputing Center (BSC), Barcelona, Spain

[2] Group of Meteorology, Universitat de Barcelona (UB), Barcelona, Spain

[3] CNRM, Université de Toulouse, Météo-France, CNRS, Toulouse, France

[4] Climate Simulations and Predictions Division, Fondazione Centro Euro-Mediterraneo sui Cambiamenti Climatici (CMCC), Bologna, Italy

[5] Istituto Nazionale di Geofisica e Vulcanologia, Bologna, Italy

Trascasa-Castro et al. 2019; Hardiman et al. 2019; Jiménez-Esteve and Domeisen 2019). The actual "linearity" of the ENSO-NAE teleconnection thus remains unresolved, and addressing this issue is the primary objective of this study.

Another key aspect of the ENSO-NAE teleconnection which is nothing but settled is the dynamical mechanism leading to the canonical SLP dipole. In particular, two main pathways are suggested for this teleconnection: via the troposphere and via the stratosphere. Regarding the tropospheric pathway, the poleward-propagating Rossby wave train (see "Appendix 1") driving the well-established teleconnection in the North Pacific (Trenberth et al. 1998), first described by Horel and Wallace (1981) and Hoskins and Karoly (1981), is a suitable candidate (e.g. García-Serrano et al. 2011; Mezzina et al. 2020), although other mechanisms have been proposed (e.g. Toniazzo and Scaife 2006; Jiménez-Esteve and Domeisen 2018). The stratospheric pathway would involve a response to ENSO in the extra-tropical stratosphere, typically consisting of changes in the strength of the polar vortex, followed by downward propagation of the anomalies into the troposphere that then trigger North Atlantic Oscillation (NAO)-like variability (see Domeisen et al. 2019 for a review). The two hypotheses are not mutually exclusive, and some studies suggest that El Niño and La Niña may have different preferred pathways, in particular when strong versus weak events are considered (e.g. Hardiman et al. 2019; Trascasa-Castro et al. 2019). The polar vortex response will be briefly examined in this study, which instead focuses on the tropospheric pathway. One of our objectives is to show that the canonical NAE signal associate with El Niño and La Niña can be mostly explained in terms of the same tropospheric dynamics.

The underlying idea of this study is to use idealized experiments with atmospheric models forced by *symmetric* anomalous SST patterns representing El Niño and La Niña to diagnose symmetries and asymmetries in the extra-tropical response. With this approach, potential asymmetries can be attributed purely to atmospheric processes and isolated from other effects related to the ENSO diversity (Capotondi et al. 2015). Previous studies adopted a similar method (e.g. Hoerling et al. 2001), including very recent ones (e.g. Jiménez-Esteve and Domeisen 2019; Trascasa-Castro et al. 2019), but, to the best of our knowledge, it is the first time that this is done in a multi-model framework. The experiments analyzed here are in fact run with the same protocol using three state-of-the-art models; that these models provide consistent results will add robustness to our conclusions. We aim not only at diagnosing asymmetries in the extra-tropical ENSO-related SLP signal, but also at understanding their cause by examining all the steps involved in the tropospheric pathway of the atmospheric response, starting from the tropical Pacific. The interaction of heat-induced anomalies in the tropical upper troposphere with the mean flow in the sub-tropics is key to understanding SST-forced teleconnections (Sardeshmukh and Hoskins 1988; Qin and Robinson 1993), and it will be carefully examined here in order to trace back the asymmetric behavior of the extra-tropical SLP response.

While we will present results for the entire Northern Hemisphere, including the North Pacific, our primary target is the NAE sector. For this reason, the study is based on late winter (JFM), when the canonical signal is more robust (Brönnimann 2007), since intra-seasonal changes between early winter (November–December) and late winter (January–February) occur (e.g. Moron and Gouirand 2003; Gouirand et al. 2007; Bladé et at. 2008; King et al. 2018; Ayarzaguena et al. 2018). Note that the use of different seasons across NAE-oriented studies may be contributing to the lack of agreement on the symmetric character of the teleconnection.

We will call *asymmetry* any deviation from what is expected to be a linear, symmetric behavior, i.e. an identical pattern with same amplitude but opposite sign for El Niño and La Niña. The term "non-linearity" is often used to describe these deviations but, in the context of the ENSO teleconnection, it may refer to several aspects: the impacts of El Niño versus La Niña (e.g. Hoerling et al. 1997), of strong versus moderate/weak events (e.g. Toniazzo and Scaife 2006), of different ENSO "flavors", such as the Central Pacific and Eastern Pacific El Niños (e.g. Capotondi et al. 2015). Garfinkel et al. (2019), for example, discuss all these aspects referring to them as "non-linearities". The last two issues—distinct flavors and strength—are intentionally left out in this work, which focuses on the response to strong, Eastern Pacific-like events of opposite polarity. In this context, the term "non-linearity" could be used without ambiguity, but we choose the more neutral "asymmetry" as it does not suggest the involvement of non-linear physical processes such as the triggering of different pathways.

Another point that will be addressed here, not concerning the asymmetries but of crucial importance for the full understanding of the canonical NAE dipole, is the relationship between the ENSO-forced variability in the Euro-Atlantic sector and the NAO. While Brönnimann (2007) already stressed that the canonical dipole resembles *"though not exactly"* the North Atlantic Oscillation, in the following years little effort was dedicated to distinguishing the canonical "NAO-like" dipole from the NAO itself (e.g. García-Serrano et al. 2011). Here, we adopt a complementary approach to confirm the results of Mezzina et al. (2020), who used reanalysis data and AMIP-like simulations to show that the ENSO-NAE teleconnection, despite some similarity at the surface, is dynamically distinct from the NAO.

After describing the models, experimental protocol and methods in Sect. 2, we examine the tropical and extra-tropical tropospheric response to El Niño- and La Niña-like

forcings across the three models (Sect. 3), and in Sect. 3.5 we compare it to the internal variability associated with the NAO. In Sect. 3.6, we discuss the stratospheric response to EN and LN, and also compare it with the NAO-related variability. We summarize and discuss our results in Sect. 4, while the main conclusions are provided in Sect. 5.

2 Data and Methods

2.1 Models and experimental set-up

All experiments analysed here are atmosphere-only simulations. The multi-model ensemble, contributing to the ERA4CS-funded MEDSCOPE project, consists of three state-of-the-art models. The first one is the atmospheric component of the climate model EC-EARTH3.2, the ECMWF Integrated Forecasting System (IFS) cycle 36r4, at T255 horizontal resolution (approx. 0.7° in longitude-latitude, ~ 80 km) with 91 vertical levels up to 0.01 hPa (see Davini et al. 2017 and Haarsma et al. 2020; hereafter *EC-EARTH*). The second one is the atmospheric component of the climate model CNRM-CM6-1, ARPEGE-Climat v6.3 at T127 horizontal resolution (~ 1.4° at the equator), also with 91 vertical levels up to 0.01 hPa (see Voldoire et al. 2019; Roehrig et al. 2020; hereafter *CNRM*). Lastly, the atmospheric component of the climate model CMCC-SPS3, CAM5.3, with a horizontal resolution of about 110 km and 46 vertical levels up to 0.3 hPa (see Sanna et al. 2017; hereafter *CMCC*).

The suite of experiments includes a control simulation and two perturbed runs. Observational SSTs (HadISST2.2; Titchner and Rayner 2014) are used to define the boundary conditions, and all radiative forcings are kept fixed at year 2,000 to represent present-day conditions and avoid the effect of long-term trends. The control simulation (CTL) is run with climatological SSTs computed over the period 1981–2010 and integrated for 50 years after spin-up. CTL is also used to provide atmospheric initial conditions for the sensitivity experiments. The latter are designed to study the forced response to symmetric warm and cold ENSO events. The El Niño experiment (EN) is performed with SST anomalies that mimic a strong, canonical eastern-Pacific El Niño event; the La Niña experiment (LN) has identical prescribed pattern but with flipped-sign SST anomalies, i.e. multiplied by − 1. The time-evolving anomalous SSTs, superimposed on the climatological condition of CTL, are built using linear regressions of detrended monthly SST anomalies onto the Niño3.4 index (area-averaged SST anomalies over 5°N–5°S;170°W–120°W) in DJF, and over the period 1981–2010 to ensure reliability and quality of data for the ENSO pattern in the satellite era. The EN/LN experiments are run for a complete ENSO cycle, from June 1st (year 0) to May 31st (year 1). The imposed SST anomalies are restricted to 20°S–20°N (see Fig. 1) and are augmented to reach a maximum amplitude of about 2.7 °C (2.4 °C) in DJF (JFM), similar to previous studies (e.g. Taguchi and Hartmann 2006), in order to compensate for the damping by surface heat fluxes that results from considering the ocean as an infinite reservoir of heat capacity (atmosphere-only simulations). The amplitude of the SST anomalies is realistic and comparable to the strongest observed El Niño events (1982/83, 1997/98, 2015/16).

2.2 Methods

The forced atmospheric response associated with El Niño (La Niña) is estimated by computing the difference between the ensemble mean of the 50 winters in EN (LN) and CTL; unless otherwise indicated (e.g. Sect. 3.5), we will refer to this response to EN/LN as *forced patterns* or *anomalies*. Several direct outputs of atmospheric fields are examined: sea-level pressure (SLP), 3D geopotential height (Z), and precipitation (PCP). Additionally, to assess the generation of anomalous vorticity that triggers the Rossby wave energy propagation (Sect. 3.3), we compute the Tropical Rossby Wave Source as:

$$TRWS = -v'_{\chi} \cdot \nabla\left(\bar{\zeta} + f\right)$$

where v'_{χ} is the anomalous divergent wind, $\bar{\zeta}$ is the climatological relative vorticity, and f is the planetary vorticity or Coriolis parameter (Sardeshmukh and Hoskins 1988; Qin and Robinson 1993); monthly zonal and meridional wind are used to first integrate the velocity potential χ from the divergence, and then to derive the divergent wind v_{χ} (e.g. Sardeshmukh and Hoskins 1987).

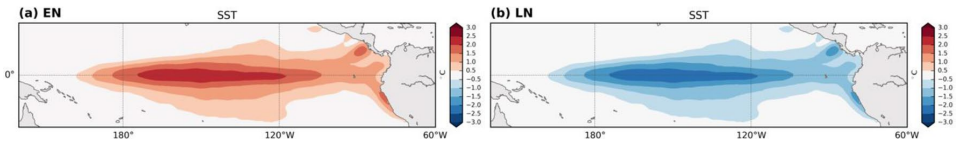

Fig. 1 JFM average of the SST anomalies prescribed in the **a** EN and **b** LN experiments

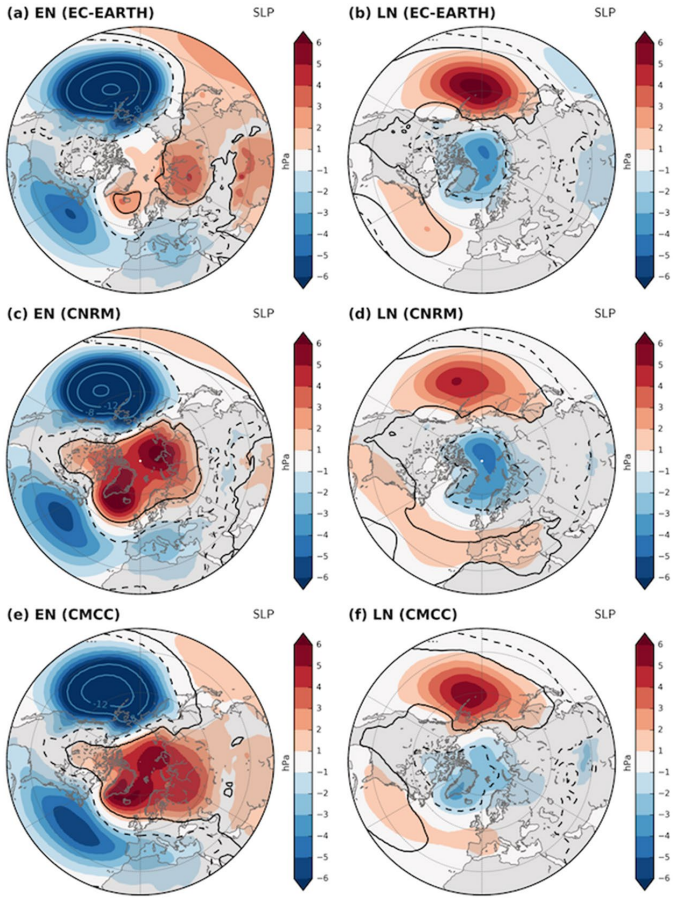

Fig. 2 Ensemble-mean SLP anomalies for (left) EN and (right) LN with respect to CTL in JFM: EC-EARTH (top), CNRM (middle), CMCC (bottom). Blue contours show values exceeding the color scale limit at − 8, − 12, − 16 hPa. Black contours (solid for positive, dashed for negative anomalies) indicate statistically significant areas at the 95% confidence level

In Sect. 3.5 we evaluate changes in storm-track activity by computing the Eddy Kinetic Energy at 500 hPa as (Hoskins et al. 1983; Trenberth 1986):

$$EKE = \frac{1}{2}\left(u'u' + v'v'\right)$$

where the covariances are computed from daily horizontal wind and applying the 24-h difference filter (e.g. Wallace et al. 1988; Chang et al. 2002) and then performing seasonal averages. Note that other diagnostics such as geopotential height variance at 500 hPa (Blackmon 1976; Lau 1988) or EKE at 200 hPa yield identical results.

CTL is used to study the unforced, internally-generated variability associated with the NAO (Sect. 3.5). Specifically, after defining the NAO index as the 1st Principal Component/EOF of SLP anomalies over the NAE region (20°N–90°N–90°W–40°E), its positive (NAO^+) and negative (NAO^-) phases are computed based on the upper and lower terciles of the index, respectively, from the 50 winters. Composite NAO^-–NAO^+ maps of different variables, thus displaying patterns with NAO^- polarity, are discussed in Sects. 3.5 and 3.6.

The zonal shift and amplitude ratio between the responses in EN and LN are quantified by first computing, separately in the two experiments, the coordinates of the strongest response in the examined region (x_{max}, y_{max}). For the shift, the difference between the longitudes ($x_{max}^{EN} - x_{max}^{LN}$) is evaluated, with positive values indicating an eastward shift in EN with respect to LN. For the ratio, the area-average over a box centered at (x_{max}, y_{max}) is used to estimate the amplitude of the response in EN and LN, and the ratio between them is computed (EN/LN). The box has varying size according to the variable: $x_{max} \pm 10°$ and $y_{max} \pm 5°$ for SLP and Z200; $\pm 5°$ in both directions for PCP; $x_{max} \pm 5°$ and $y_{max} \pm 2°$ for TRWS.

As stated in the Introduction, the target of the study is the late-winter ENSO teleconnection and hence all figures are presented for JFM. Statistical significance of the ENSO-forced response and NAO-related internal variability is assessed by applying a Student's *t*-test for the difference of means at the 95% confidence level. An *F*-test for the difference of variances is used in the case of the amplitude ratio, also at the 95% confidence level.

3 Results

3.1 Forced extra-tropical response: sea-level pressure

Looking for insights on the canonical ENSO-NAE teleconnection, we begin by examining the forced SLP patterns in the EN and LN experiments. All models agree in showing the strongest response over the North Pacific: the expected, well-documented deepening of the Aleutian Low in EN (Fig. 2a, c, e) and weakening in LN (Fig. 2b, d, f; e.g. Trenberth et al. 1998; Alexander et al. 2002). Two aspects stand out, given that these patterns are forced by symmetric SST anomalies: (i) the response in LN is much weaker, about half the amplitude of that in EN, and (ii) it is shifted westward with respect to that in EN by about 10°-20°, depending on the model. These features, which will also emerge in other regions and fields, are robust across the three models, and the differences between the forced patterns, namely the asymmetric component of the response (EN + LN), are mostly statistically significant (see Online Resource 1).

In the NAE sector, a dipole with centers of action in mid and high latitudes is present in both EN and LN, with opposite polarity, consistent with the canonical late-winter signature of ENSO (see Introduction). As in the North Pacific, a clear disproportion exists in terms of amplitude between EN and LN, while a westward longitudinal shift of about 20° is also present but not readily apparent due to the less defined nature of the anomalies in LN, probably linked to their weakness (see Sect. 3.4). Some inter-model variability is noticeable: the mid-latitude anomaly varies in shape and extent in LN, and in EN a distinct secondary center of action over the Mediterranean appears in EC-EARTH and CNRM, but not so clearly in CMCC. However, the fundamental structure of the El Niño and La Niña related patterns—i.e. the dipole over the North Atlantic—is consistent among the models.

The surface response to the symmetric ENSO forcing in the Northern Hemisphere thus appears to be roughly symmetric except for the two aspects mentioned above: the zonal shift and the amplitude difference.

3.2 Forced tropical response: convection

What is the origin of the zonal shift and amplitude difference of the extra-tropical ENSO teleconnection? To address this question, we take a step back and examine the deep convection response to the SST forcing in the tropical Pacific. While the prescribed anomalies are symmetric in the two sensitivity experiments (see Sect. 2), the total SST resulting from their combination with the climatology is obviously different; but the full SST field, and the total amount of heating provided, is what ultimately determines the development of tropical convection. First, a threshold of around 27 °C is required to trigger deep convection, both in observations (e.g. Graham and Barnett 1987) and models (e.g. Numaguti and Hayashi 1991), a condition that is fulfilled all over the tropical Pacific in EN (yellow contour in Fig. 3a, c, e) but only in the western part of the basin, over the Warm Pool, in LN (Fig. 3b, d, f). Second, tropical convection is related to low-level moisture convergence which is, in turn, affected by the SST gradient (e.g. Lindzen and Nigam 1987; Back and Bretherton 2009). Using total (not anomalous) precipitation as a proxy, we can confirm that the longitude of maximum convection is approximately located where the zonal gradient of SST changes sign (cf. shading and red/blue contours in Fig. 3). Thus, in EN the maximum precipitation north of the Equator is located east of the Date Line (around 170°W; Fig. 3a, c, e), in contrast to LN, which always shows a maximum west of it (around 160°E; Fig. 3b, d, f). In terms of anomalies with respect to CTL, convection/PCP is essentially weakened in LN, while it is enhanced but also shifted to the east in EN (not shown). Therefore, there is a westward shift of tropical convection in LN with respect to EN, consistent with what we noticed in the extra-tropical SLP patterns (Sect. 3.1). The longitudinal shift of the deep convection response, however, varies from 30° to 40°, depending on the model, almost twice the value of the SLP shift in the extra-tropics. The EN/LN amplitude asymmetry observed in the extra-tropical SLP is already apparent in the tropical response, since the precipitation amplitude in LN is about half that in EN, with the exception of CMCC, where they have comparable magnitudes (Fig. 3). Not surprisingly, the overall cooler tropical Pacific in LN provides less diabatic heating and promotes weaker convection with respect to EN, despite the symmetric anomalous SST forcing.

3.3 Forced tropical response: upper-level divergent wind and tropical Rossby wave source

The low-level convergence and associated rising motion are balanced at upper levels by divergent flow; hence, our next step is to examine the anomalous divergent wind (v'_χ) at 200 hPa, which is the level of approximate maximum outflow. In EN, the tropical Pacific is dominated by anomalous

equatorial divergence around 160°E–160°W, consistent with the reinforced convective activity there (cf. Fig. 3a, c, e and Fig. 4a, c, e); convergence is observed to the east and west, at around 100°E and 50°W, resulting from large-scale compensation (e.g. García-Serrano et al. 2017). In contrast, the suppression of climatological convection in LN is manifested as anomalous convergence over the western Pacific (Fig. 4b, d, f). There are, again, no striking differences among the models, except for the overall weaker signal in CMCC (in both EN and LN), in agreement with the response in precipitation.

Anomalous upper-level divergence is the essential trigger of the quasi-stationary large-scale Rossby wave train that constitutes the main extra-tropical response to ENSO (e.g. Trenberth et al. 1998); however, this is only part of the story. The generation of Rossby waves due to tropical heating can be described in terms of the Rossby Wave Source (RWS), a diagnostic that involves the interaction between divergence and vorticity (Sardeshmukh and Hoskins 1988). In particular, the most effective source to excite extra-tropical teleconnections is the advection of climatological vorticity by the anomalous divergent flow (Qin and Robinson 1993), called the tropical component of the Rossby Wave Source (TRWS; see Sect. 2.2). The TRWS is depicted in Fig. 4 (shading); for clarity, some anomalies are masked out in this figure, but the full TRWS is shown and discussed in "Appendix 2" (Fig. 12). The anomalies, with opposite sign, have roughly the same structure in EN and LN: a horseshoe-like pattern with maxima around 5°N and 30°N (the horseshoe shape in LN is not evident due the contour interval, see Fig. 12). These maxima can be explained by examining the two components of TRWS separately, v'_χ and $\nabla\left(\bar{\zeta}+f\right)$, shown in Fig. 13 of "Appendix 2". The gradient of climatological vorticity (computed from CTL) is small in the central tropical Pacific, close to the Equator, but this is where the strongest anomalous divergent wind is found. In contrast, the North Pacific jet is responsible for the strong gradient of climatological vorticity around 30°N that, combined with the moderate v'_χ anomalies there, generates the subtropical maximum in TRWS (cf. Figs. 4, 13). Note that the realistic zonally-asymmetric mean flow is what determines the "distorted" horseshoe-like shape of TRWS, which would tend to have zonally-aligned maxima otherwise (Qin and Robinson 1993; Ting 1996). Through the anomalous divergent wind, TRWS inherits part of the asymmetry between EN and LN observed in tropical convection. Using the TRWS maximum located at about 30°N as a reference, the TRWS anomalies in EN are 1 to 2.5 stronger than in LN—depending on the model—, similarly to the difference in precipitation. The zonal shift in convection and in the tropical divergent outflow, on the other hand, is mitigated by the interaction with the mean flow, whereby it decreases from 30° to 40° in precipitation to 20°–30° in TRWS (Fig. 4).

In line with the deep convection response, CMCC is showing a weaker signal compared to the other models in divergent wind and in the TRWS maximum around 5°N, in both EN and LN. The subtropical TRWS maximum, on the other hand, has similar amplitude in all the models. In addition, while in EC-EARTH and CMCC the TRWS anomaly linked to the jet is clearly stronger than the one in the tropics,

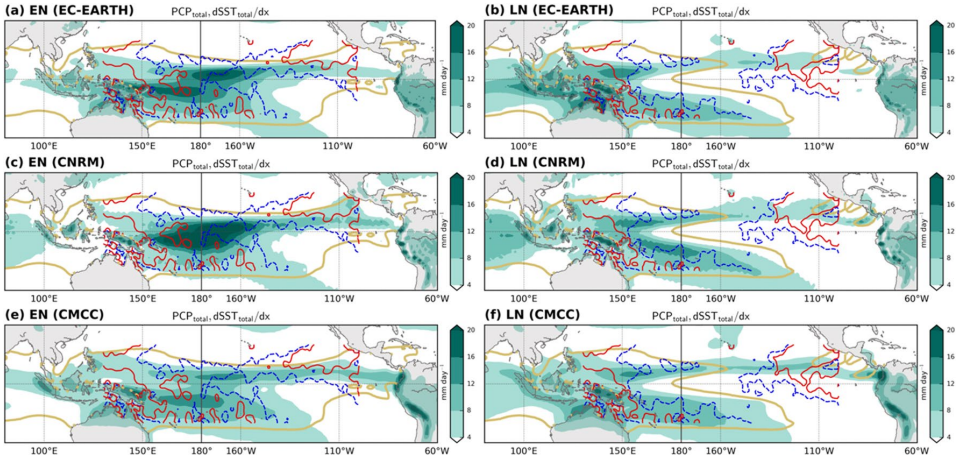

Fig. 3 Ensemble-mean PCP (shading), zonal SST gradient (red and blue contours, indicating +0.2 and −0.2 10^{-6} °C/m, respectively) and SST at 27 °C (yellow contour) for (left) EN and (right) LN in JFM: EC-EARTH (top), CNRM (middle), CMCC (bottom). For clarity, the zonal SST gradient is smoothed and only shown in the box 130°E–100°W; 20°S–20°N

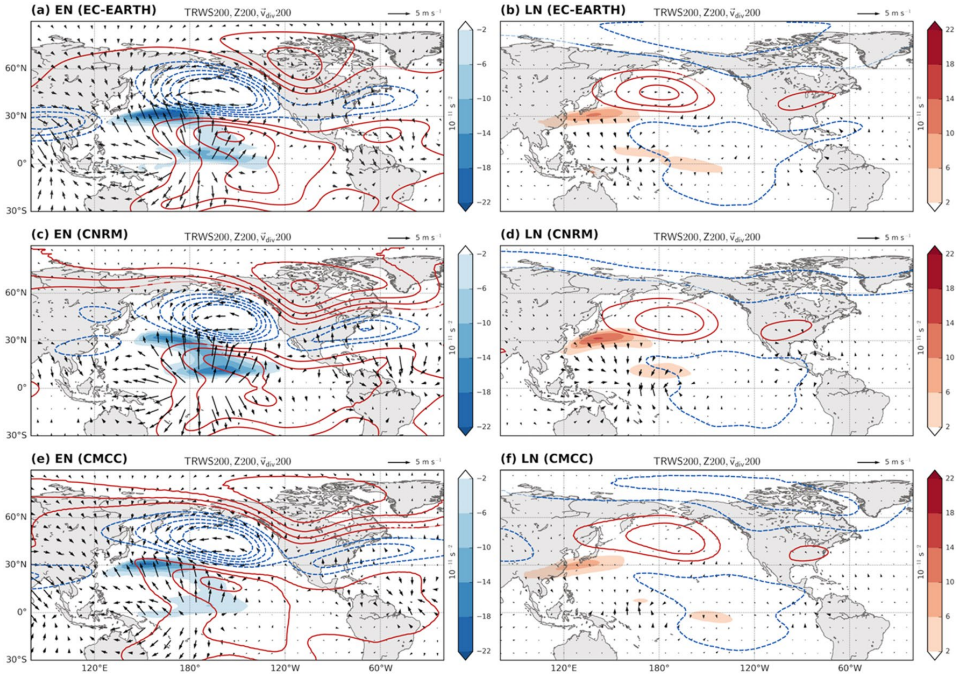

Fig. 4 Ensemble-mean 200-hPa TRWS (shading), divergent wind (arrows) and Z200 (contours; interval = 30 m) anomalies for (left) EN and (right) LN in JFM: EC-EARTH (top), CNRM (middle), CMCC (bottom). For TRWS, only the strongest negative (positive) anomalies in the tropical North Pacific are shown in EN (LN), see Fig. 12 for the full field. Only statistically significant TRWS and v'_χ anomalies (95% confidence level) are shown. For Z200, non-significant values are plotted with lighter contours

in CNRM the two appear to have comparable magnitude in EN, probably because of the very intense rainfall response and hence anomalous divergent wind (Fig. 4c).

3.4 ENSO-forced extra-tropical response: upper levels

After examining the Rossby Wave Source, the following step is to finally turn to the forced wave train itself. As it is conventionally detected in the upper-level (200 hPa) geopotential height, its anomalies for the two sensitivity experiments are shown as contours in Fig. 4. A succession of highs and lows curving away from the tropical Pacific is evident in both EN and LN, with opposite signs, forming the well-known arching wave train (e.g. Horal and Wallace 1981; Hoskins and Karoly 1981).

Starting from the ENSO region and focusing on the extra-tropics, poleward of 30°N, the first center of action is found in the North Pacific. In EN, it is centered east of the Date Line and extends up to the western coast of North America, while in LN it is shifted westward by about 10°–20°, roughly straddling the Date Line and reaching the western boundary of the basin. This well-known center of action is the upper-tropospheric counterpart of the SLP anomalies in the North Pacific (Aleutian Low) described in Sect. 3.1. The high (low) in EN (LN) approximately located over Canada and covering the polar region is the second center of action of the wave train; while in EN it has a clear center and consistent location across the models, it looks less defined in LN, particularly in the cylindrical projection that is used here. Finally, the tail of the wave train reaches the western mid-latitude North Atlantic in EN, but its LN equivalent is located inland over North America. There is some inter-model variability concerning this zonal shift, which ranges from 15° to 35°, but the shift is overall larger than the one in the North Pacific. On the other hand, the EN/LN asymmetry in amplitude is a common aspect to all the anomalies belonging to the wave train: the extra-tropical upper-level response in EN is about double the response in LN.

On a side note, we highlight that the tropical Gill-type response (Matsuno 1966; Gill 1980) does not exhibit a clear shift in longitude, but only weaker amplitude in LN compared to EN, consistent with the weaker signal in tropical convection.

3.5 ENSO-forced extra-tropical response: a closer look at the North Atlantic

The tail of the ENSO-induced wave train projects at the surface on the mid-latitude lobe of the SLP dipole in the North Atlantic discussed in Sect. 3.1. This is clearly revealed by computing height-longitude cross sections of the anomalous geopotential height averaged over the latitudinal band between 35°N–45°N, which is approximately where the Z200 and SLP mid-latitude anomalies are found in the NAE sector (Figs. 2, 4). The vertically tilted structure, depicted in Fig. 5, shows a maximum around 200 hPa that corresponds to the center of action over the western North Atlantic in Z200 (Fig. 4), while the amplitude decreases towards the surface, consistent with the fact that the maximum tropical outflow and thus the maximum TRWS occur at upper levels (Jin and Hoskins 1995; Ambrizzi and Hoskins 1997) and with the structure of balanced stationary waves in an atmosphere in which the zonal wind increases with height (Held et al. 2002). The SLP center over the mid-latitude North Atlantic (Fig. 2) is part of this 3-dimensional anomalous structure. In LN the vertical pattern is less defined, but the eastward shift of the surface response with respect to the upper-level maximum is still evident (Fig. 5b, d, f). In Fig. 5, the westward shift of the whole anomalous pattern in LN with respect to EN is consistent with those described in Sects. 3.1 and 3.4. The maximum at the surface in LN is not as evident as in EN (see also Fig. 2), but, if we follow the general westward tilt with height of the pattern and consider the maximum at upper levels, the longitude of the surface maximum can be estimated to be around 60°W (80°W) in EN (LN), implying a zonal shift of about 20°.

The westward tilt with height is an intrinsic feature of large-scale Rossby waves and it provides important information on the dynamics of the ENSO-related SLP dipole in the NAE sector, particularly in the context of the debate around its relationship with the NAO (see Introduction and Mezzina et al. 2020). To investigate this issue, we examine the NAO-related variability in the three models by considering the CTL experiment, where the variability is purely internal to the atmosphere (see Sect. 2). The distinctive signature of the NAO in SLP, a dipole in the North Atlantic, is accurately reproduced by all models (Fig. 6a, c, e). There is a certain similarity with the ENSO patterns of Fig. 2 (see also Fig. 11 in "Appendix 1"), but note how the NAO-related mid-latitude anomaly is centered around the zero Meridian, almost in quadrature with the ENSO-forced patterns, particularly for EC-EARTH (cf. Figs. 2, 6a). This surface pattern is accompanied by upper-level anomalies (Z200) that are essentially barotropic, with no vertical tilt, over the North Atlantic (Fig. 6b, d, f) and are reminiscent of the circumglobal waveguide pattern on the hemispheric scale (Branstator 2002). Extending the analysis to transient-eddy activity, the NAO meridionally shifts the storm tracks reaching western Europe, leading to a wet-dry dipole in precipitation there (Fig. 7c, f, i). In contrast, the impact of ENSO is more limited to the North Atlantic Ocean (left and middle columns of Fig. 7), with its maximum anomaly in EKE located approximately at the node of the NAO signal. This longitudinal distinction between the ENSO-forced and NAO-related patterns is robust across the models and statistically significant (not shown).

3.6 ENSO-forced extra-tropical response: lower stratosphere

Following the numerous studies suggesting that the ENSO-NAE teleconnection may be, partially or totally, driven by the stratospheric pathway (see Introduction), it is worth exploring the models' response in the lower polar stratosphere (50 hPa geopotential height, Z50; e.g. Ineson and Scaife 2009). In Fig. 8 (left and middle columns), displaying Z50 anomalies, it can be seen that the models show a signal consistent with previous studies (see Brönnimann 2007 for a review): a dominant positive (negative) anomaly in EN (LN) indicating the weakening (strengthening) of the polar vortex, accompanied with weaker, opposite-singed centers of action over the North Pacific and North Atlantic. The signal is roughly symmetric in sign, but the vortex response in EN is stronger than in LN, with the exception of EC-EARTH (Fig. 8a, b) where the positive anomaly in EN is rather weak and confined to central-northern North America, similarly to the corresponding center of action in Z200 (cf. Figs. 4a, 8a). The three models agree in the North Pacific, where the signal is consistent with the tropospheric wave train, displaying a similar longitudinal shift and a slightly weaker magnitude in LN with respect to EN, suggesting a tropospheric origin of the Z50 anomalies.

Less consistency is found in the North Atlantic, where a significant signal in LN is present only in CMCC, roughly symmetric to EN (cf. Fig. 8g, h), although all three models yield the canonical SLP dipole (Fig. 2). But it is actually in the NAE sector where the stratosphere is suggested to play an important role, a hypothesis mainly inspired by the tendency of stratospheric vortex anomalies to project onto dipolar, NAO-like patterns on seasonal time scales (e.g. Hitchcock and Simpson 2014; see Kidston et al. 2015 for a review). For this reason, similarly to the previous section, we also examine the NAO-related variability in CTL. The strongest center of action is still in the polar vortex (Fig. 8c, f, i), but the shape of the circulation anomalies is different than the ENSO-forced response: the configuration of the anomalous vortex in the NAO pattern covers the whole polar cap but is elongated along the axis western North Atlantic-eastern Eurasia (Fig. 8c, f, i), while in EN and LN the vortex anomalies are confined to the western hemisphere (left

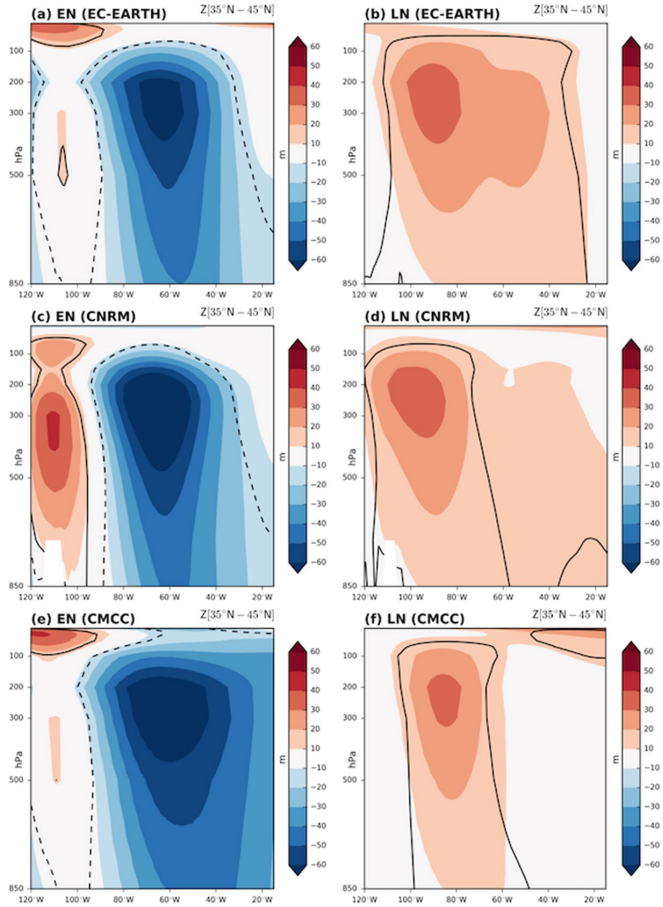

Fig. 5 Longitude-height cross section of ensemble-mean geopotential height anomalies for (left) EN and (right) LN with respect to CTL in JFM, averaged over the latitudinal band 35°N–45°N: EC-EARTH (top), CNRM (middle), CMCC (bottom). Black contours (solid for positive, dashed for negative anomalies) indicate statistically significant areas at the 95% confidence level

and middle columns of Fig. 8), except for EN in CNRM (Fig. 8d). These differences can be emphasized with a wavenumber decomposition of the patterns, which shows that the wavenumber-1 component of EN and LN is almost in quadrature with the NAO-related component (Fig. 9). A similar orthogonality of the patterns is also found in the wavenumber-2 component (see "Appendix 3").

4 Summary and discussion

To guide the discussion, we summarize our results in a schematic figure (Fig. 10). For each model and variable examined (PCP, SLP, TRWS, SLP, Z200), we build a scatter plot of the longitudinal shift in LN relative to EN versus the ratio of the amplitudes, computed as described in Sect. 2.2. For clarity, we consider the North Pacific (Fig. 10a) and the North Atlantic (Fig. 10b) separately and focus on the mid-latitude response. The two panels thus show the same points for TRWS and PCP, which represent the response over the tropical Pacific, but different ones for SLP and Z200, which describe the mid-latitude signal in the two regions. Note that we used the subtropical maxima of TRWS (at 30°N) to encapsulate the behavior of the TRWS anomalies, as this maximum is more clearly defined than the one in the equatorial region. The purpose of this figure is not to find a relationship between the shift and ratio, but to summarize how the fields behave in response to the symmetric forcing mimicking El Niño and La Niña.

The left panel describes the asymmetric behavior in the North Pacific (blue symbols), in terms of both amplitude, with EN showing anomalies 2–3 times larger than LN, and location, with a shift of 10°–20° (Fig. 10a). This result, which applies to strong El Niño- and La Niña-like SST

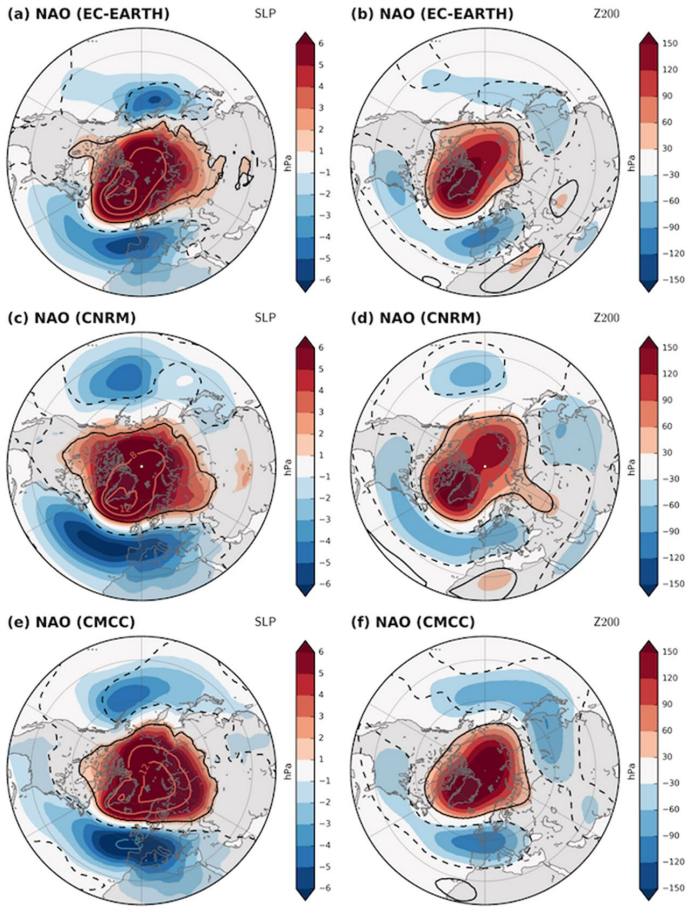

Fig. 6 SLP (left) and Z200 (right) composites of NAO^{-}–NAO^{+} for CTL in JFM: EC-EARTH (top), CNRM (middle), CMCC (bottom). Red and blue contours show values exceeding the color scale limit at ± 8, ± 12, ± 16 hPa. Black contours (solid for positive, dashed for negative anomalies) indicate statistically significant areas at the 95% confidence level

forcings, is in agreement with previous works using similar sensitivity experiments (e.g. Hoerling et al. 1997, 2001; Sardeshmukh et al. 2000; Jiménez-Esteve and Domeisen 2019; Tracasa-Castro et al. 2019) but is in conflict with Rao and Ren (2016b), who reported no asymmetry for strong events. In the same study, however, Rao and Ren observed asymmetries in coupled experiments for both the strong and moderate case. On the other hand, the composites in Garfinkel et al. (2019), who used AMIP-like experiments, also show a longitudinal shift and amplitude difference between El Niño and La Niña (see their Fig. 1), although the authors do not comment on them. Observational studies using reanalysis data deliver mixed conclusions as well. De Weaver and Nigam (2002) found a symmetric upper-level response with only a small longitudinal shift (~10°), while Deser et al. (2017) report no significant nonlinearities in SLP and only indicate regional differences in amplitude, although their results show a zonal shift consistent with the one found here (see their Fig. 10). Composites using ECMWF ERA-20CR in JFM lead to a similar result, with minor—but significant—differences in the North Pacific (see "Appendix 4"). In contrast, Hoerling et al. (1997, 2001) and Rao and Ren (2016a) point out clear asymmetries. With some limitations, discussed below, our study advocates for an asymmetric response to El Niño and La Niña in sea-level pressure, which is directly inherited from the upper tropospheric Rossby wave train (cf. SLP and Z200 in Fig. 10a). Convection in the tropical Pacific appears to be the primary source of this asymmetry, but with an even larger shift (Fig. 10a, green). Once the interaction between the anomalous tropical divergence and the climatological vorticity is considered via the TRWS (Fig. 10a, red), the shift is reduced and approaches that in SLP and Z200, with the three variables tending to cluster in the scatter plot.

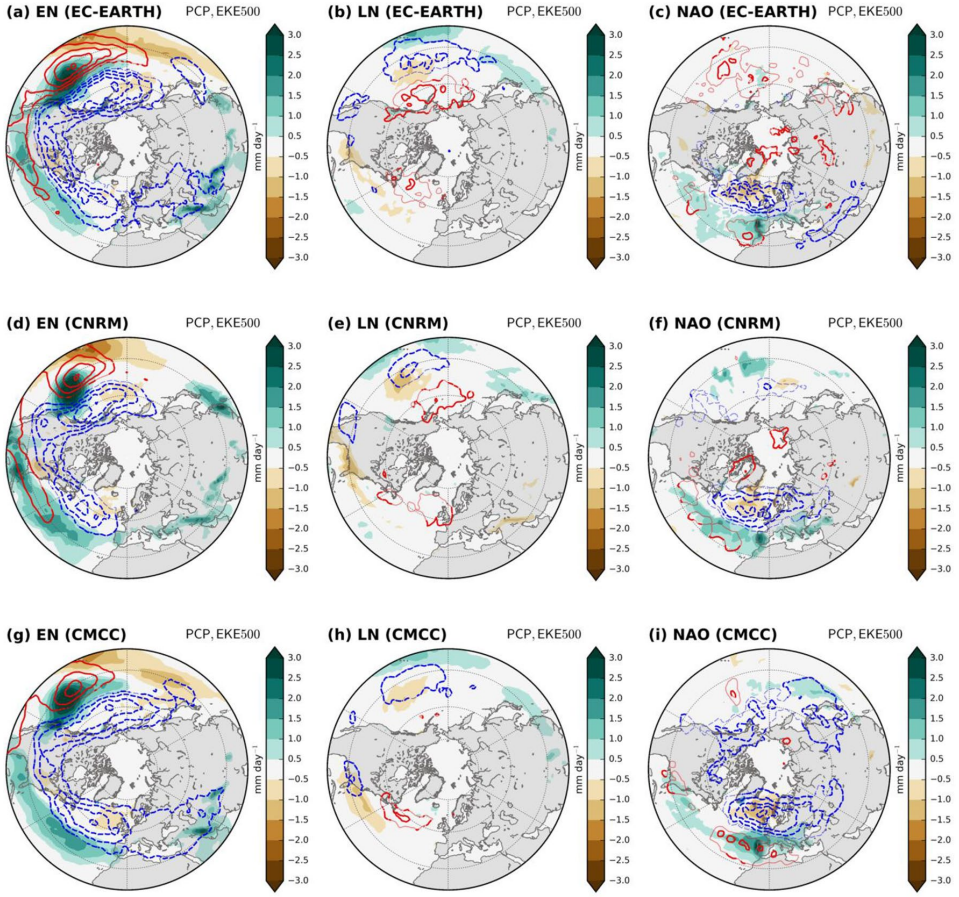

Fig. 7 Left and middle columns: ensemble-mean PCP (shading) and 500-hPa EKE (contours; interval = 8 m^2s^{-2}) anomalies for EN (left) and LN (right) with respect to CTL in JFM: EC-EARTH (top), CNRM (middle), CMCC (bottom). Right column: same, but for NAO^-–NAO^+ in CTL. Only statistically significant PCP anomalies (95% confidence level) are shown. For EKE, non-significant values are plotted with lighter contours

While some consistent asymmetries are still present, the overall picture in the North Atlantic is not as clear as in the North Pacific (Fig. 10b). Z200 has a ratio comparable to the North Pacific, around 2, but larger values and spread for the shift, which ranges from 15° to 35°. For two of the models, the shift is closer to that of TRWS than to that in precipitation (not so in CNRM), confirming the importance of the interplay between the anomalous tropical divergence and the mean flow. The large deviation of SLP from the rest of the variables in the scatter plot is linked to the ratio rather than the shift, partly because the upper-level Rossby wave train in LN projects onto land at the surface, tending to vanish (Fig. 5; e.g. Branstator 2002) and partly because of the large internal atmospheric variability in the region (e.g. Deser et al. 2017). Most observational studies indicate a large degree of linearity of the ENSO-NAE teleconnection in late-winter, such Ayarzagüena et al. (2018), although an amplitude asymmetry is present in their composites, and Brönnimann (2007). Focusing on DJF, Deser et al. (2017) found minor, non-significant asymmetries consistent with those in Fig. 15 for JFM, while the monthly maps of Jiménez-Esteve and Domeisen (2018) display a complex, non-linear response from December to March. For Zhang et al. (2019), who separate Central Pacific and Eastern Pacific events, there is no linearity at all for the latter (in JFM). Works using simulations and specifically addressing asymmetries in the North Atlantic are relatively limited in number. Earlier studies include Sardeshmukh et al. (2000) and Pozo-Vazquez et al. (2001), who reported asymmetries in the region, and recently a renewed interest in this topic has

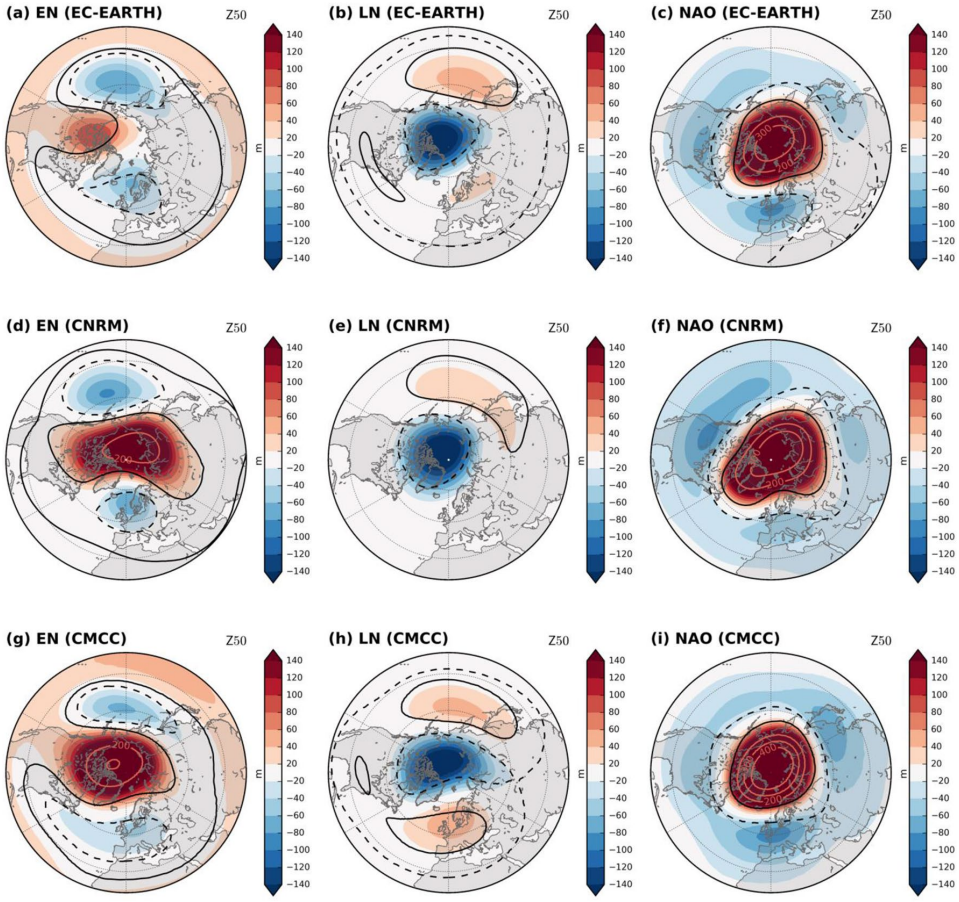

Fig. 8 Left and middle columns: ensemble-mean Z50 anomalies for EN (left) and LN (right) with respect to CTL in JFM: EC-EARTH (top), CNRM (middle), CMCC (bottom). Right column: same, but for NAO^{-}–NAO^{+} in CTL. Red and blue contours show values exceeding the color scale limit at ±200, ± 300, ± 400 m. Black contours (solid for positive, dashed for negative anomalies) indicate statistically significant areas at the 95% confidence level

arisen. Jiménez-Esteve and Domeisen (2019), using a set-up similar to ours but with an intermediate-complexity model, identified asymmetries in the North Atlantic for strong ENSO events, but did not discuss their origin in depth. Trascasa-Castro et al. (2019), Hardimann et al. (2019) and Weinberger et al. (2019), using sensitivity experiments, coupled models and AMIP-like simulations, respectively, reached contrasting conclusions: asymmetry in the first two cases and symmetry in the latter. A common aspect to these three studies, in spite of the different results, is the analysis and discussion of the role of the polar stratosphere. In particular, Weinberger et al. (2019) report no significant "non-linearity" in the presumed stratospheric pathway to the NAE in winter, but a weaker amplitude in the tropospheric circulation for La Niña compared to El Niño is present in their composites (see their Fig. 1).

Our results suggest that asymmetries are present in the NAE region associated with strong El Niño- and La Niña-like SST patterns in terms of amplitude and zonal shift, but the structure of the SLP pattern is similar and driven by the same dynamics: the dipolar pattern, consistent with the canonical view of Brönnimann (2007), is associated with the tropospheric Rossby wave train and its westward tilt with height (Fig. 5). In addition, comparison of the ENSO- and NAO-related patterns in SLP, Z200, transient-eddy activity and precipitation in the forced and control experiments indicate dynamical differences between the ENSO-NAE teleconnection and the NAO (Figs. 6, 7), supporting the conclusions

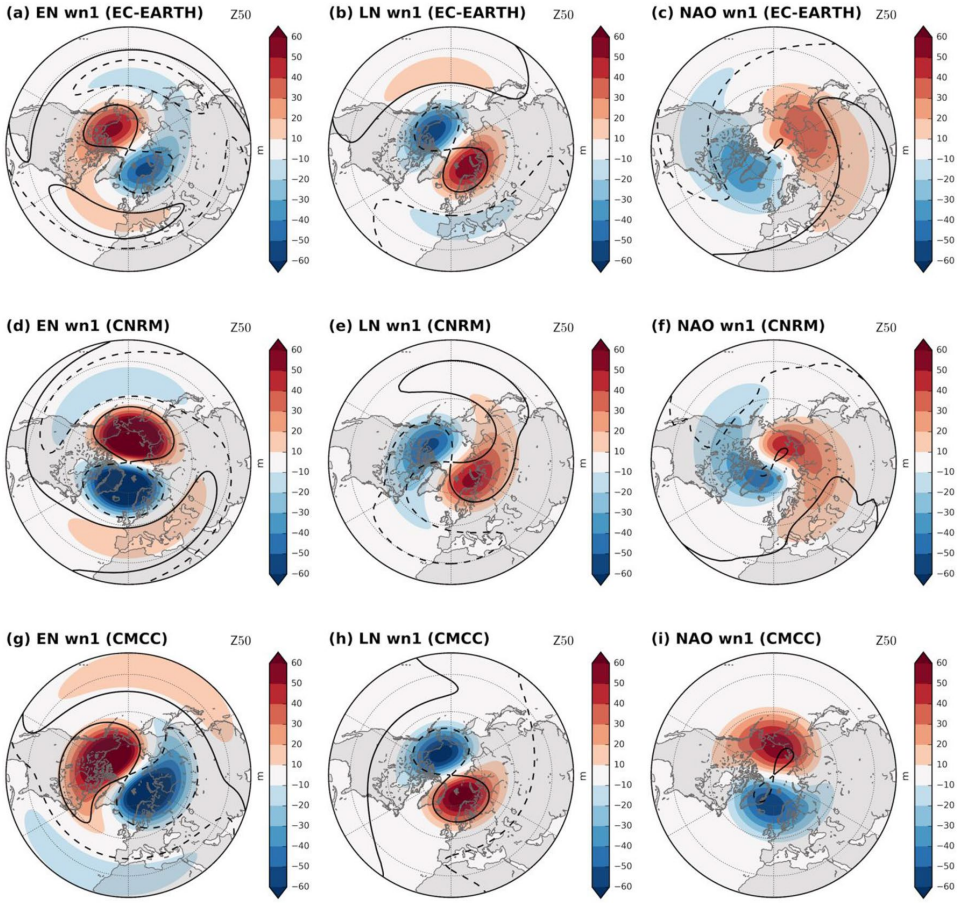

Fig. 9 Left and middle columns: wavenumber-1 component of the ensemble-mean Z50 anomalies for EN (left) and LN (right): EC-EARTH (top), CNRM (middle), CMCC (bottom). Right column: same, but for NAO^-–NAO^+ in CTL. Black contours (solid for positive, dashed for negative anomalies) indicate statistically significant areas at the 95% confidence level

of Mezzina et al. (2020) based on reanalysis and AMIP-like experiments. The stratospheric response to ENSO, which is quite linear in sign but with a consistent asymmetry in amplitude (Fig. 8), does not project onto the NAO-related pattern either; instead, their wavenumber-1 and 2 components are largely orthogonal (Figs. 9, 14).

Note that, when discussing the asymmetries, we do not examine in-depth the other lobe of the NAE dipole—the one at high latitudes—because of its distorted structure at the surface. However, we consider that the two opposite-signed anomalies over the North Atlantic belong to the same dipolar system and are primarily driven by the same tropospheric dynamics, i.e. the Rossby wave train triggered from the tropical Pacific. Therefore, we draw our conclusions indistinctly for the entire dipole of the ENSO-NAE teleconnection.

Some notes on the strength and limitations of the experimental set-up follow. The anomalous SST patterns prescribed as forcing are built from linear regression onto the Niño3.4-index and the same shape, with flipped sign, is used to represent El Niño and La Niña. Several studies adopted the same approach (e.g. Hoerling et al. 2001; Rao and Ren 2016b; Jiménez-Esteve and Domeisen 2019; Tracasa-Castro et al. 2019), which here we justify by the aim of focusing on asymmetries arising from one source only, i.e. cooling versus warming of the tropical Pacific, while excluding other factors such as pattern diversity, variations in timing and SST amplitude differences. More importantly, not only are El Niño and La Niña represented with the same spatial pattern, but also with same amplitude, in contrast with the observed skewness: indeed, La Niña events comparable to

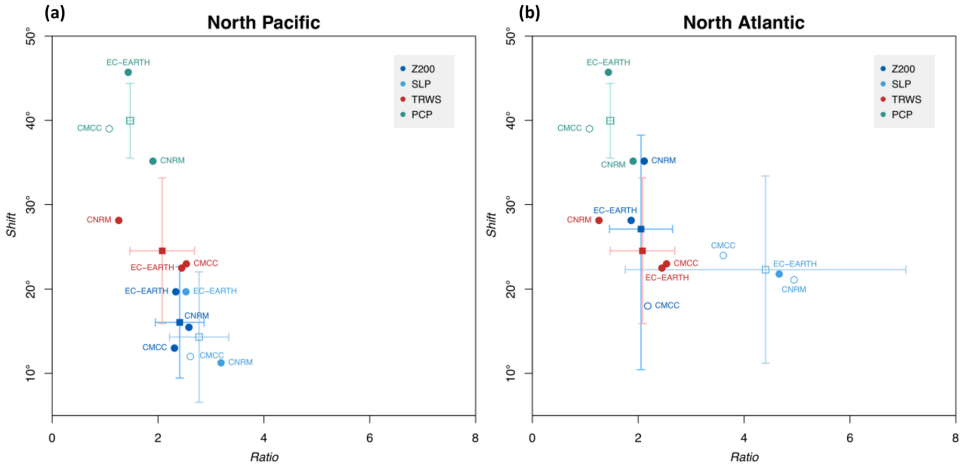

Fig. 10 Shift-ratio scatter plots summarizing the asymmetries in the EN and LN experiments. The maximum response in EN and LN is considered. The horizontal axis indicates the ratio of the amplitudes (EN/LN, positive sign), while the vertical axis represent the longitudinal shift in LN relative to EN. The response over the tropical Pacific is considered for PCP and TRWS, and over the mid-latitude North Pacific (left) and North Atlantic (right) for SLP and Z200. See text for details. Unlabeled squares represent the multi-model ensemble mean. All points are significant at the 95% confidence level for the shift, while empty circles and squares indicate variables that do not pass the significance test for the ratio. Error bars indicate $\pm 0.5\sigma$ for the multi-model mean

the strongest El Niños are not present in the observational records (e.g. Burgers and Stephenson 1999; Timmermann et al. 2018). Recently, Hardiman et al. (2019) emphasized this lack of "strong" La Niñas in observations and stressed the need to fill this gap with model studies, as such events may happen in the future. "Unrealistically" strong La Niñas are also considered in Jiménez-Esteve and Domeisen (2019) and Tracasa-Castro et al. (2019). As discussed above, these and other similar studies deliver contrasting conclusions concerning the asymmetric response to strong and weak El Niño versus La Niña, particularly in the North Atlantic, stressing the need to further investigate the dynamics of the atmospheric teleconnection of strong ENSO events of both signs. In this context, our study provides relevant contributions to address this gap, with consistent results that are supported by three different state-of-the-art models.

Finally, note that in the analysis of the Rossby Wave Source (Sect. 3.3) we did not include its extra-tropical component, ERWS $= -(\zeta + f)\nabla \cdot v'_\chi$, as it is considered to be part of the response and associated with wave propagation (Qin and Robinson 1993; Ting 1996). Works including both terms suggest another source region in the Gulf of Mexico/Caribbean Sea to explain the ENSO-forced SLP dipole in the NAE sector (e.g. Hardiman et al. 2019). This source, which is present in our experiments (see ERWS in Online Resource 2) and also reflected in TRWS (Fig. 12), is related to the large-scale response of the Atlantic Hadley cell to the ENSO-induced changes in convection over northern South America (e.g. Wang 2005; García-Serrano et al. 2017), but is located downstream of the Rossby wave train crossing the North Pacific (Fig. 4) that is our target. On the other hand, notice that the zonal shift described for TRWS, underlying the longitudinal shift in the ray path of EN/LN, is mirrored in ERWS as both follow the displacement of the Pacific Hadley cell in response to ENSO, the former over the subtropics and the latter in the extra-tropics (north of 30°N).

5 Conclusions

Analyzing sensitivity experiments with symmetric SST forcing mimicking strong warm and cool ENSO events, and using three state-of-the-art models, we draw the following conclusions:

- Even in the presence of a symmetric forcing, asymmetries arise in the SLP response over both the North Pacific (Aleutian Low) and NAE sector (North Atlantic dipole). The response to La Niña SST anomalies tends to be weaker and shifted westward relative to the one associated with El Niño anomalous forcing. This asymmetry is mostly inherited from the large-scale extra-tropical Rossby wave train excited in the upper troposphere.
- The response of tropical convection to the SST forcing is the underlying cause for the extra-tropical asymmetries. Warm (cold) SST anomalies during EN (LN) superimposed onto the mean state enlarge (restrict) the region suitable for the triggering of deep convection (SST above

27 °C) and increase (decrease) the amount of available diabatic heating, while the longitude of maximum convection is found east (west) of the Date Line due to the different SST gradient.

- The anomalous deep convection triggers a similarly shifted anomalous divergent wind response. In order to explain the more modest longitudinal shift of the extra-tropical SLP signal, the anomalous divergence needs to be considered in tandem with the mean flow (Rossby Wave Source).
- The ENSO surface signal in the NAE sector is the "canonical" dipole between mid and high latitudes, with asymmetries in terms of amplitude and longitude but not structure. These asymmetries are not indicative of different mechanisms driving the teleconnection for El Niño and La Niña. Instead, in both cases the ENSO teleconnection to the North Atlantic is mainly associated with the downstream part of the Rossby wave train from the tropical Pacific and its tilt with height, and it is unrelated to the NAO dynamics.

Our results show that ENSO does not trigger NAO-related variability neither in the troposphere nor in the stratosphere, thus questioning the view of the ENSO-NAE teleconnection as an excitation of the NAO via the stratosphere. Hence, we suggest that the dynamics of the stratospheric pathway may need to be revisited.

Finally, we remark on an issue that was mentioned in Sect. 3.4: the tropical signal in Z200, which does not display a clear zonal shift between EN and LN, unlike the extra-tropical one (Fig. 4). The theoretical frameworks describing the tropical Gill-type response and the extra-tropical Rossby wave train are distinct, the former being largely baroclinic and the latter barotropic (e.g. Lee et al. 2009; Ting 1996) and it is not clear whether they are part of the same global-scale response. As remarked by De Weaver and Nigam (2002), the equatorial response has received little attention and still, 18 years later, a satisfactory description reconciling the tropical and extra-tropical responses is missing.

Acknowledgements This work was supported by the MEDSCOPE project. MEDSCOPE is part of ERA4CS, an ERA-NET initiated by JPI Climate, and funded by AEMET (ES), ANR (FR), BSC (ES), CMCC (IT), CNR (IT), IMR (BE) and Météo-France (FR), with co-funding by the European Union (Grant 690462). B.M. and J.G.-S. were supported by the "Contratos Predoctorales para la Formación de Doctores" (BES-2016-076431) and "Ramón y Cajal" (RYC-2016-21181) programmes, respectively. F.M.P. was partially supported by the Spanish DANAE (CGL2015-68342-R) and GRAVITOCAST (ERC2018-092835) projects. Technical support at BSC (Computational Earth Sciences group) is sincerely acknowledged. We also thank four anonymous reviewers for their valuable insights.

Appendix

Appendix 1: Linear response

Figure 11 shows the linear component of the ENSO response in SLP and Z200, i.e. ensemble-mean differences between EN and LN. The benchmarks of the ENSO-NAE teleconnection discussed in the Introduction, the SLP dipole and the large-scale Rossby wave train, are evident in the three models.

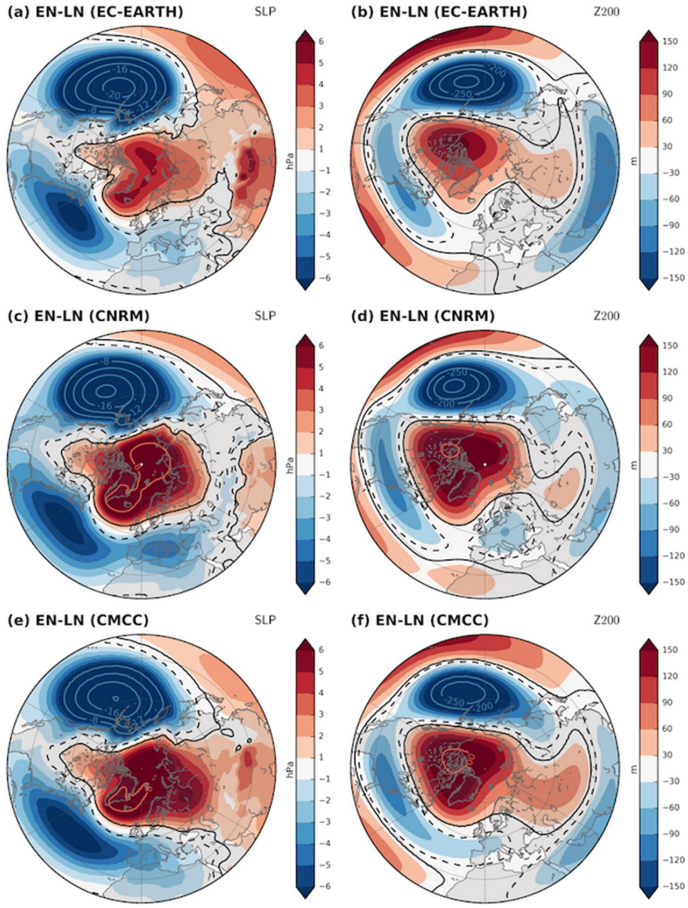

Fig. 11 Ensemble-mean SLP (left) and Z200 (right) differences between EN and LN in JFM: EC-EARTH (top), CNRM (middle), CMCC (bottom). Red and blue contours show values exceeding the color scale limit at ± 8, ± 12, ± 16, ± 20 hPa (SLP) and ± 200, ± 250, ± 300 m (Z200). Black contours (solid for positive, dashed for negative anomalies) indicate statistically significant areas at the 95% confidence level

Appendix 2: Full TRWS and TRWS components

Figure 12 complements Fig. 4 by depicting the full TRWS anomalies (only statistically significant values are shown); the contours are adapted to show the horseshoe-like pattern in LN.

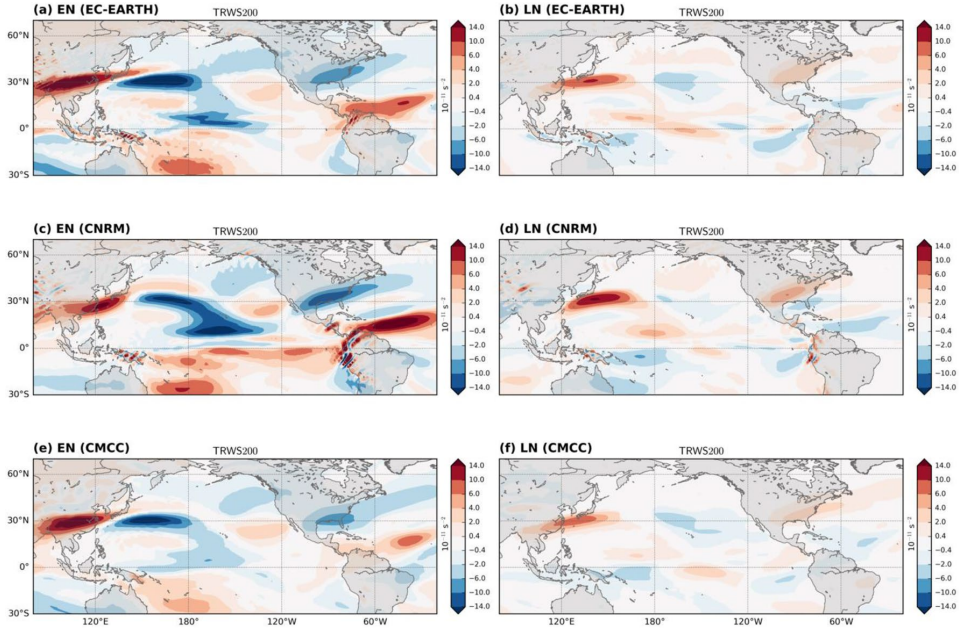

Fig. 12 Ensemble-mean 200-hPa TRWS anomalies for (left) EN and (right) LN with respect to CTL in JFM: EC-EARTH (top), CNRM (middle), CMCC (bottom). Only statistically significant anomalies (95% confidence level) are shown. Anomalies are smoothed in CMCC for clarity

Figure 13 is provided to help the interpretation of the TRWS response by displaying separately its components, v'_χ and $\nabla\left(\bar{\zeta}+f\right)$.

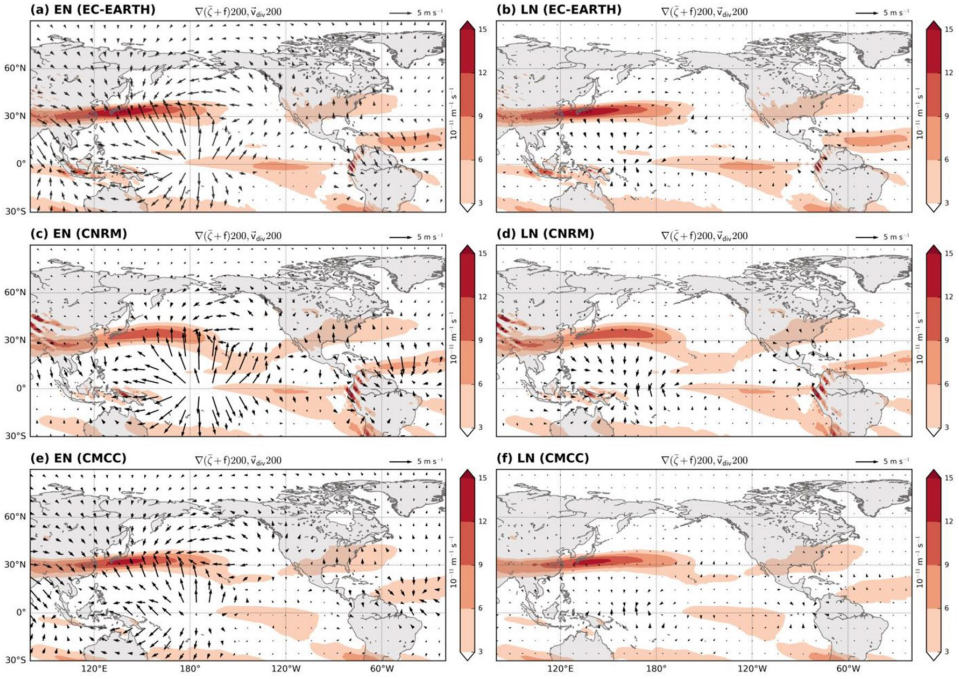

Fig. 13 Gradient of climatological vorticity in CTL (shading) and ensemble-mean 200-hPa divergent wind anomalies for (left) EN and (right) LN with respect to CTL (arrows) in JFM: EC-EARTH (top), CNRM (middle), CMCC (bottom)

Appendix 3: wavenumber-2 components of Z50

Figure 14 displays the wavenumber-2 component of EN and LN (left and middle column) in comparison with the NAO-related component.

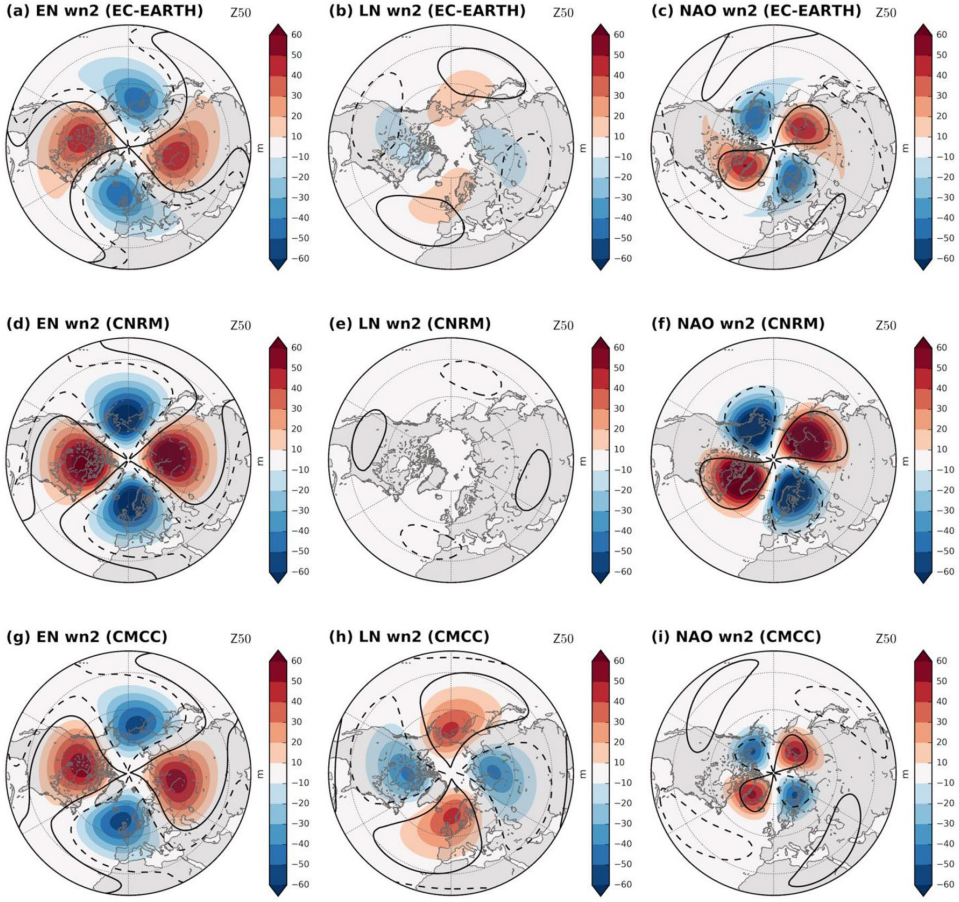

Fig. 14 Same as Fig. 9, but for the wavenumber-2 components

Appendix 4: Observational composites

Figure 15 shows JFM composites of El Niño (top left) and La Niña (top right) SLP anomalies using data from ECMWF ERA-20C (Poli et al. 2016) over 1900–2010. The composites are built according to the JFM Nino3.4-index computed from HadISST1.1, with El Niño (La Niña) years identified when $+1$ (-1) standard deviation is exceeded (18 EN and 19 LN years). The bottom panels display the symmetric (left) and asymmetric (right) components of the response.

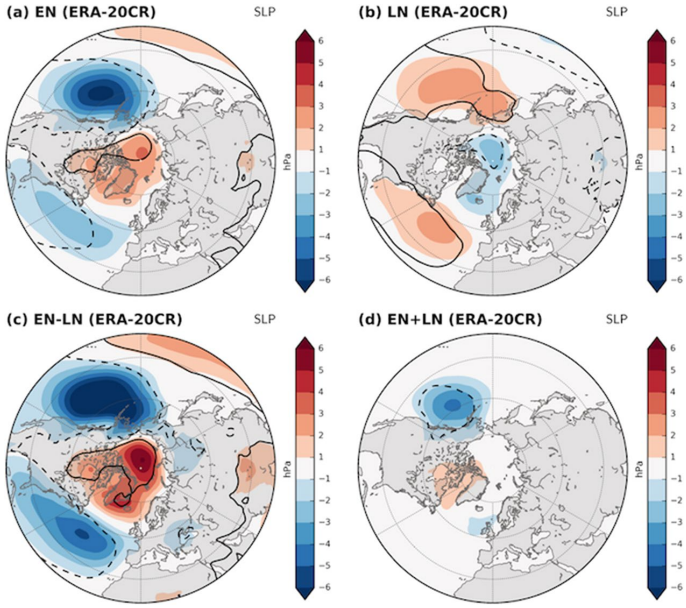

Fig. 15 Top: JFM composites of **a** El Niño **b** La Niña **c** El Niño-La Niña and **d** El Niño + La Niña anomalies using SLP data from ECMWF ERA-20C (Poli et al. 2016) over 1900–2010. Black contours (solid for positive, dashed for negative anomalies) indicate statistically significant areas at the 95% confidence level

References

Alexander MA, Bladé I, Newman M, Lanzante JR, Lau N-C et al (2002) The atmospheric bridge: the influence of ENSO teleconnections on air–sea interaction over the global oceans. J Clim 15:2205–2231. https://doi.org/10.1175/1520-0442(2002)015,2205:TABTIO.2.0.CO;2

Ambrizzi T, Hoskins BJ (1997) Stationary Rossby-wave propagation in a baroclinic atmosphere. Q J R Meteorol Soc 123:919–928. https://doi.org/10.1002/qj.49712354007

Ayarzagüena B, Ineson S, Dunstone NJ, Baldwin MP, Scaife AA (2018) Intraseasonal Effects of El Niño–Southern Oscillation on North Atlantic Climate. J Clim 31:8861–8873. https://doi.org/10.1175/JCLI-D-18-0097.1

Back LE, Bretherton CS (2009) On the relationship between SST gradients, boundary layer winds, and convergence over the tropical oceans. J Clim 22:4182–4196. https://doi.org/10.1175/2009JCLI2392.1

Bell CJ, Gray LJ, Charlton-Perez AJ, Joshi MM, Scaife AA (2009) Stratospheric communication of El Niño teleconnections to European winter. J Clim 22:4083–4096. https://doi.org/10.1175/2009JCLI2717.1

Blackmon ML (1976) A climatological spectral study of the 500 mb geopotential height of the Northern hemisphere. J Atmos Sci 33:1607–1623. https://doi.org/10.1175/1520-0469(1976)033<1607:ACSSOT>2.0.CO;2

Bladé I, Newman M, Alexander MA, Scott JD (2008) The late fall extratropical response to ENSO: sensitivity to coupling and convection in the Tropical West Pacific. J Clim 21:6101–6118. https://doi.org/10.1175/2008JCLI1612.1

Branstator G (2002) Circumglobal teleconnections, the jet stream waveguide, and the North Atlantic Oscillation. J Clim 15:1893–1910. https://doi.org/10.1175/15200442(2002)015,1893:CTTJSW.2.0.CO;2

Brönnimann S (2007) Impact of El Niño–Southern Oscillation on European climate. Rev Geophys 45:RG3003. https://doi.org/10.1029/2006RG000199

Burgers G, Stephenson DB (1999) The "normality" of el niño. Geophys Res Lett 26(8):1027–1030. https://doi.org/10.1029/1999GL900161

Butler AH, Polvani LM, Deser C (2014) Separating the stratospheric and tropospheric pathways of El Niño-Southern Oscillation teleconnections. Environ Res Lett 9:024014. https://doi.org/10.1088/1748-9326/9/2/024014

Cagnazzo C, Manzini E (2009) Impact of the stratosphere on the winter tropospheric teleconnections between ENSO and the North Atlantic and European Region. J Clim 22:1223–1238. https://doi.org/10.1175/2008JCLI2549.1

Capotondi A, Wittenberg AT, Newman M, Di Lorenzo E, Yu J-Y et al (2015) Understanding ENSO diversity. Bull Am Meteorol Soc 96:921–938. https://doi.org/10.1175/BAMS-D-13-00117.1

Chang EK, Fu Y (2002) Interdecadal variations in Northern Hemisphere winter storm track intensity. J Clim 15:642–658. https://doi.org/10.1175/1520-0442(2002)015,0642:IVINHW.2.0.CO;2

Davini P, von Hardenberg J, Corti S, Christensen HM, Juricke S et al (2017) Climate SPHINX: evaluating the impact of resolution and stochastic physics parameterisations in the EC-Earth global climate model. Geosci Model Dev 10:1383–1402. https://doi.org/10.5194/gmd-10-1383-2017

Deser C, Simpson IR, McKinnon KA, Phillips AS (2017) The Northern hemisphere extratropical atmospheric circulation response to

ENSO: how well do we know it and how do we evaluate models accordingly? J Clim 30:5059–5082. https://doi.org/10.1175/JCLI-D-16-0844.1
DeWeaver E, Nigam S (2002) Linearity in ENSO's atmospheric response. J Clim 15:2446–2461. https://doi.org/10.1175/1520-0442(2002)015,2446:LIESAR.2.0.CO;2
Domeisen DI, Garfinkel CI, Butler AH (2019) The teleconnection of El Niño Southern Oscillation to the stratosphere. Rev Geophys 57:5–47. https://doi.org/10.1029/2018RG000596
García-Serrano J, Cassou C, Douville H, Giannini A, Doblas-Reyes FJ (2017) Revisiting the ENSO teleconnection to the tropical North Atlantic. J Clim 30:6945–6957. https://doi.org/10.1175/JCLI-D-16-0641.1
García-Serrano J, Rodríguez-Fonseca B, Bladé I, Zurita-Gotor P, de la Cámara A (2011) Rotational atmospheric circulation during North Atlantic-European winter: the influence of ENSO. Clim Dyn 37:1727–1743. https://doi.org/10.1007/s00382-010-0968-y
Garfinkel CI, Weinberger I, White IP, Oman LD, Aquila V et al (2019) The salience of nonlinearities in the boreal winter response to ENSO: North Pacific and North America. Clim Dyn 52:4429–4446. https://doi.org/10.1007/s00382-018-4386-x
Gill AE (1980) Some simple solutions for heat-induced tropical circulation. Q J R Meteorol Soc 106:447–462. https://doi.org/10.1002/qj.49710644905
Graham NE, Barnett TP (1987) Sea surface temperature, surface wind divergence, and convection over tropical oceans. Science 238:657–659. https://doi.org/10.1126/science.238.4827.657
Gouirand I, Moron V, Zorita E (2007) Teleconnections between ENSO and North Atlantic in an ECHO-G simulation of the 1000–1990. Geophys Res Lett 34:L06705. doi:https://doi.org/10.1029/2006GL028852
Haarsma RJ, Acosta M, Bakhshi R, Bretonnière P-A, Caron L-P et al (2020) HighResMIP versions of EC-EARTH: EC-Earth3P and EC-Earth3P-HR. Description, model computational performance and basic validation. Geosci Model Dev. https://doi.org/10.5194/gmd-2019-350
Hardiman SC, Dunstone NJ, Scaife AA, Smith DM, Ineson S et al (2019) The impact of strong El Niño and La Niña events on the North Atlantic. Geophys Res Lett 46:2874–2883. https://doi.org/10.1029/2018GL081776
Held IM, Ting M, Wang H (2002) Northern winter stationary waves: theory and modeling. J Clim 15:2125–2144. https://doi.org/10.1175/1520-0442(2002)015<2125:NWSWTA>2.0.CO;2
Hitchcock P, Simpson IR (2014) The downward influence of stratospheric sudden warmings. J Atmos Sci 71:3856–3876. https://doi.org/10.1175/JAS-D-14-0012.1
Hoerling MP, Kumar A, Xu T (2001) Robustness of the nonlinear climate response to ENSO's extreme phases. J Clim 14:1277–1293. https://doi.org/10.1175/1520-0442(2001)014<1277:ROTNCR>2.0.CO;2
Hoerling MP, Kumar A, Zhong M (1997) El Niño, La Niña, and the nonlinearity of their teleconnections. J Clim 10:1769–1786. https://doi.org/10.1175/1520-0442(1997)010<1769:ENOLNA>2.0.CO;2
Horel JD, Wallace JM (1981) Planetary-scale atmospheric phenomena associated with the Southern oscillation. Mon Weather Rev 109:813–829. https://doi.org/10.1175/1520-0493(1981)109<0813:PSAPAW>2.0.CO;2
Hoskins BJ, James LN, White GH (1983) The shape, propagation and mean-flow interaction of large-scale weather systems. J Atmos Sci 40:1595–1612. https://doi.org/10.1175/1520-0469(1983)040<595:TSPAMF>2.0.CO;2
Hoskins BJ, Karoly DJ (1981) The steady linear response of a spherical atmosphere to thermal and orographic forcing. J Atmos Sci 38:1179–1196. https://doi.org/10.1175/1520-0469(1981)038<1179:TSLROA>2.0.CO;2
Ineson S, Scaife AA (2009) The role of the stratosphere in the European climate response to El Niño. Nat Geosci 2:32–36. https://doi.org/10.1038/ngeo381
Jiménez-Esteve B, Domeisen DI (2018) The Tropospheric Pathway of the ENSO–North Atlantic Teleconnection. Geophys Res Lett 46:4563–4584. https://doi.org/10.1175/JCLI-D-17-0716.1
Jiménez-Esteve B, Domeisen DI (2019) Nonlinearity in the North Pacific atmospheric response to a linear ENSO forcing. Geophys Res Lett 46:2271–2281. https://doi.org/10.1029/2018GL081226
Jin F, Hoskins BJ (1995) The direct response to tropical heating in a baroclinic atmosphere. J Atmos Sci 52:307–319. https://doi.org/10.1175/1520-0469(1995)052<0307:TDRTTH>2.0.CO;2
Kidston J, Scaife AA, Hardiman SC, Mitchell DM, Butchart N et al (2015) Stratospheric influence on tropospheric jet streams, storm tracks and surface weather. Nat Geosci 8:433–440. https://doi.org/10.1038/ngeo2424
King MP, Herceg-Bulić I, Bladé I, García-Serrano J, Keenlyside N et al (2018) Importance of late fall ENSO teleconnection in the Euro-Atlantic sector. Bull Am Meteorol Soc 99:1337–1343. https://doi.org/10.1175/BAMS-D-17-0020.1
Lee S, Wang C, Mapes BE (2009) A simple atmospheric model of the local and teleconnection responses to tropical heating anomalies. J Clim 22:272–284. https://doi.org/10.1175/2008JCLI2303.1
Lau N-C (1988) Variability of the observed midlatitude storm tracks in relation to low-frequency changes in the circulation pattern. J Atmos Sci 45:2718–2743. https://doi.org/10.1175/1520-0469(1988)045<2718:VOTOMS>2.0.CO;2
Lindzen RS, Nigam S (1987) On the role of sea surface temperature gradients in forcing low-level winds and convergence in the tropics. J Atmos Sci 44:2418–2436. https://doi.org/10.1175/1520-0469(1987)044<2418:OTROSS>2.0.CO;2
Matsuno T (1966) Quasi-geostrophic motions in the equatorial area. J Meteorol Soc Jpn 44:25–43. https://doi.org/10.2151/jmsj1965.44.1_25
Mezzina B, García-Serrano J, Bladé I, Kucharski F (2020) Dynamics of the ENSO teleconnection and NAO variability in the North Atlantic–European late winter. J Clim 33:907–923. https://doi.org/10.1175/JCLI-D-19-0192.1
Moron V, Gouirand I (2003) Seasonal modulation of the El Niño–Southern Oscillation relationship with sea level pressure anomalies over the North Atlantic in October–March (1873–1996). Int J Climatol 23:143–155. https://doi.org/10.1002/joc.868
Numaguti A, Hayashi Y-Y (1991) Behavior of cumulus activity and the structures of circulations in an "Aqua Planet" model. J Meteorol Soc Jpn 69:563–579. https://doi.org/10.2151/jmsj1965.69.5_563
Poli P, Hersbach H, Dee DP, Berrisford P, Simmons AJ et al (2016) ERA-20C: an atmospheric reanalysis of the twentieth century. J Clim 29:4083–4097. https://doi.org/10.1175/JCLI-D-15-0556.1
Pozo-Vázquez D, Esteban-Parra MJ, Rodrigo FS, Castro-Díez Y (2001) The association between ENSO and winter atmospheric circulation and temperature in the North Atlantic Region. J Clim 14:3408–3420. https://doi.org/10.1175/1520-0442(2001)014<3408:TABEAW>2.0.CO;2
Qin J, Robinson WA (1993) On the Rossby wave source and the steady linear response to tropical forcing. J Atmos Sci 50:1819–1823. https://doi.org/10.1175/1520-0469(1993)050<1819:OTRWSA>2.0.CO;2
Rao J, Ren R (2016a) Asymmetry and nonlinearity of the influence of ENSO on the northern winter stratosphere: 1. Observations. J Geophys Res Atmos 121:9000–9016. doi:https://doi.org/10.1002/2015JD024520
Rao J, Ren R (2016b) Asymmetry and nonlinearity of the influence of ENSO on the northern winter stratosphere: 2. Model study with

WACCM. J Geophys Res Atmos 121:9017–9032. doi:https://doi.org/10.1002/2015JD024521
Roehrig R, Beau I, Saint-Martin D, Alias A, Decharme B et al (2020) The CNRM global atmosphere model ARPEGE-Climat 6.3: description and evaluation. J Adv Model Earth Syst
Sanna A, Borrelli A, Athanasiadis P, Materia S, Storto A et al (2017) CMCC-SPS3: the CMCC seasonal prediction system 3. CMCC Tech Rep RP0285:61
Sardeshmukh PD, Compo GP, Penland C (2000) Changes of probability associated with El Niño. J. Clim 13:4268-4286. https://doi.org/10.1175/1520-0442(2000)013<4268:COPAWE>2.0.CO;2
Sardeshmukh PD, Hoskins BJ (1987) On the derivation of the divergent flow from the rotational flow: the χ problem. Q J R Meteorol Soc 113:339–360. https://doi.org/10.1002/qj.49711347519
Sardeshmukh PD, Hoskins BJ (1988) The generation of global rotational flow by steady idealized tropical divergence. J Atmos Sci 45:1228–1251. https://doi.org/10.1175/1520-0469(1988)045<1228:TGOGRF>2.0.CO;2
Taguchi M, Hartmann DL (2006) Increased occurrence of stratospheric sudden warmings during El Niño as simulated by WACCM. J Clim 19:324–332. https://doi.org/10.1175/JCLI3655.1
Timmermann A, An S, Kug J, Jin F-F, Cai W et al (2018) (2018) El Niño-Southern Oscillation complexity. Nature 559:535–545. https://doi.org/10.1038/s41586-018-0252-6
Ting M (1996) Steady linear response to tropical heating in barotropic and baroclinic models. J Atmos Sci 53:1698–1709. https://doi.org/10.1175/1520-0469(1996)053<1698:SLRTTH>2.0.CO;2
Titchner HA, Rayner NA (2014) The Met Office Hadley Centre sea ice and sea surface temperature data set, version 2: 1. Sea ice concentrations. J Geophys Res Atmos 119:2864–2889. https://doi.org/10.1002/2013JD020316
Toniazzo T, Scaife AA (2006) The influence of ENSO on winter North Atlantic climate. Geophys Res Lett 33:L24704. doi:https://doi.org/10.1029/2006GL027881
Trascasa-Castro P, Maycock AC, Scott Yiu YY, Fletcher JK (2019) On the linearity of the stratospheric and Euro-Atlantic sector response to ENSO. J Clim 32:6607–6626. https://doi.org/10.1175/JCLI-D-18-0746.1
Trenberth KE (1986) An assessment of the impact of transient eddies on the zonal flow during a blocking episode using localized Eliassen-Palm flux diagnostics. J Atmos Sci 43:2070–2087. https://doi.org/10.1175/1520-0469(1986)043<2070:AAOTIO>2.0.CO;2
Trenberth KE, Branstator GW, Karoly D, Kumar A, Lau N-C, Ropelewski C (1998) Progress during TOGA in understanding and modeling global teleconnections associated with tropical sea surface temperatures. J Geophys Res 103(C7):14291–14324. https://doi.org/10.1029/97JC01444
Voldoire A, Saint-Martin D, Sénési S, Decharme B, Alias A et al (2019) Evaluation of CMIP6 DECK experiments with CNRM-CM6-1. J Adv Model Earth Syst 11:2177–2213. https://doi.org/10.1029/2019MS001683
Wallace JM, Lim G, Blackmon ML (1988) Relationship between cyclone tracks, anticyclone tracks and baroclinic waveguides. J Atmos Sci 45:439–462. https://doi.org/10.1175/1520-0469(1988)045<0439:RBCTAT>2.0.CO;2
Wang C (2005) ENSO, Atlantic climate variability and the Walker and Hadley circulations. In: Diaz HF, Bradley RS (eds) The Hadley Circulation: present, past and future. Kluwer Academic Publishers, The Netherlands, pp 173–202
Weinberger I, Garfinkel CI, White IP, Oman LD (2019) The salience of nonlinearities in the boreal winter response to ENSO: Arctic stratosphere and Europe. Clim Dyn 53:4591–4610. https://doi.org/10.1007/s00382-019-04805-1
Zhang W, Wang Z, Stuecker MF, Turner AG, Jin F-F et al (2019) Impact of ENSO longitudinal position on teleconnections to the NAO. Clim Dyn 52:257–274. https://doi.org/10.1007/s00382-018-4135-1

3.1 Supplementary Material

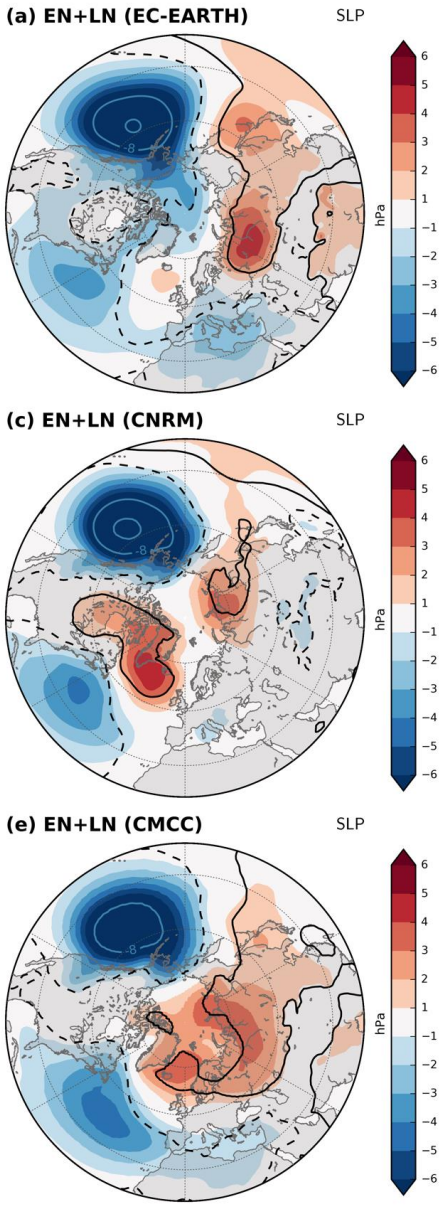

Online Resource 1. EN+LN ensemble-mean SLP anomalies in JFM: EC-EARTH (top), CNRM (middle), CMCC (bottom). Blue contours show values exceeding the color scale limit at -8, -12,-16 hPa. Black contours indicate statistically significant areas at the 95% confidence level

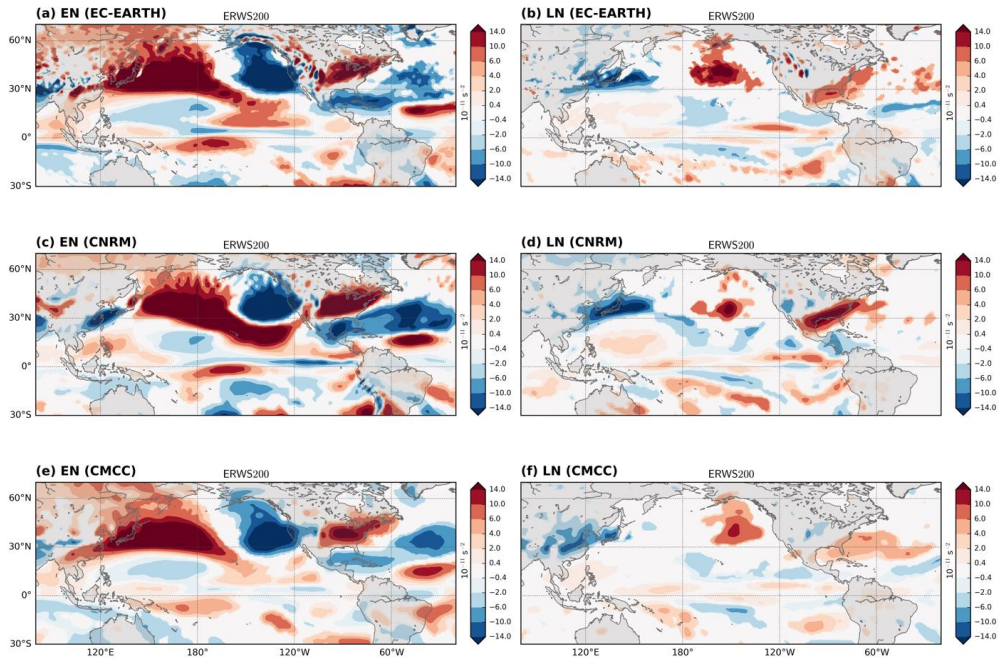

Online Resource 2. Ensemble-mean 200-hPa ERWS anomalies for (left) EN and (right) LN with respect to CTL in JFM: EC-EARTH (top), CNRM (middle), CMCC (bottom). Only statistically significant anomalies (95% confidence level) are shown. Anomalies are smoothed in CMCC for clarity

Chapter 4

Multi-model assessment of the late-winter stratospheric response to El Niño and La Niña

This chapter contains the research article Mezzina et al. 2021b and addresses objectives 1 and 4 from Sect. 1.3.

Mezzina, B., Palmeiro, F. M., García-Serrano, J., Bladé, I., Batté, L., & Benassi, M. (2021b). Multi-model assessment of the late-winter stratospheric response to El Niño and La Niña. *Clim. Dyn.*, 1–21. https://doi.org/10.1007/s00382-021-05836-3

Climate Dynamics
https://doi.org/10.1007/s00382-021-05836-3

Multi-model assessment of the late-winter stratospheric response to El Niño and La Niña

Bianca Mezzina[1] · Froila M. Palmeiro[2] · Javier García-Serrano[1,2] · Ileana Bladé[2] · Lauriane Batté[3] · Marianna Benassi[4]

Received: 10 December 2020 / Accepted: 3 June 2021

Abstract
The impact of El Niño-Southern Oscillation (ENSO) on the late-winter extra-tropical stratosphere (January–March) is assessed in a multi-model framework. Three state-of-the-art atmospheric models are run with prescribed SST anomalies representative of a strong ENSO event, with symmetric patterns for El Niño and La Niña. The well-known temperature perturbation in the lower stratosphere during El Niño is captured by two models, in which the anomalous warming at polar latitudes is accompanied by a positive geopotential height anomaly that extends over the polar cap. In the third model, which shows a lack of temperature anomalies over the pole, the anomalous anticyclone is confined over Canada and does not expand to the polar cap. This anomalous center of action emerges from the large-scale tropospheric Rossby wave train forced by ENSO, and shrinking/stretching around the polar vortex is invoked to link it to the temperature response. No disagreement across models is found in the lower stratosphere for La Niña, whose teleconnection is opposite in sign but weaker. In the middle-upper stratosphere (above 50 hPa) the geopotential height anomalies project on a wavenumber-1 (WN1) pattern for both El Niño and, more weakly, La Niña, and show a westward tilt with height up to the stratopause. It is suggested that this WN1 pattern arises from the high-latitude lower-stratospheric anomalies, and that the ENSO teleconnection to the polar stratosphere can be interpreted in terms of upward propagation of the stationary Rossby wave train and quasi-geostrophic balance, instead of wave breaking.

Keywords ENSO · Atmospheric teleconnections · Climate modeling · Stratosphere

1 Introduction

When referring to El Niño-Southern Oscillation (ENSO), the term "stratospheric pathway" is now commonly used to allude to its extra-tropical teleconnection (e.g. Butler et al. 2014). With this expression, it is implied that not only is ENSO inducing a response in the stratosphere, but also that this response is later transferred to the surface. Concerning the first part of the pathway, namely how the stratosphere is affected by ENSO, El Niño has been shown to have a robust impact on the winter seasonal-mean state of the Northern Hemisphere polar stratosphere, consisting of a warming at low levels and a weakening of the westerly flow related to the polar vortex (e.g. Taguchi and Hartmann 2006; Free and Seidel 2009; Calvo et al. 2010; see Domeisen et al. 2019 for a review). More recently, La Niña has been associated with the opposite response, a lower-stratospheric cooling and a strengthening of the westerly flow linked to the polar vortex (e.g. Calvo et al. 2010; Hurwitz et al. 2014; Iza et al.

This paper is a contribution tothe MEDSCOPE special issue on the drivers of variability andsources of predictability for the European and Mediterranean regionsat subseasonal to multi-annual time scales. MEDSCOPE is anERA4CS project co-funded by JPI Climate. The special issue wascoordinated by Silvio Gualdi and Lauriane Batté.

✉ Bianca Mezzina
bianca.mezzina@bsc.es

[1] Barcelona Supercomputing Center (BSC), Barcelona, Spain

[2] Group of Meteorology, Universitat de Barcelona (UB), Barcelona, Spain

[3] CNRM, Université de Toulouse, Météo-France, CNRS, Toulouse, France

[4] Fondazione Centro Euro-Mediterraneo sui Cambiamenti Climatici (CMCC), Bologna, Italy

Published online: 13 June 2021

2016; Weinberger et al. 2019), although there is still some controversy as to whether this atmospheric response is truly symmetric (e.g. Manzini et al. 2006; Hurwitz et al. 2014; Rao and Ren 2016a, b; Hardiman et al. 2019), where the skewness of the ENSO forcing may play a role. Addressing the (a)symmetry of the ENSO stratospheric response is one of the aims of the present model-based study, taking advantage of an experimental set-up with *symmetric* idealized SST forcing to represent El Niño and La Niña.

The mechanisms leading to the ENSO response in the polar stratosphere are also unsettled. The well-known tropospheric Rossby wave train excited by ENSO (Horel and Wallace 1981; Hoskins and Karoly 1981) has its first center of action over the North Pacific and a second one over Canada. Early studies suggested that during El Niño the stationary wave pattern is reinforced in the lower stratosphere by the center of action over Canada, which strengthens the climatological Aleutian High and vertically propagates to the mesosphere (e.g. van Loon and Labitzke 1987; Hamilton 1993a, b, 1995; Sassi et al. 2004; Manzini et al. 2006). In contrast, a more recent interpretation of the ENSO impact on the polar stratosphere relies on the first center of action, which strengthens and expands (weakens and contracts) the climatological Aleutian Low in the troposphere during El Niño (La Niña). Thus, for El Niño, linear constructive interference is suggested to take place between the perturbed Aleutian Low and the climatological stationary wave pattern, and the opposite for La Niña (e.g. Garfinkel and Hartmann 2008; Ineson and Scaife 2009). According to this view, during El Niño anomalous vertically-propagating planetary waves grow with height and eventually break, decelerating the polar vortex and warming the stratosphere (e.g. see Domeisen et al. 2019 for a review), while wave breaking inhibition is associated with a stronger vortex during La Niña (e.g. Iza et al. 2016). In this study, we examine the vertical structure of the ENSO-forced circulation anomalies and their interaction with the climatological state and provide evidence to support the key roles of the center of action over Canada and the stratospheric Aleutian High, as opposed to the tropospheric Aleutian Low. In addition, by combining this analysis with other diagnostics such as the Eliassen-Palm (EP) flux and its divergence, we revisit the paradigm of the stratospheric impact of ENSO through anomalous "irreversible" (see Waugh and Polvani 2010 for a review) wave breaking, with arguments based on large-scale dynamics, including quasi-geostrophy and thermal wind balance.

Historically, the hypothesis of the stratospheric pathway emerged in an effort to understand the elusive ENSO teleconnection to the North Atlantic-European (NAE) region (e.g. Brönnimann 2007). The idea is that, as suggested for other stratospheric perturbations (see Kidston et al. 2015 for a review), the stratospheric ENSO signal may propagate downwards and project onto a dipolar sea-level pressure (SLP) pattern over the North Atlantic. This would be in agreement with the observed late-winter (January–March) "canonical" response to ENSO in the NAE sector, which consists of a SLP dipole between mid and high latitudes (see Brönnimann 2007 for a review). Mezzina et al. (2021) have used the same multi-model ensemble employed in the present study to analyze the tropospheric pathway of the ENSO teleconnection and have concluded that this dipole (Fig. 1) is mostly driven by the forced, tropospheric large-scale Rossby wave train. By assessing the stratospheric response in the same set of sensitivity experiments, we complement their results and provide further evidence for the minor role of the stratosphere in the late-winter ENSO teleconnection to the NAE region.

Sudden stratospheric warmings (SSWs) are abrupt, nonlinear events that consist of a strong deceleration and warming of the polar vortex (Matsuno 1971), similar in sign to the El Niño effect, but with a different time-scale (daily-weekly). They have been suggested to play a key role in the stratospheric pathway of El Niño to the NAE region (e.g. Domeisen et al. 2015; Richter et al. 2015; Calvo et al. 2017; Bell et al. 2009; Ineson and Scaife 2009; Butler et al. 2014), or an amplifying role for the surface response (Cagnazzo and Manzini 2009). The relationship with the La Niña teleconnection is more obscure, and overall their implication during ENSO events is not clear, as other studies consider SSWs and ENSO as distinct sources of variability in the North Atlantic (e.g. Polvani et al. 2017; Oehrlein et al. 2019). Using the same set of sensitivity experiments as in the present study, Palmeiro et al. (2021a) have concluded that while ENSO modifies the seasonal-mean state of the polar vortex by conditioning it to be more (less) easily perturbed during El Niño (La Niña), the actual triggering of SSWs (at higher-frequency time-scales) is largely unrelated to ENSO. Based on their results, in this work only anomalies at the seasonal time-scale are considered, which implicitly include SSWs, but the occurrence of SSWs is not explicitly taken into account, also in agreement with their minimal contribution to the seasonal-mean state (Garfinkel et al. 2012).

This study explores the impact of ENSO on the polar stratosphere in late winter (JFM; January–March), following the approach of Mezzina et al. (2020, 2021) to avoid intra-seasonal issues between early and late winter in the canonical NAE response (e.g. Ayarzagüena et al. 2018; King et al. 2018), and also in recognition of the fact that the stratospheric response to El Niño is not well established until January (e.g. van Loon and Labitzke 1987; Manzini et al. 2006; Ineson and Scaife 2009). Several model-based studies have been published on this topic, but the fact that the same suite of sensitivity experiments is run using three state-of-the-art high-top models (i.e., with a well-resolved stratosphere) adds strength to this work. Furthermore, the experimental design, tailored to isolate the impacts of a

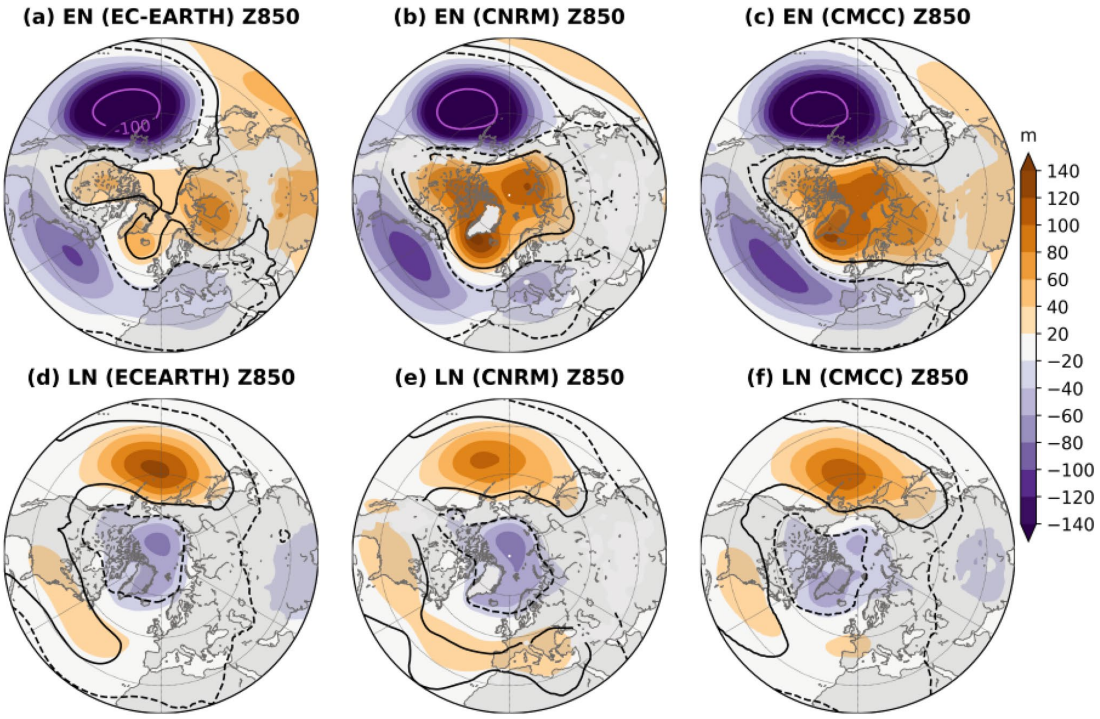

Fig. 1 Ensemble-mean geopotential height response at 850 hPa for EN (top) and LN (bottom) in JFM: EC-EARTH (left), CNRM (middle), CMCC (right). Magenta contours show values exceeding the color scale limit at − 100 m. Black contours (solid for positive, dashed for negative anomalies) indicate statistically significant areas at the 95% confidence level

symmetric, observation-based El Niño- and La Niña-like forcing, distinguishes our study from previous ones using coupled models (e.g. Calvo et al. 2017), global SST forcing (e.g. Weinberger et al. 2019) or idealized boundary conditions (e.g. Trascasa-Castro et al. 2019).

We will assess, in a multi-model approach, the (a)symmetry of the late-winter response to El Niño and La Niña in the lower (up to 50 hPa) and middle-upper (up to 1 hPa) stratosphere separately, to highlight the different features. Taking advantage of the different performances of the models, we will clarify what aspects of the ENSO response in the polar stratosphere appear to be robust and we will provide a consistent dynamical interpretation and/or implications for the impact on temperature and zonal wind.

After describing the experiments and methodology (Sect. 2), the models' climatology in the stratosphere is briefly analyzed (Sect. 3.1). Results on the SST-forced atmospheric circulation are presented in the rest of Sect. 3, first examining the zonal-mean response (Sects. 3.2–3.3), then focusing on the lower stratosphere (Sects. 3.4–3.5) and finally on the middle-upper stratosphere (Sect. 3.6). Additional remarks on the dynamical aspects of the temperature response are presented in Sect. 3.7. The main findings are summarized and discussed in Sect. 4.

2 Data and methods

2.1 Models and experimental set-up

This study makes use of a coordinated set of sensitivity atmosphere-only experiments performed with three different state-of-the-art atmospheric general circulation models (AGCMs) that contribute to the European ERA4CS-funded MEDSCOPE project. The experimental protocol, aimed to isolate the atmospheric response to El Niño (EN) and La Niña (LN), as compared to neutral conditions with prescribed climatological SST (CTL), has already been described in depth by Mezzina et al. (2021) and Benassi et al. (2021). Here, only a short summary is provided. Common to all simulations is: (i) the background SST climatology, computed from HadISST v2.2 (Titchner and Rayner 2014) over 1981–2010; (ii) fixed radiative forcings (GHG, solar, ozone, aerosols) at year 2000, representative of

present-day conditions; and, (iii) the ensemble size, consisting of 50 winters. The baseline experiment (CTL) was run for 50 years after spin-up, providing atmospheric initial conditions for the ENSO experiments. The anomalous boundary conditions were created by regressing detrended monthly SST anomalies onto the DJF Niño3.4 index to set an ENSO cycle from June (year 0) to May (year 1), restricted to the central-eastern tropical Pacific (e.g. as in Jiménez-Esteve and Domeisen 2019), and amplified to have a maximum anomaly of 2.7/2.4 °C in DJF/JFM (e.g. as in Taguchi and Hartmann 2006). The EN and LN SST forcings are symmetric and opposite in sign and can be considered as idealized strong eastern-Pacific events. Further details, including visualization of the SST patterns, can be found in Mezzina et al. (2021).

The AGCMs correspond to the atmospheric components of the following climate models (with lon × lat grid/vertical levels): EC-EARTH version 3.2, 512 × 256/L91 up to 0.01 hPa (Davini et al. 2017); CNRM Climate Model version 6–1, 256 × 128/L91 up to 0.01 hPa (Voldoire et al. 2019; Roehrig et al. 2020); CMCC Seasonal Prediction System 3, 360 × 180/L46 up to 0.3 hPa (Sanna et al. 2017). These three AGCMs are considered "high-top" models since they properly resolve the stratosphere, particularly the northern polar stratosphere. They also simulate QBO-like variability in the tropical stratosphere (e.g. see Palmeiro et al. 2020 for EC-EARTH), but the potential impact of the (internally-generated) QBO on the ENSO teleconnections has been minimized as all simulations start from the same atmospheric initial conditions from a continuous run, so that the different easterly/westerly QBO phases are equally sampled in the CTL and EN/LN experiments. More details on the AGCMs can be found in Mezzina et al. (2021).

2.2 Diagnostics and methods

In quasi-geostrophic (QG) theory, large-scale Rossby wave propagation and its interaction with the mean flow can be diagnosed by the Eliassen-Palm (EP) flux (e.g. Andrews et al. 1987; Vallis 2017):

$$F_y = -\rho a \cos\varphi \left[u^* v^*\right]$$

$$F_z = \rho a \cos\varphi \frac{Rf}{HN^2}\left[v^* T^*\right]$$

where ρ is the air density, a is the Earth radius, φ is latitude, R is the gas constant (287 $m^2 s^{-2} K^{-1}$), f is the Coriolis parameter or planetary vorticity, H is the scale-height (7 km), and N^2 is the squared Brunt-Väisälä buoyancy frequency. $[u^* v^*]$ is the eddy momentum flux and $[v^* T^*]$ the eddy heat flux, where * indicates perturbation from the zonal-mean and $[\,]$ denotes a zonal-mean. The divergence of the EP flux ($\nabla \cdot F$) appears in the momentum equation and encapsulates the eddy forcing of the mean flow, with EP flux divergence (convergence) implying acceleration (deceleration) of the zonal-mean zonal wind. These diagnostics are examined in Sect. 3.3. Details on the scaling of F_z and F_y are described in the caption of Fig. 4.

The QG potential vorticity can be defined as (e.g. Andrews et al. 1987; Vallis 2017):

$$q = \zeta + f + \frac{1}{\rho}\frac{\partial}{\partial z}\left(\rho \frac{f_0^2}{N^2}\frac{\partial \psi}{\partial z}\right)$$

where g is the gravity, f_0 is a suitable reference of the Coriolis parameter at some origin φ_0 (note that $\Phi = f_0 \psi$, with Φ the geopotential), ψ is the geostrophic streamfunction, and z is the vertical log-pressure coordinate. The first term is the geostrophic relative vorticity ($\zeta = \nabla^2 \psi$), the second represents the planetary vorticity ($f = 2\Omega \sin\varphi$), and the third term is the stretching vorticity. The potential vorticity is conserved following the (geostrophic) flow in the absence of frictional and diabatic effects. The vertical gradient of ψ (and its curvature, the second derivative) increases (decreases) where relative vorticity decreases or becomes more anticyclonic (increases or becomes more cyclonic). This can be more easily diagnosed by taking the (zonal-eddy) perturbation potential vorticity (e.g. Plumb 1985; Andrews et al. 1987):

$$q^* = \zeta^* + \frac{1}{\rho}\frac{\partial}{\partial z}\left(\rho \frac{f_0^2}{N^2}\frac{\partial \psi^*}{\partial z}\right)$$

Note that the two views presented above are dynamically equivalent. In fact, from the zonal-mean QG potential vorticity equation, the divergence of the EP flux can be expressed as (e.g. Andrews et al. 1987; Vallis 2017): $\rho^{-1}\nabla \cdot F = \left[v^* q^*\right]$; thereby, EP flux divergence (convergence) is associated with a poleward flux of positive (negative) potential vorticity.

Furthermore, in hydrostatic balance, changes in potential vorticity can be related to temperature variations via the hypsometric equation (e.g. Andrews et al. 1987):

$$T^* = \frac{Hf_0}{R}\frac{\partial \psi^*}{\partial z}$$

The link between potential vorticity and temperature might be more easily interpreted using isentropic coordinates and Ertel's formulation (e.g. Vallis 2017), but this is beyond the scope of the present study.

Ensemble-mean differences between the EN/LN experiments and the CTL simulation are computed to estimate the *forced* atmospheric response to ENSO. Statistical significance has been assessed with a Student's *t*-test for

difference of means at the 95% confidence level. Note that while monthly outputs were stored at several vertical levels from 850 to 1 hPa, for daily outputs only seven vertical levels in the stratosphere were available from the multi-model: 200, 100, 70, 50, 30, 20, 10 hPa. Observational composites based on reanalysis are shown and detailed in Appendix 1.

3 Results

3.1 Stratosphere climatology

Since the aim of the study is to investigate the impact of ENSO on the stratosphere, we first describe the models climatological geopotential height (Z) at various levels (Fig. 2). In the lower stratosphere (at 100 and 50 hPa, Fig. 2g–l), the low-pressure center corresponding to the polar vortex (shading) is slightly off-centered with respect to the pole and elongates towards Siberia and Canada, while it retracts over the North Pacific due to the presence of a large-scale anticyclone (the Rocky Mountain Ridge; Nigam and DeWeaver 2003) that appears clearly in the zonal-eddy field (Z^*, contours). In the middle-upper stratosphere (at 10 and 1 hPa) the vortex is much more zonally symmetric and stronger (Fig. 2a–f, shading), although still showing marked deviations from the pole. Here, the zonal-eddy field is dominated by an anticyclone, the Aleutian High, and a cyclone, representing a displacement of the vortex: together, they form a couplet that tilts westward with height, indicating upward propagation of stationary wave activity, into the mesosphere (Harvey and Hitchman 1996; Harvey et al. 2002). With increasing height, the westerly winds strengthen so that only the longest waves can propagate upwards (Charney-Drazin wave filtering; Charney and Drazin 1961). Hence at 10 and 1 hPa a predominantly wavenumber-1 (WN1) pattern is found in the Z^* field (Fig. 2a–f), while some WN2 component is present at 50 hPa (Fig. 2g–i) and additionally some WN3 component at 100 hPa (Fig. 2j–l). All models capture these climatological features well, although EC-EARTH systematically shows a weaker vortex, particularly at 50 and 10 hPa (Fig. 2, left column; see Fig. 3a, g), a known bias of this model (Palmeiro et al. 2021b).

3.2 Zonal-mean zonal wind and temperature

We begin the analysis of the ENSO impact on the stratosphere by examining the anomalous response of the zonal-mean zonal wind in the EN experiment (Fig. 3, top row). A negative anomaly north of 60°N is present in CNRM and CMCC, peaking in the middle stratosphere (~ 10 hPa) and extending from the lowermost stratosphere to beyond 1 hPa (although the statistical significance is model dependent; Fig. 3b,c), implying a deceleration of the polar vortex (Fig. 3b, c, green contours). In both models, this weakening of the westerly winds is accompanied by a warming of the lower stratosphere north of 70°N (Fig. 3e,f), peaking at approximately 100 hPa and extending from just above the tropopause (green contour) to ~10 hPa, consistent with thermal wind balance. Both the weakening of the vortex, in the middle-upper stratosphere, and the warming of the polar cap, in the lower stratosphere, are well-documented aspects of the El Niño teleconnection to the stratosphere and also appear in our observational composites (Fig. 11a, c in Appendix 1). A different response, however, is found in the third model, EC-EARTH, which fails to capture the expected changes in the stratospheric polar cap (Fig. 3a, d). Note that, in contrast, in the troposphere, a southward shift in the mid-latitude jet is observed in all models (Fig. 3, top).

Interestingly, EC-EARTH does not show the same wrong performance for LN: all three models show a robust increase in the zonal-mean zonal wind at subpolar latitudes maximizing at around 10 hPa, as well as a cooling over the lower stratospheric polar cap (Fig. 3, third and fourth rows), again consistent with thermal wind balance. In CMCC, the response in EN is about 50% stronger than in LN, which is also less significant (cf. Fig. 3c, f, i, and l); on the contrary, in CNRM, the magnitude of the anomalies appears comparable or even stronger in LN (cf. Fig. 3b, e, h, and k), but, as we will discuss later in Sect. 3.6, this is a consequence of the zonal average. This almost linear response for LN was not necessarily expected—although also found in other models (e.g. Calvo et al. 2010; Hurwitz et al. 2014; Trascasa-Castro et al. 2019; Weinberger et al. 2019)—given that the observed La Niña signal is weak and not significant in our composites (Fig. 11e, g) or other observational studies (e.g. Manzini et al. 2006).

Note also that EC-EARTH simulates a weaker, southward shifted polar vortex compared to CNRM and CMCC (Fig. 3, green contours). This difference in the mean flow may have some impacts, but it is unlikely a relevant factor for the discordant EN signal in EC-EARTH, given that the same behavior is not observed for LN. This peculiarity of the ENSO response in EC-EARTH and the comparison with the other two models offers a unique opportunity to clarify the key mechanisms of the ENSO teleconnection to the stratosphere.

3.3 Eliassen-Palm flux and divergence

Changes in the upward propagation and breaking of planetary waves is commonly considered as the main factor driving the ENSO impact on the polar stratosphere. Failure in capturing this anomalous wave-mean flow interaction may be responsible for the unrealistic response in the zonal-mean zonal wind and temperature in EC-EARTH for

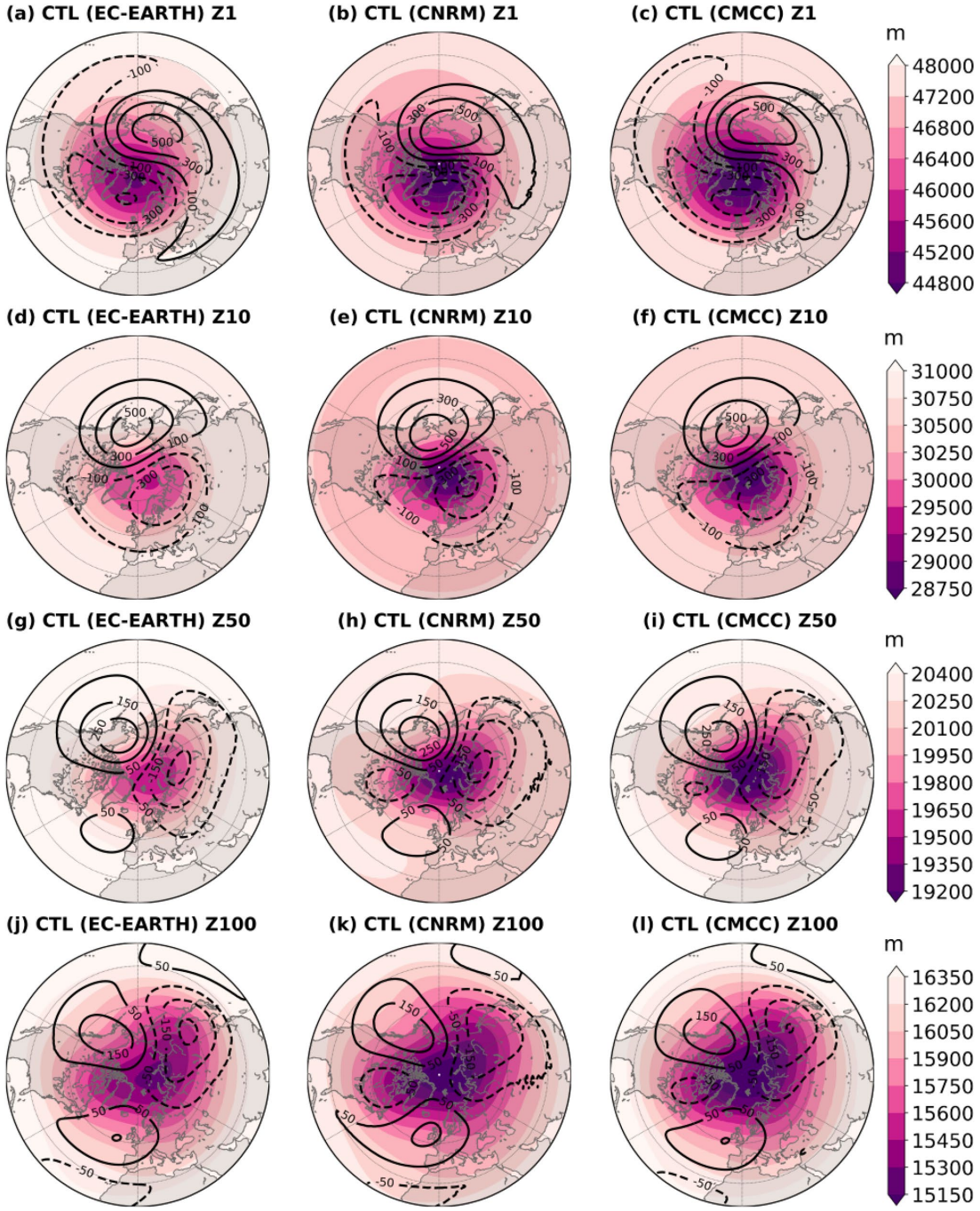

Fig. 2 JFM climatology of geopotential height (shading) and zonal-eddy geopotential height (contours) from CTL at 1 hPa (first row), 10 hPa (second row), 50 hPa (third row) and 100 hPa (fourth row): EC-EARTH (left), CNRM (middle), CMCC (right). Contour interval: $\pm 100, \pm 300, \pm 500$ in the first two rows; $\pm 50, \pm 150, \pm 250$ in the two bottom rows

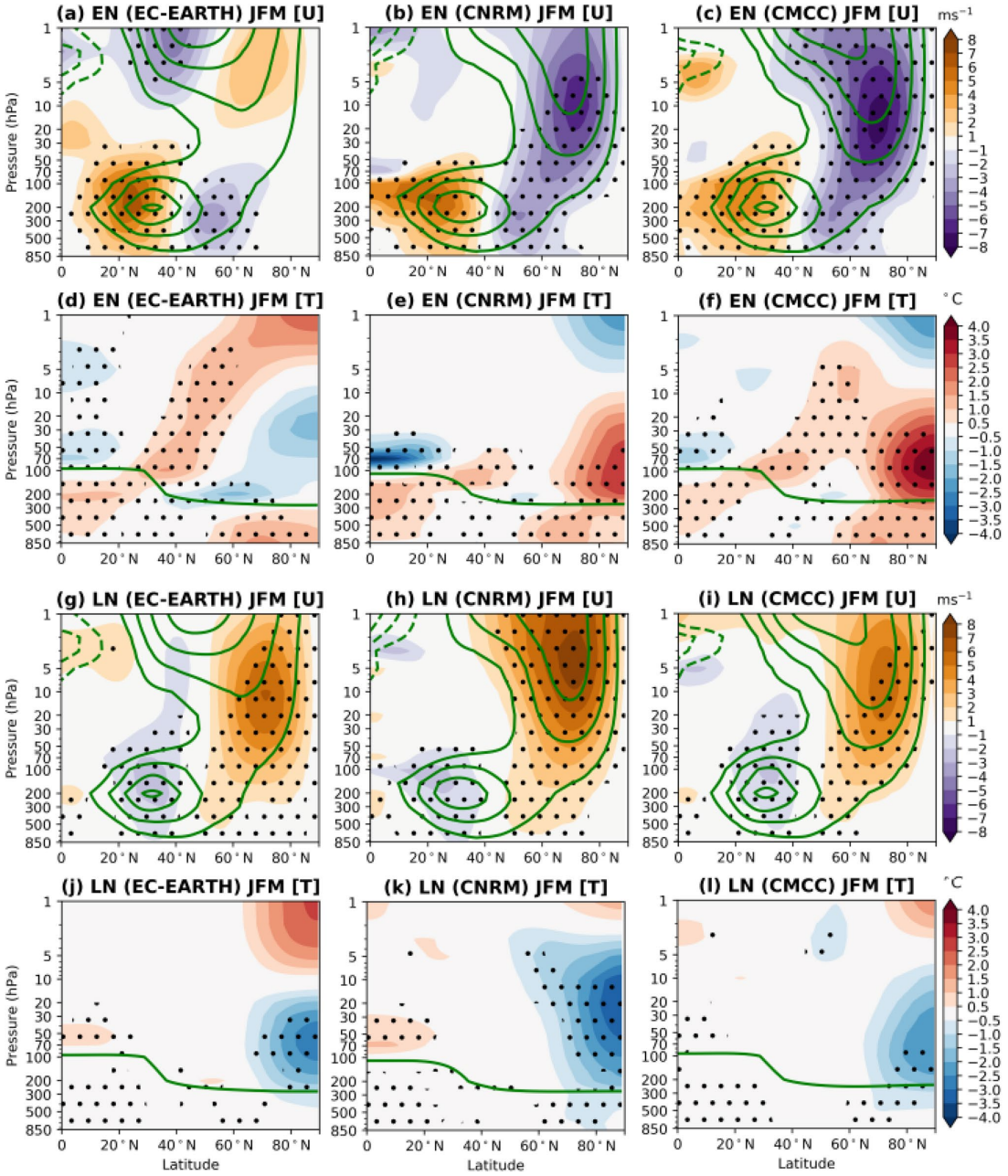

Fig. 3 **a**–**f** Ensemble-mean zonal-mean zonal wind (top row) and temperature (second row) anomalies for EN with respect to CTL in JFM: EC-EARTH (left), CNRM (middle), CMCC (right). **g**–**l** Same as (**a**–**f**), but for LN. Green contours in the zonal wind panels show its climatology from CTL (contour interval: 10 ms^{-1}) and the green line in the temperature panels depicts the tropopause level from CTL, according to the WMO's definition (lowest level at which the lapse rate decreases to 2 °C/km or less). Dotted areas indicate statistical significance at the 95% confidence level

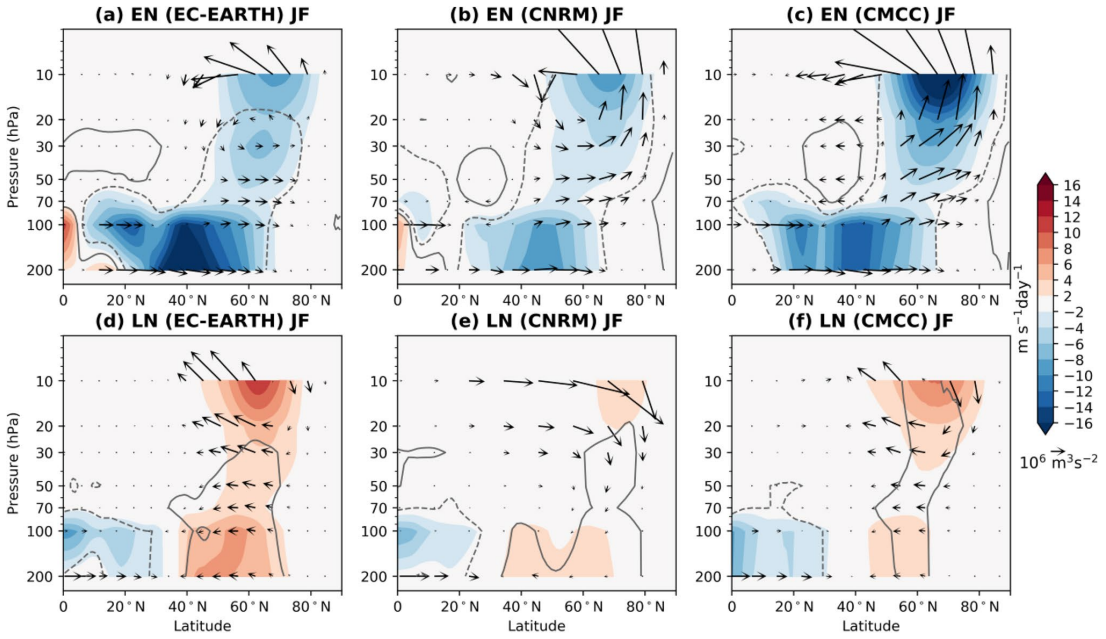

Fig. 4 Top: EP flux (arrows) and EP-flux divergence (shading) anomalies for EN with respect to CTL in JF: EC-EARTH (left), CNRM (middle), CMCC (right). Bottom: same as Top, but for LN. The EP flux is shown as $F/\rho a$ and scaled by $\sqrt{1000/p}$ as in Taguchi and Hartmann (2006); to improve visibility, F_z is multiplied by 100, as in Rao and Ren (2016a). Black contours (solid for positive, dashed for negative anomalies) indicate statistical significance at the 95% confidence level for the EP-flux divergence

EN. To explore this possibility, we examine the anomalous EP flux and its divergence (Fig. 4; see Sect. 2.2). Although the wave driving of the stratospheric circulation might be almost instantaneous (e.g. Shaw et al. 2014), we only consider JF, as in previous studies, as that is when the ENSO-related anomalous wave injection is expected to peak (e.g. García-Herrera et al. 2006; Bell et al. 2009). We begin by analyzing the divergence of the EP flux, $\nabla \cdot F$ (Fig. 4, shading), recalling that negative (positive) anomalies indicate divergence (convergence) of zonal momentum (u^*v^*) and deceleration (acceleration) of the flow. For EN (Fig. 4, top), a dominant negative $\nabla \cdot F$ anomaly is present in all cases throughout the atmosphere, in agreement with previous studies (e.g. Taguchi and Hartmann 2006; Trascasa-Castro et al. 2019), but with differences in magnitude and significance. In particular, all models show maximum EP-flux convergence in mid-latitudes at lower levels (below 70 hPa), consistent with the weakening of the tropospheric jet at its poleward flank (Fig. 3, top), observed even in EC-EARTH (Fig. 3a). Another negative maximum is present at higher latitudes in the upper levels (~ 10 hPa), which is consistent with the middle stratospheric anomalies in zonal-mean zonal wind in CMCC and CNRM (Fig. 3b, c) but inconsistent with the (lack of) signal in EC-EARTH (Fig. 3a). This inconsistency suggests that anomalous wave breaking may *not* actually drive the weakening of the polar vortex in these models. This hypothesis is further supported by the anomalous EP flux divergence in LN (Fig. 4g–i), which is qualitatively symmetric to that in EN, in agreement with previous studies (e.g. Iza et al. 2016; Trascasa-Castro et al. 2019), but much weaker and less significant, particularly in CNRM (Fig. 4e) even though that is the model with the largest strengthening of the polar vortex (Fig. 3h).

The vertical component of the EP flux (F_z), which is proportional to $[v^*T^*]$, is related to the vertical propagation of wave activity, and thus upward (downward) pointing vectors suggest enhanced (reduced) wave propagation towards higher levels. In EN, all models show EP-flux vectors pointing poleward in the lower stratosphere (up to 50 hPa; recall that F_y is proportional to $-[u^*v^*]$), and again behave similarly at 10 hPa, where they tend to turn equatorward (Fig. 3a–c). Between 50 and 10 hPa, the EP-flux vectors in CNRM and CMCC turn upwards at high latitudes (north of 60°–70° N), while the vertical component of the EP flux seems negligible in EC-EARTH, a difference that we will further discuss in Sect. 3.6. In LN, the EP-flux vectors do not clearly indicate a suppression of wave

propagation, except in the upper levels and at high latitudes (Fig. 4, bottom).

3.4 Longitude-latitude structure of temperature anomalies in the lower stratosphere

While zonal-mean profiles are a common approach to examine the vertical structure of the ENSO anomalies, looking at the spatial distribution of the signal in the longitude-latitude plane at some key levels is convenient to gain further insight into the models' response (e.g. Baldwin and O'Sullivan 1995; Sassi et al. 2004; Manzini et al. 2006; Garfinkel and Hartmann 2007; Cagnazzo and Manzini 2009). Due to the wave filtering exerted by strong westerly winds, different anomalous patterns are expected in the lower and middle-upper stratosphere, similarly to what is seen in the climatology (see Sect. 3.2): for this reason, here we show maps of anomalous temperature at 200, 100 and 50 hPa (Figs. 5 and 6), while the response above 50 hPa is discussed in Sect. 3.6. Note that in mid-latitudes and further north, the 200 hPa level is located above the tropopause (see green contour in Fig. 3). For EN, the lowermost stratosphere shows

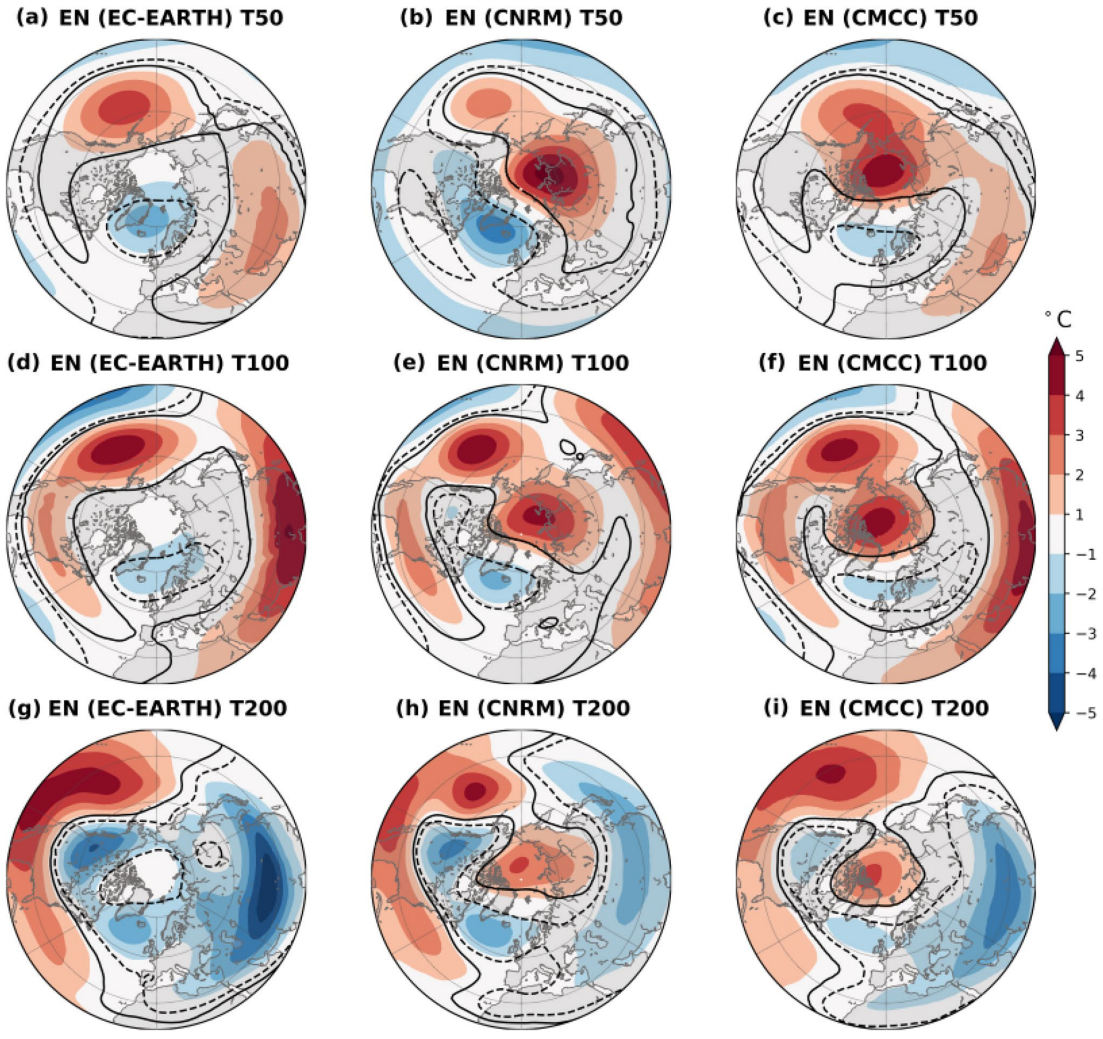

Fig. 5 Ensemble-mean temperature anomalies for EN with respect to CTL in JFM at 50 (top), 100 (middle) and 200 hPa (bottom): EC-EARTH (left), CNRM (middle), CMCC (right). Black contours (solid for positive, dashed for negative anomalies) indicate statistically significant areas at the 95% confidence level

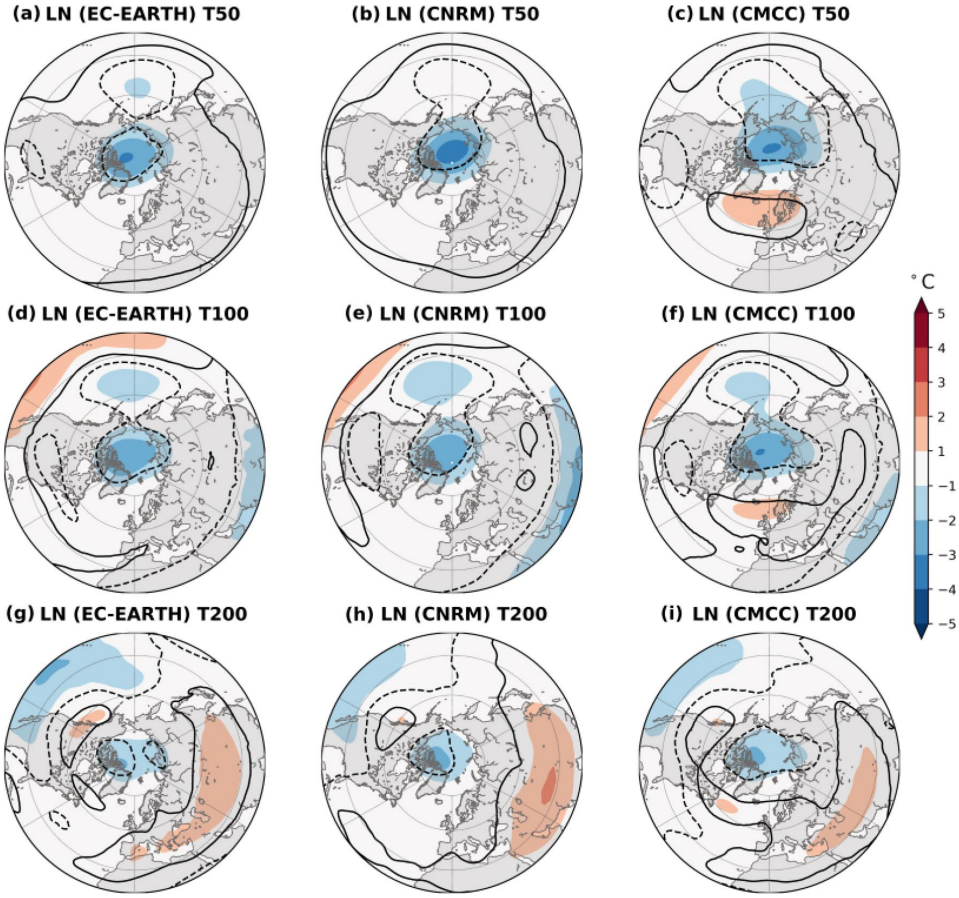

Fig. 6 Ensemble-mean temperature anomalies for LN with respect to CTL in JFM at 50 (top), 100 (middle) and 200 hPa (bottom): EC-EARTH (left), CNRM (middle), CMCC (right). Black contours (solid for positive, dashed for negative anomalies) indicate statistically significant areas at the 95% confidence level

a cooling at subpolar latitudes over North America and the North Atlantic (Fig. 5g–i). The peak in the warming of the polar cap in a zonal-mean sense is found around 100 hPa (Fig. 3b, c), but a positive temperature anomaly over polar latitudes is already present at 200 hPa in CMCC and CNRM, albeit displaced towards the North Pacific sector (Fig. 5h, i). While the subpolar cooling is also present in EC-EARTH, the warming over the polar cap is strikingly absent (Fig. 5g), indicating that this model is not simulating a displaced or weaker response masked by the zonal mean but is not yielding a response over the polar cap at all. The same situation is seen at higher levels, where CNRM and CMCC show an even stronger polar warming (Fig. 5b, c, e, and f), while EC-EARTH lacks any significant signal in that region (Fig. 5a, d). Note that, in contrast, no discrepancy is found between the models in the troposphere (Fig. S1). For LN (Fig. 6), instead, and as with the zonal mean (Fig. 3, bottom row), the temperature response is similar across the models, with the main feature being the cooling over the polar cap between 200 and 50 hPa, which, as in the case of EN, is located in the North Pacific sector (Fig. 5d–i). The temperature anomalies are weaker than in EN (by ~ 25% for the polar anomaly) but significant, even in EC-EARTH. In the observational composites, the polar cap anomalies appear more zonally symmetric (Fig. 11d), but the statistical significance for La Niña is limited to the North Pacific sector (Fig. 11h).

3.5 Longitude-latitude structure of geopotential height anomalies in the lower stratosphere

To gain further insight into the lower stratospheric response, we now examine maps of anomalous geopotential height

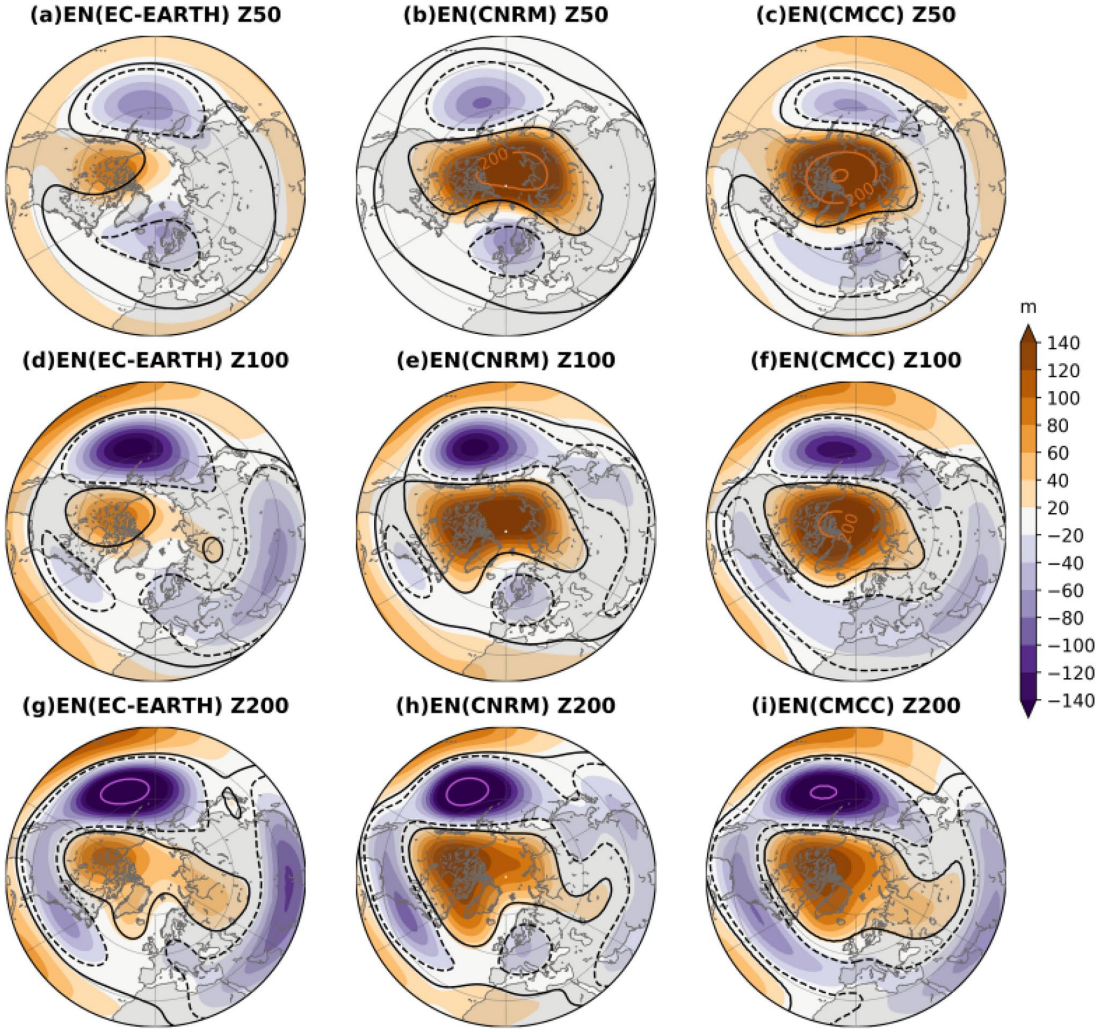

Fig. 7 Ensemble-mean geopotential height anomalies for EN with respect to CTL in JFM at 50 (top), 100 (middle) and 200 hPa (bottom): EC-EARTH (left), CNRM (middle), CMCC (right). Orange and magenta contours show values exceeding the color scale limit at ± 200, and ± 300 m. Black contours (solid for positive, dashed for negative anomalies) indicate statistically significant areas at the 95% confidence level

at 200, 100 and 50 hPa (Figs. 7 and 8). For EN (Fig. 7), a prominent difference stands out between EC-EARTH and the other two models: the magnitude and extension of the high-latitude positive center of action. In CNRM and CMCC (Fig. 7, middle and right columns), the positive anomaly at 200 hPa is stronger over North America with moderate values over the polar cap (Fig. 7h,i). It strengthens with increasing height (Fig. 7e,f), comparing well with the reanalysis (Fig. 11b), and shows maximum amplitude at 50 hPa north of 70°N (Fig. 7b, c) and again, like the temperature anomalies, placed in the North Pacific sector (Fig. 5b, c, e, f, h, and i). The anomalous anticyclonic circulation associated with this high-pressure system over the polar cap is also dynamically consistent with the weakening of the lower stratospheric westerly winds (Fig. 3b, c), in accordance with quasi-geostrophic balance. In EC-EARTH, by contrast, this positive center of action has smaller amplitude already at 200 hPa (Fig. 7g). More importantly, while it is centered over Canada as in the other two models, it only weakly extends towards the pole. At upper levels, it further weakens

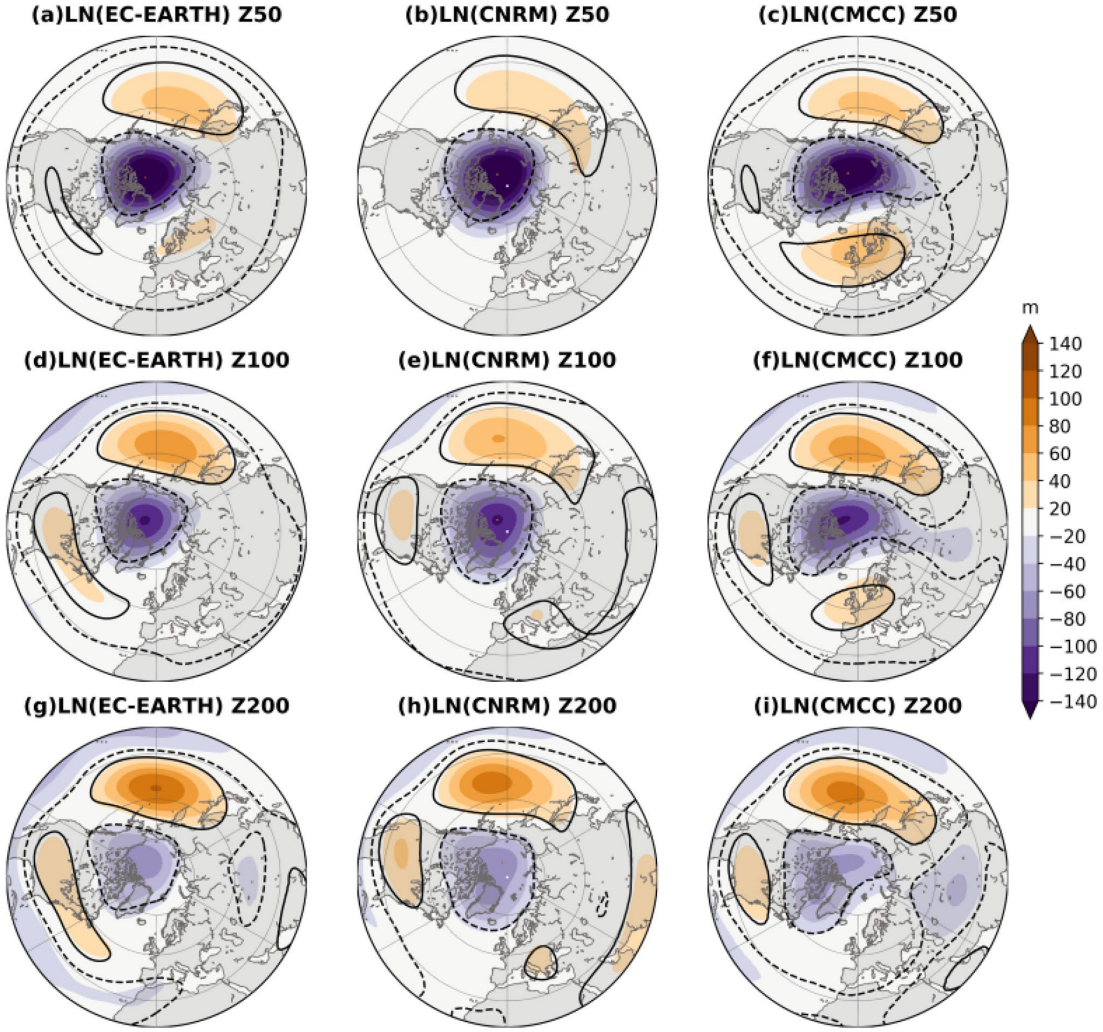

Fig. 8 Ensemble-mean geopotential height anomalies for LN with respect to CTL in JFM at 50 (top), 100 (middle) and 200 hPa (bottom): EC-EARTH (left), CNRM (middle), CMCC (right). Black contours (solid for positive, dashed for negative anomalies) indicate statistically significant areas at the 95% confidence level

over the polar cap, where it shows almost no signal, and is confined to the Western Hemisphere between ~ 180° and 120° W (Fig. 7d, a). The lack of circulation anomalies over the polar region agrees with the missing response in the zonal-mean zonal wind at 100 and 50 hPa (Fig. 3a), again in accordance with quasi-geostrophic balance, drawing the attention to this anomalous anticyclone over Canada, as already noted by Sassi et al. (2004). Note that, in all models, the negative anomaly in the Pacific (the first center of action of the Rossby wave train forced by EN) reinforces the climatological Aleutian Low in the troposphere, but in the stratosphere it is mostly superimposed to positive values of the climatological stationary wave pattern, preventing linear constructive interference over the mid-latitude eastern North Pacific (cf. Figures 7 and 2g–l). In the North Atlantic sector, the dipole-like pattern near the surface (Fig. 1a–c) extends to only 200 hPa (Fig. 7g–i), with only the southern lobe remaining at 100 hPa and disappearing beyond that.

Similarly to what was observed for temperature, EC-EARTH largely agrees with the other models for LN (Fig. 8). The forced wave train tends to be shifted westward in mid-latitudes compared to its EN counterpart (Mezzina

et al. 2021) and the negative anomaly over Canada peaks at higher latitudes, i.e., north of 70°N (cf. bottom rows in Figs. 7 and 8). It amplifies with increasing altitude but maintains its structure, largely covering the polar cap (Fig. 8a–f), although slightly displaced towards the North Pacific sector, like the temperature anomalies (Fig. 6a–f). The anomalous cyclonic circulation associated with this low-pressure system over the polar cap is again consistent with the strengthening of the zonal-mean westerly winds at lower stratospheric levels (Fig. 3h–i), according to quasi-geostrophic balance. As for temperature, weak significance is found in the observational composite for La Niña (Fig. 11f), in line with the zonal-mean zonal wind response (Fig. 11e).

We have found that EC-EARTH is able to capture the expected geopotential height response for LN, but not for EN, in contrast to the other models (which behave symmetrically). While this model is not completely failing in simulating the anomalous high over Canada in EN, the lack of positive geopotential height anomalies over the polar cap in the lower stratosphere is consistent with the wrong zonal wind response and appears to be related to the missing warming of the lower stratosphere.

3.6 ENSO signal in the middle-upper stratosphere

We now turn to the middle-upper stratosphere and examine in detail the circulation (Z) response to ENSO above 50 hPa. For EN (Fig. 9), CNRM and CMCC show already at 10 hPa a pattern with a strong WN1 component, which dominates at all levels (Fig. 9, middle and right columns). This response appears to be related to the lower-stratospheric anomalies, which propagate upwards, as suggested by the westward tilt with height, and adopt this predominantly WN1 structure due to the stronger westerly winds and the Charney-Drazin wave filtering (Fig. 2; see Sect. 3.1). In these two models, the geopotential height anomalies, which grow in amplitude with increasing height (cf. Figures 9 and 7), are largely in phase with the climatological wave pattern at all levels. In particular, the positive anomaly strengthens the stratospheric Aleutian High, while the negative one reinforces the cyclonic circulation associated with the vortex displacement in the North Atlantic sector (cf. Figs. 9 and 2): the net result is a weakening of the vortex (Fig. 3b, c) and a displacement towards Greenland (e.g. Harvey and Hitchman 1996; Harvey et al. 2002; Nigam and DeWeaver 2003). In EC-EARTH, in contrast, the 10 hPa pattern is more reminiscent of a WN2 structure, related to the distinct lower stratospheric response and to the weaker climatological winds between 50 and 10 hPa (Fig. 3a), which do not effectively filter out smaller components. At 5 and 1 hPa, the winds are strong enough for the WN1 component to become dominant (Figs. 3a, 9a, d) and the response is more similar to that of the other two models, again showing a strengthening of the stratospheric Aleutian High. Note, however, that the anomalies barely reach the polar cap, which is consistent with the erroneous response in the zonal-mean zonal wind at high latitudes (Fig. 3a).

The westward tilt with height of the anomalies in the middle-upper stratosphere is a common aspect to all models (Fig. 9) that indicates upward propagation of (stationary) wave activity, which is in turn associated with positive anomalous v^*T^* (see Sect. 2.2). This would appear to be in contrast with the lack of a vertical EP-flux component in EC-EARTH between 50 and 10 hPa (Fig. 4a); we note, however, that anomalous positive v^*T^* is present at 50 hPa outside the polar cap (Fig. 12d), cancelling out in the zonal mean. It is only at 10 hPa that anomalous positive v^*T^* appears at high latitudes, north of 70ºN, and dominates the zonal mean (Fig. 12a), consistent with the EP-flux vectors and in agreement with CNRM and CMCC (Figs. 4, 12). Therefore, there is upward wave propagation from the lowermost throughout the middle-upper stratosphere in all models, including EC-EARTH.

As before, for LN there is more consistency across the models (Fig. 10), although CMCC shows a stronger WN1 pattern that is symmetric in structure to that in EN (cf. Figs. 9 and 10, right column): here, the anomalies are out of phase with the climatological stationary eddy field and the stratospheric Aleutian High is weakened, thereby the vortex is reinforced and shifted towards the North Pacific sector (cf. Figs. 10 and 2, right columns). While it is less evident, in EC-EARTH and CNRM, the cyclonic anomaly is also off-centered with respect to the pole, towards the North Pacific (Fig. 10, left and middle columns), hence also destructively interfering with the climatological Aleutian High (see Fig. 2). This overall WN1 component of the response to La Niña in the upper stratosphere (see also Mezzina et al. 2021) is in agreement with the model results of Manzini et al. (2006). In all models, the westward tilt with height is again evident, but less pronounced than for EN. While the amplitude of the circulation anomalies slightly increases with height from the lower (Fig. 8) to the middle stratosphere, they weaken and lose statistical significance at the stratopause (1 hPa), particularly in EC-EARTH (Fig. 10a) and CMCC (Fig. 10c), which may be indicative of wave dissipation at this level.

Note that the response in LN is again weaker than in EN, highlighting the importance of examining longitude-latitude maps of the anomalies at some key levels to complement the zonal-mean analysis, which instead showed a similar amplitude for EN and LN in CNRM (see Sect. 3.2), due to the WN1 character of the response. This is also true for the temperature anomalies, which appear to be confined to the lower stratosphere in the zonal mean (Fig. 3), but are in

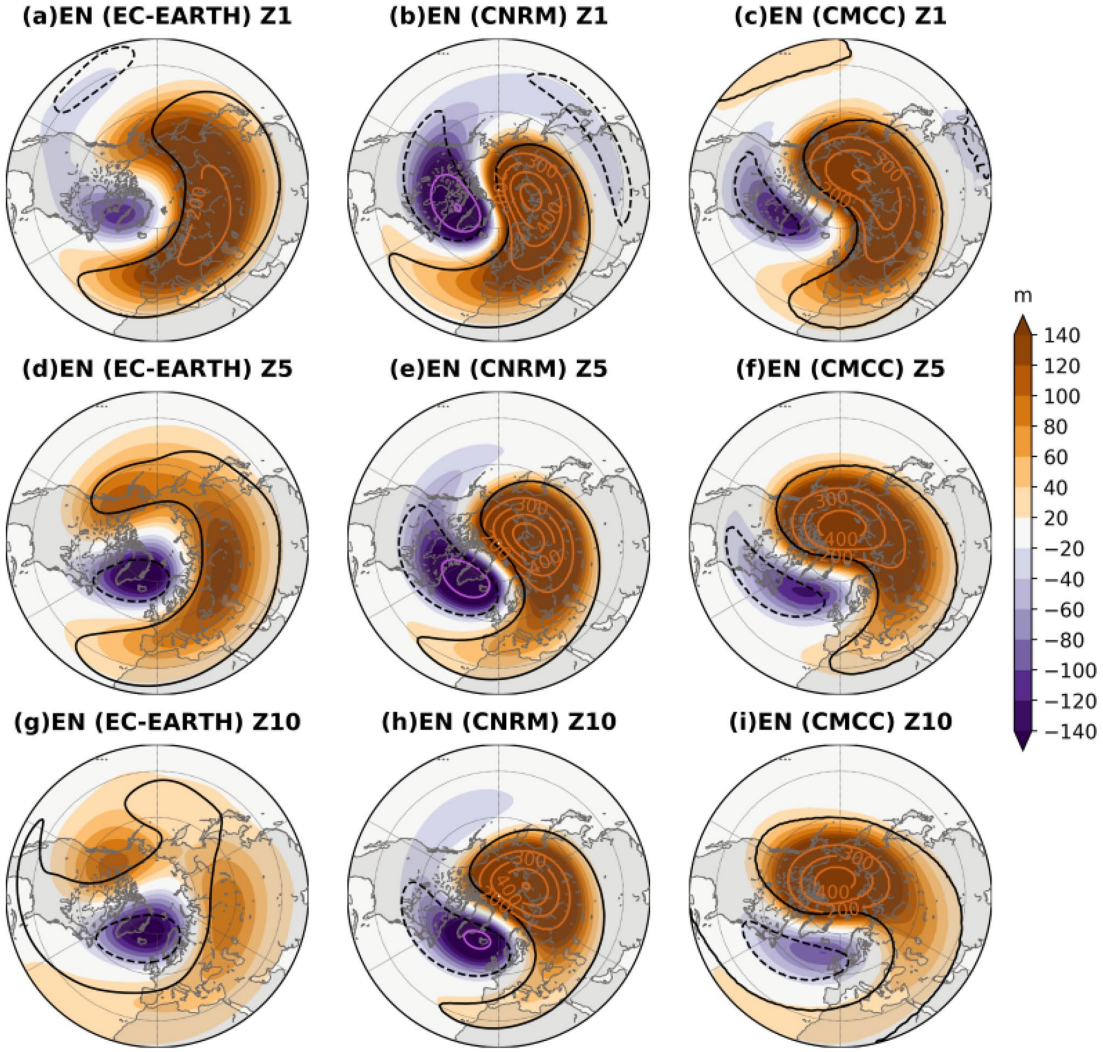

Fig. 9 Ensemble-mean geopotential height anomalies for EN with respect to CTL in JFM at 1 (top), 5 (middle) and 10 hPa (bottom): EC-EARTH (left), CNRM (middle), CMCC (right). Orange and magenta contours show values exceeding the color scale limit at $\pm 200, \pm 300, \pm 400$ and ± 500 m. Black contours (solid for positive, dashed for negative anomalies) indicate statistically significant areas at the 95% confidence level

fact present with a similar WN1 pattern in the middle-upper stratosphere (not shown; in agreement with Sassi et al. 2004; Manzini et al. 2006).

3.7 Interpreting the polar cap temperature anomalies

The presented results suggest that the ENSO circulation anomalies in the stratosphere are mainly associated with a propagating wave rather than a dissipating wave, in agreement with previous studies (e.g. Sassi et al. 2004; Manzini et al. 2006). It relies on the SST-forced, stationary tropospheric Rossby wave train, which propagates upwards and is eventually filtered into a WN1 pattern with no apparent wave breaking. As such, and since the fundamental mechanism underlying Rossby wave propagation is that potential vorticity of the fluid parcels is conserved (e.g. Vallis 2017), the ENSO temperature anomalies in the lower stratosphere,

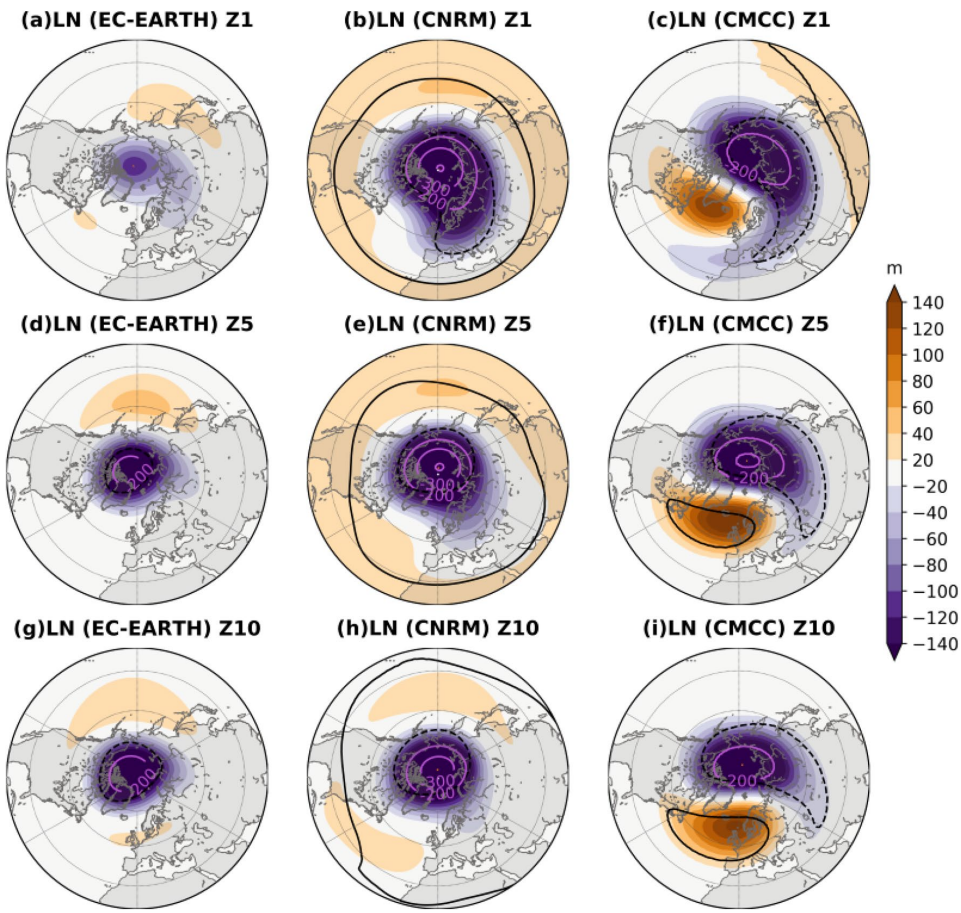

Fig. 10 Ensemble-mean geopotential height anomalies for LN with respect to CTL in JFM at 1 (top), 5 (middle) and 10 hPa (bottom): EC-EARTH (left), CNRM (middle), CMCC (right). Orange and magenta contours show values exceeding the color scale limit at ± 200, ± 300, ± 400 and ± 500 m. Black contours (solid for positive, dashed for negative anomalies) indicate statistically significant areas at the 95% confidence level

which are in hydrostatic balance with the geopotential height anomalies (see Fig. S2 in the Supplementary Material), could be interpreted in terms of changes in stretching vorticity (see Sect. 2.2). For EN, linked to the anomalous anticyclonic circulation over Canada, a decrease in relative vorticity would be balanced by anomalous shrinking of some layers in the air column, implying an anomalous differential warming while conserving angular momentum. Yet, where horizontal motion dominates vertical motion, i.e. mid-latitudes, changes in thickness are negligible; hence, for this shrinking to be effective, the wave train has to reach the polar vortex region (Fig. 2), as in CNRM and CMCC (Fig. 7, middle and right column), but not in EC-EARTH (Fig. 7, left column). For LN, similarly, the anomalous cyclonic circulation at high latitudes would be associated with anomalous stretching and differential cooling, to balance the increase in relative vorticity. In this case, however, the arching pathway of the wave train is such that it consistently spreads over the polar vortex region in the three models (Fig. 8), yielding a robust cooling of the polar cap (Figs. 3j–l, 6).

This framework of thermodynamic adjustment in the lower stratosphere, based on the balance of relative vorticity and stretching vorticity, operates at monthly time-scale in both the EN and LN experiments (see Figs. S3–S8 in the Supplementary Material). Further research is warranted to explore this hypothesis more in depth.

4 Summary and discussion

We have used three state-of-the-art atmospheric models (EC-EARTH, CNRM and CMCC) and 50-member ensembles to study the impacts of idealized and symmetric El Niño and La Niña SST forcings on the Northern Hemisphere polar stratosphere in late winter (JFM). We have analyzed the ensemble-mean responses to strong ENSO events and found that they are similar to each other and to observations for La Niña, but not for El Niño, whose response is misrepresented by one of the models, and have profited from this difference to investigate the driving mechanisms of the ENSO teleconnection to the polar stratosphere. It is commonly considered that anomalous vertical propagation and breaking of planetary waves is key for the ENSO impact on the polar vortex. However, our results suggest that the ENSO response in the stratosphere is mainly driven by the upward propagation of the wavenumber-1 (WN1) component of the tropospheric Rossby wave train triggered by ENSO, starting over Canada at the tropopause and reaching the stratopause while tilting westward with height and projecting on the stratospheric Aleutian High. At lower stratospheric levels, the ENSO-forced geopotential height anomalies at high latitudes are hydrostatically consistent with temperature anomalies around the polar vortex, which is interpreted in terms of shrinking/stretching since they are linked to a (reversible) distortion of the vortex without wave breaking. In accordance with quasi-geostrophic balance, the geopotential height anomalies associated with the upward propagation of the high-latitude WN1 pattern are responsible for the zonal wind anomalies related to the polar vortex. These temperature and zonal wind perturbations in the zonal average are those required to maintain thermal wind balance, implying a consistent anomalous vertical zonal-wind shear at middle-upper stratospheric levels. In the following, our main findings are discussed into context:

1. The two models that properly capture the well-known temperature and zonal wind El Niño signal in the late-winter stratosphere, i.e. warming at lower levels at polar latitudes and weakening of the polar vortex, indicate that the response to La Niña is symmetric in terms of opposite signed-patterns, but has smaller amplitude (about half). Mixed results are present in the literature concerning this (a)symmetry. The studies around the time of Brönnimann's (2007) review and in the subsequent years only addressed the impact of El Niño (e.g. Bell et al. 2009; Cagnazzo and Manzini 2009; Ineson and Scaife 2009) or mainly followed a linear El Niño-La Niña approach (e.g. Sassi et al. 2004; Taguchi and Hartmann 2006), although in some cases weaker and less significant anomalies for La Niña were reported (e.g. Manzini et al. 2006). More recently, Hurwitz et al. (2014), Rao and Ren (2016a, b) and Hardiman et al. (2019) found a large degree of symmetry in the polar stratospheric response to strong, canonical El Niño and La Niña events, as did Calvo et al. 2017 (El Niño) and Iza et al. 2016 (La Niña), using coupled simulations and several reanalysis products. Weinberger et al. (2019) examined a 41-member ensemble forced with observed SSTs and also found linearity for El Niño and La Niña. Trascasa-Castro et al. (2019) used an idealized, symmetric ENSO-like SST forcing of increasing amplitude: for strong events, they found winter anomalies in the zonal-mean zonal wind and EP flux/divergence symmetric in sign but weaker in La Niña. Our results in the stratosphere are similar to what Mezzina et al. (2021) found for the troposphere, where the asymmetry in the magnitude of the response was related to the different energy available from the tropical Pacific in the two ENSO phases (linked to total SSTs). They suggested that the asymmetry in the tropospheric and surface response is not indicative of different mechanisms at play for the teleconnection of El Niño and La Niña, and here we reach the same conclusion for the impacts on the stratosphere.
2. The anomalous circulation over Canada of tropospheric origin is key for the ENSO response in both the lower and middle-upper stratosphere. In the case of El Niño (La Niña), it is an anticyclonic (cyclonic) circulation belonging to the large-scale Rossby wave train that constitutes the main feature of the tropospheric response to ENSO. In the two models that are properly capturing the stratospheric response to El Niño, this center of action extends north of 70° N even at 200 hPa and increases with height in amplitude and extent, reinforcing the climatological Aleutian High in the middle-upper stratosphere. In the model that does not capture the weakening of the vortex and the lower-stratospheric warming, the anomalous center of action remains confined outside the polar cap at all levels, growing with height only in the upper stratosphere (above 10 hPa), where it also reinforces the Aleutian High. For La Niña, instead, the anomalous cyclonic circulation is correctly placed in all the models, possibly because of the slightly different arching path of the tropospheric Rossby wave train (Mezzina et al. 2021). As reviewed by Brönnimann (2007), the relevance of the ENSO-related geopotential height anomaly over Canada was already reported in the earlier works addressing the ENSO impacts on the stratosphere (van Loon and Labitzke 1987; Hamilton 1993a, b, 1995; Baldwin and O'Sullivan 1995), and was later stressed by other studies such as Sassi et al. (2004), Manzini et al. (2006) and Cagnazzo and Manzini (2009). In this latter work, the authors presented results from a "high-top" model that simulates, for El Niño, an anomalous anticyclone at 50 hPa expanding over the polar cap, and from a "low-top" model for

which the anomaly remains confined over Canada, similarly to EC-EARTH (see their Fig. 3); they also found that the zonal-mean temperature anomaly at 80°N was weaker in the "low-top" model (see their Fig. 1). That this anomalous circulation over Canada could play such a key role is somewhat in contrast with the more recent interpretation of the ENSO teleconnection to the stratosphere in terms of linear constructive (destructive) interference of the strengthened (weakened) tropospheric Aleutian Low during El Niño (La Niña) with the climatological wave pattern in the North Pacific mid-latitudes (e.g. Garfinkel and Hartmann 2008; Ineson and Scaife 2009; see the review by Domeisen et al. 2019). Our results instead agree with the early studies and stress the crucial role of the anomalous circulation over Canada.

3. We suggest that the temperature anomalies in the lower stratosphere could be interpreted in terms of shrinking/stretching. The anomalous relative vorticity associated with the center of action over Canada, anticyclonic (cyclonic) for El Niño (La Niña), is balanced by anomalous shrinking (stretching) at polar latitudes, whose thermodynamical adjustment imply anomalous differential warming (cooling). We note that this anomalous circulation over Canada constitutes the key center of action of the wavenumber-1 (WN1) pattern that is filtered as it propagates vertically through the stratosphere. Our results suggest an alternative view to the current understanding of the ENSO impact on the stratosphere, based on the wavenumber-0 (WN0) response of the polar vortex driven by increased (decreased) wave forcing during El Niño (La Niña), associated with a deceleration (acceleration) and a warming (cooling) (see Domeisen et al. 2019 for a review). Our findings, instead, agree with previous works showing that the zonally-asymmetric, WN1 response to ENSO prevails over WN0, zonal-mean changes of the stratospheric circulation (e.g. Hamilton 1993a, 1993b; Baldwin and O'Sullivan 1995; Sassi et al. 2004), as well as with theoretical considerations where stationary, conservative, linear planetary waves, such as the ENSO-forced Rossby wave train, are incapable of inducing changes in the zonal-mean stratospheric flow (see Andrews et al. 1987 for a review).
4. The ENSO signal in the middle-upper stratosphere (above 50 hPa) projects onto a WN1 pattern, reminiscent of the climatological stationary eddy, for both El Niño and, more weakly, La Niña. The El Niño- (La Niña-) related geopotential height anomalies are in phase (out of phase) with the climatological wave pattern and reinforce (lessen) the climatological Aleutian High in the middle-upper stratosphere, resulting in a weakening (strengthening) of the polar vortex and a displacement towards the North Atlantic (North Pacific) sector. These features have been reported in previous works, from earlier (e.g. van Loon and Labitzke 1987; Hamilton 1993a, b, 1995; Sassi et al. 2004; Manzini et al. 2006) to more recent ones (e.g. Rao and Ren 2016a, b), but only for El Niño. Moreover, the anomalies show a westward tilt with height, which indicates upward propagation of wave activity, as reported in the same earlier studies (e.g. Hamilton 1995; Sassi et al. 2004; Manzini et al. 2006). Our results suggest that this response is related to the upward propagation of the lower-stratospheric anomalies and that thus wave breaking is not associated with this response (see point 3.); instead, the wave activity continues to propagate upwards into the higher stratosphere and the mesosphere, aligned with Sassi et al. (2004).

The results presented here complement those of Mezzina et al. (2020, 2021) in suggesting that the ENSO signal over the NAE region, the "canonical" SLP dipole between mid and high latitudes, is mostly driven by the tropospheric pathway. Indeed, even in EC-EARTH the canonical SLP dipole is present during El Niño—although weaker over high latitudes compared to the other models—despite the erroneous stratospheric response. However, we acknowledge that lower-stratospheric circulation anomalies may propagate to the surface and induce SLP anomalies at polar/high latitudes via, for example, the same potential vorticity adjustment described above, as suggested by Ambaum and Hoskins (2002). Experiments with a stratosphere nudged to climatology (versus a free stratosphere), as in Jiménez-Esteve and Domeisen (2019), would allow to further isolate the stratospheric and tropospheric contributions to the ENSO-NAE signal.

There are many scientific questions concerning the ENSO impact on the stratosphere and the teleconnection to the NAE sector that remain open, but one that is not often discussed concerns a secondary center of action in SLP that was noticed, but not discussed, in Mezzina et al. (2020, 2021). It appears over Europe in the geopotential height field in the troposphere and lower stratosphere (Figs. 7, 8), albeit not always clearly. It is not straightforward to associate this anomaly with tropospheric processes, such as a split of the main wave train crossing the North Pacific-American sector (García-Serrano et al. 2011) or a secondary wave train triggered from the tropical Atlantic (Toniazzo and Scaife 2006), or with stratospheric ones, e.g. linked to the displacement of the polar vortex at 50–10 hPa, nor is it clear its role in the teleconnection, for which investigation is required.

Appendix 1: observational composites

Figure 11 shows observational composites of El Niño (a–d) and La Niña (e–h) in JFM. We use the same dataset (ECMWF ERA-20CR; Poli et al. 2016), period (1900–2010)

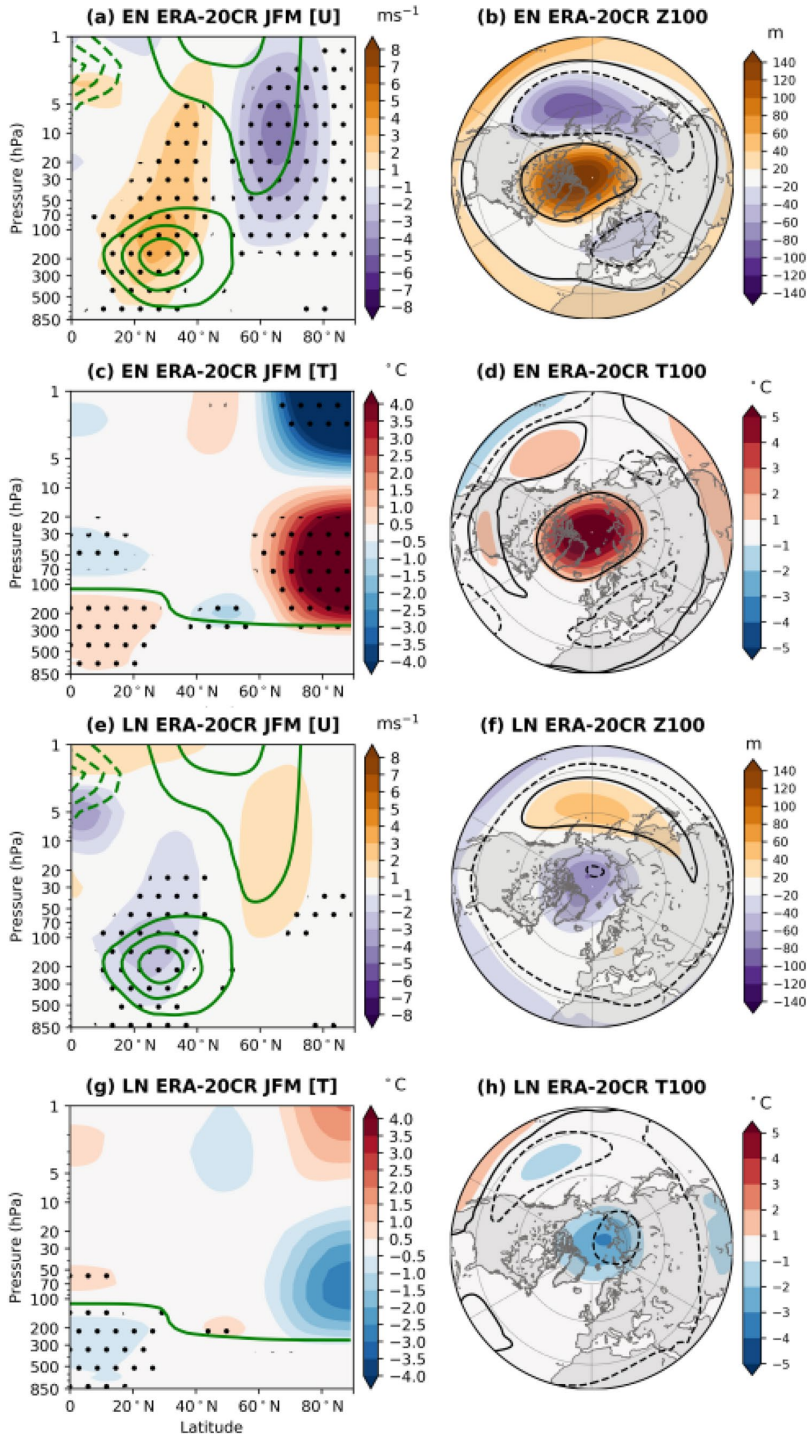

Fig. 11 **a**–**d** JFM composites of El Niño anomalies using data from ECMWF ERA-20CR (Poli et al. 2016) over 1900–2010: zonal-mean zonal wind (**a**) and temperature (**c**); 100-hPa geopotential height (**b**) and temperature (**d**). **e**–**h** Same, but for La Niña. Green contours in the zonal wind panels show its climatology (contour interval: 10 ms^{-1}) and the green line in the zonal-mean temperature panels depicts the tropopause level, according to the WMO's definition (lowest level at which the lapse rate decreases to 2 °C/km or less). Black contours (solid for positive, dashed for negative anomalies) indicate statistically significant areas at the 95% confidence level

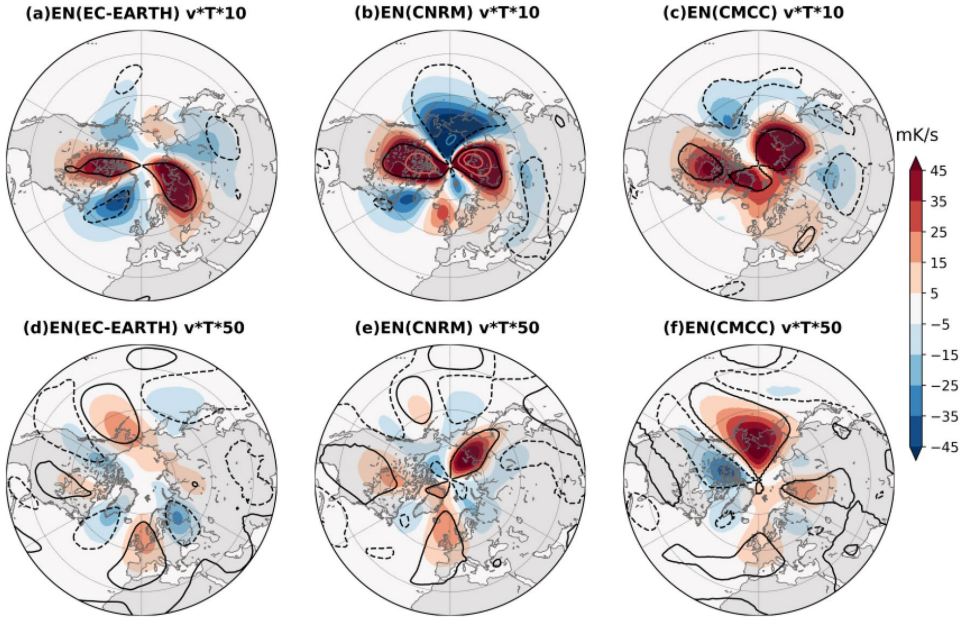

Fig. 12 Ensemble-mean eddy-heat flux anomalies for EN with respect to CTL in JF at 10 (top) and 50 hPa (bottom): EC-EARTH (left), CNRM (middle), CMCC (right). Red and blue contours show values exceeding the color scale limit at $\pm 200, \pm 300, \pm 400$ and ± 500 m. Black contours (solid for positive, dashed for negative anomalies) indicate statistically significant areas at the 95% confidence level

and methods as in Mezzina et al. 2021, stratifying El Niño (La Niña) years according to a threshold of $+1$ (-1) standard deviation of the JFM Niño3.4-index. 18 EN and 19 LN years are selected, using SST from HadISST1.1.

Appendix 2: longitude-latitude maps of v*T*

Figure 12 shows maps of anomalous v^*T^* in EN at 50 and 10 hPa, as discussed in Sect. 3.7.

Supplementary Information The online version contains supplementary material available at https://doi.org/10.1007/s00382-021-05836-3.

Acknowledgements This work was supported by the MEDSCOPE project. MEDSCOPE is part of ERA4CS, an ERA-NET initiated by JPI Climate, and funded by AEMET (ES), ANR (FR), BSC (ES), CMCC (IT), CNR (IT), IMR (BE) and Météo-France (FR), with co-funding by the European Union (Grant 690462). B.M. and J.G.-S. were supported by the "Contratos Predoctorales para la Formación de Doctores" (BES-2016-076431) and "Ramón y Cajal" (RYC-2016-21181) programmes, respectively. F.M.P. was partially supported by the Spanish DANAE (CGL2015-68342-R) and GRAVITOCAST (ERC2018-092835) projects. Technical support at BSC (Computational Earth Sciences group) is sincerely acknowledged. We also thank the two anonymous reviewers for their helpful feedback.

References

Ambaum MHP, Hoskins BJ (2002) The NAO troposphere-stratosphere connection. J Clim 15(14):1969–1978. https://doi.org/10.1175/1520-0442(2002)015%3c1969:TNTSC%3e2.0.CO;2

Andrews DG, Holton JR, Leovy CB (1987) Middle atmosphere dynamics. International geophysics series, vol 40. Academic Press, p 489

Ayarzagüena B, Ineson S, Dunstone NJ, Baldwin MP, Scaife AA (2018) Intraseasonal effects of El Niño-Southern oscillation on North Atlantic climate. J Clim 31:8861–8873. https://doi.org/10.1175/JCLI-D-18-0097.1

Baldwin MP, O'Sullivan D (1995) Stratospheric effects of ENSO-related tropospheric circulation anomalies. J Clim 8:649–667.

https://doi.org/10.1175/1520-0442(1995)008%3c0649:SEOERT%3e2.0.CO;2
Bell CJ, Gray LJ, Charlton-Perez AJ, Joshi MM, Scaife AA (2009) Stratospheric communication of El Niño teleconnections to European winter. J Clim 22:4083–4096. https://doi.org/10.1175/2009JCLI2717.1
Benassi M, Conti G, Gualdi S et al (2021) El Niño teleconnection to the Euro-Mediterranean late-winter: the role of extratropical Pacific modulation. Clim Dyn. https://doi.org/10.1007/s00382-021-05768-y (**in press**)
Brönnimann S (2007) Impact of El Niño-Southern Oscillation on European climate. Rev Geophys 45:RG3003. https://doi.org/10.1029/2006RG000199
Butler AH, Polvani LM, Deser C (2014) Separating the stratospheric and tropospheric pathways of El Niño-Southern Oscillation teleconnections. Environ Res Let 9:024014. https://doi.org/10.1088/1748-9326/9/2/024014
Cagnazzo C, Manzini E (2009) Impact of the stratosphere on the winter tropospheric teleconnections between ENSO and the North Atlantic and European Region. J Clim 22:1223–1238. https://doi.org/10.1175/2008JCLI2549.1
Calvo N, Garcia RR, Randel WJ, Marsh DR (2010) Dynamical mechanism for the increase in tropical upwelling in the lowermost tropical stratosphere during warm ENSO events. J Atmos Sci 67(7):2331–2340. https://doi.org/10.1175/2010JAS3433.1
Calvo N, Iza M, Hurwitz MM, Manzini E et al (2017) Northern hemisphere stratospheric pathway of different El Niño flavors in stratosphere-resolving CMIP5 models. J Clim 30(12):4351–4371. https://doi.org/10.1175/JCLI-D-16-0132.1
Charney JG, Drazin PG (1961) Propagation of planetary-scale disturbances from the lower into the upper atmosphere. J Geophys Res 66:83–109. https://doi.org/10.1029/JZ066i001p00083
Davini P, von Hardenberg J, Corti S et al (2017) Climate SPHINX: evaluating the impact of resolution and stochastic physics parameterisations in the EC-Earth global climate model. Geosci Model Dev 10:1383–1402. https://doi.org/10.5194/gmd-10-1383-2017
Domeisen DIV, Butler AH, Fröhlich K et al (2015) Seasonal predictability over Europe arising from El Niño and stratospheric variability in the MPI-ESM Seasonal Prediction System. J Clim 28:256–271. https://doi.org/10.1175/JCLI-D-14-00207.1
Domeisen DIV, Garfinkel CI, Butler AH (2019) The teleconnection of El Niño Southern Oscillation to the stratosphere. Rev Geophys 57:5–47. https://doi.org/10.1029/2018RG000596
Free M, Seidel DJ (2009) Observed El Niño-Southern Oscillation temperature signal in the stratosphere. J Geophys Res 114:D23108. https://doi.org/10.1029/2009JD012420
García-Herrera R, Calvo N, Garcia RR, Giorgetta MA (2006) Propagation of ENSO temperature signals into the middle atmosphere: a comparison of two general circulation models and ERA-40 reanalysis data. J Geophys Res 111:D06101. https://doi.org/10.1029/2005JD006061
García-Serrano J, Rodríguez-Fonseca B, Bladé I et al (2011) Rotational atmospheric circulation during North Atlantic-European winter: the influence of ENSO. Clim Dyn 37:1727–1743. https://doi.org/10.1007/s00382-010-0968-y
Garfinkel CI, Hartmann DL (2007) Effects of the El Niño-Southern Oscillation and the Quasi-Biennial Oscillation on polar temperatures in the stratosphere. J Geophys Res 112:D19112. https://doi.org/10.1029/2007JD008481
Garfinkel CI, Hartmann DL (2008) Different ENSO teleconnections and their effects on the stratospheric polar vortex. J Geophys Res 113:D18114. https://doi.org/10.1029/2008JD009920
Hamilton K (1993a) A general circulation model simulation of El Nino effects in the extratropical northern hemisphere stratosphere. Geophys Res Let 20:1803–1806. https://doi.org/10.1029/93GL01782
Hamilton K (1993b) An examination of observed southern oscillation effects in the northern hemisphere stratosphere. J Atmos Sci 50:3468–3474. https://doi.org/10.1175/1520-0469(1993)050%3c3468:AEOOSO%3e2.0.CO;2
Hamilton K (1995) Interannual variability in the northern hemisphere winter middle atmosphere in control and perturbed experiments with the GFDL SKYHI general circulation model. J Atmos Sci 52(1):44–66. https://doi.org/10.1175/1520-0469(1995)052%3c0044:IVITNH%3e2.0.CO;2
Hardiman SC, Dunstone NJ, Scaife AA, Smith DM, Ineson S et al (2019) The impact of strong El Niño and La Niña events on the North Atlantic. Geophys Res Lett 46:2874–2883. https://doi.org/10.1029/2018GL081776
Harvey VL, Hitchman MH (1996) A climatology of the Aleutian High. J Atmos Sci 53:2088–2101. https://doi.org/10.1175/1520-0469(1996)053%3c2088:ACOTAH%3e2.0.CO;2
Harvey VL, Pierce RB, Hitchman MH (2002) A climatology of stratospheric polar vortices and anticyclones. J Geophys Res 107(D20):4442. https://doi.org/10.1029/2001JD001471
Horel JD, Wallace JM (1981) Planetary-scale atmospheric phenomena associated with the southern oscillation. Mon Weather Rev 109:813–829. https://doi.org/10.1175/1520-0493(1981)109%3c0813:PSAPAW%3e2.0.CO;2
Hoskins BJ, Karoly DJ (1981) The steady linear response of a spherical atmosphere to thermal and orographic forcing. J Atmos Sci 38:1179–1196. https://doi.org/10.1175/1520-0469(1981)038%3c1179:TSLROA%3e2.0.CO;2
Hurwitz MM, Calvo N, Garfinkel CI et al (2014) Extra-tropical atmospheric response to ENSO in the CMIP5 models. Clim Dyn 43:3367–3376. https://doi.org/10.1007/s00382-014-2110-z
Ineson S, Scaife AA (2009) The role of the stratosphere in the European climate response to El Niño. Nat Geosci 2(1):32–36. https://doi.org/10.1038/ngeo381
Iza M, Calvo N, Manzini E (2016) The stratospheric pathway of La Niña. J Clim 29(24):8899–8914. https://doi.org/10.1175/JCLI-D-16-0230.1
Jiménez-Esteve B, Domeisen DI (2019) Nonlinearity in the North Pacific atmospheric response to a linear ENSO forcing. Geophys Res Lett 46:2271–2281. https://doi.org/10.1029/2018GL081226
Kidston J, Scaife AA, Hardiman SC et al (2015) Stratospheric influence on tropospheric jet streams, storm tracks and surface weather. Nat Geosci 8:433–440. https://doi.org/10.1038/ngeo2424
King MP, Herceg-Bulić I, Bladé I et al (2018) Importance of late fall ENSO teleconnection in the Euro-Atlantic Sector. Bull Am Meteor Soc 99:1337–1343. https://doi.org/10.1175/BAMS-D-17-0020.1
Manzini E, Giorgetta MA, Esch M, Kornblueh L, Roeckner E (2006) The influence of sea surface temperatures on the northern winter stratosphere: ensemble simulations with the MAECHAM5 model. J Clim 19(16):3863–3881. https://doi.org/10.1175/JCLI3826.1
Matsuno T (1971) A dynamical model of the stratospheric sudden warming. J Atmos Sci 28:1479–1494. https://doi.org/10.1175/1520-0469(1971)028%3c1479:ADMOTS%3e2.0.CO;2
Mezzina B, García-Serrano J, Bladé I, Kucharski F (2020) Dynamics of the ENSO teleconnection and NAO variability in the North Atlantic-European Late Winter. J Clim 33:907–923. https://doi.org/10.1175/JCLI-D-19-0192.1
Mezzina B, Garcia-Serrano J, Bladé I et al (2021) Multi-model assessment of the late-winter ENSO teleconnection in the Euro-Atlantic sector. Clim Dyn. https://doi.org/10.1007/s00382-020-05415-y (**in press**)
Nigam S, DeWeaver E (2003) Stationary waves (orographic and thermally forced). In: Holton JR, Pyle JA, Curry JA (eds) Encyclopedia of atmospheric sciences. Academic/Elsevier Sci, London, pp 2121–2137

Oehrlein J, Chiodo G, Polvani LM (2019) Separating and quantifying the distinct impacts of El Niño and sudden stratospheric warmings on North Atlantic and Eurasian wintertime climate. Atmos Sci Lett 20:e923. https://doi.org/10.1002/asl.923

Palmeiro FM, García-Serrano J, Bellprat O et al (2020) Boreal winter stratospheric variability in EC-EARTH: High-Top versus Low-Top. Clim Dyn 54:3135–3150. https://doi.org/10.1007/s00382-020-05162-0

Palmeiro FM, Garcia-Serrano J, Ruggieri P, Batté L, Gualdi S (2021a) Intraseasonal modulation of Sudden Stratospheric Warmings by ENSO. Clim Dyn (submitted)

Palmeiro FM, García-Serrano J, Rodrigo M, Abalos M, Christiansen B, Yang S (2021b) Boreal winter stratospheric climatology: CMIP6 version. Clim Dyn (submitted)

Plumb RA (1985) On the three-dimensional propagation of stationary waves. J Atmos Sci 42(3):217–229. https://doi.org/10.1175/1520-0469(1985)042⟨0217:OTTDPO⟩2.0.CO;2

Poli P, Hersbach H, Dee DP, Berrisford P, Simmons AJ et al (2016) ERA-20C: an atmospheric reanalysis of the twentieth century. J Clim 29:4083–4097. https://doi.org/10.1175/JCLI-D-15-0556.1

Polvani LM, Sun L, Butler AH, Richter JH, Deser C (2017) Distinguishing stratospheric sudden warmings from ENSO as key drivers of wintertime climate variability over the North Atlantic and Eurasia. J Clim 30:1959–1969. https://doi.org/10.1175/JCLI-D-16-0277.1

Rao J, Ren R (2016a) Asymmetry and nonlinearity of the influence of ENSO on the northern winter stratosphere: 1. Observ J Geophys Res Atmos 121:9000–9016. https://doi.org/10.1002/2015JD024520

Rao J, Ren R (2016b) Asymmetry and nonlinearity of the influence of ENSO on the northern winter stratosphere: 2. Model Study with WACCM. J Geophys Res Atmos 121:9017–9032. https://doi.org/10.1002/2015JD024521

Richter JH, Deser C, Sun L (2015) Effects of stratospheric variability on El Niño teleconnections. Environ Res Let 10:124021. https://doi.org/10.1088/1748-9326/10/12/124021

Roehrig R, Beau I, Saint-Martin D et al (2020) The CNRM global atmosphere model ARPEGE-Climat 6.3: description and evaluation. J Adv Model Earth Syst 12:e2020MS002075. https://doi.org/10.1029/2020MS002075

Sanna A, Borrelli A, Athanasiadis P et al (2017) CMCC-SPS3: the CMCC seasonal prediction system 3. CMCC Tech Rep RP 0285:61

Sassi F, Kinnison D, Boville BA, Garcia RR, Roble R (2004) Effect of El Niño-Southern Oscillation on the dynamical, thermal, and chemical structure of the middle atmosphere. J Geophys Res 109:D17108. https://doi.org/10.1029/2003JD004434

Shaw TA, Perlwitz J, Weiner O (2014) Troposphere-stratosphere coupling: Links to North Atlantic weather and climate, including their representation in CMIP5 models. J Geophys Res Atmos 119:5864–5880. https://doi.org/10.1002/2013JD021191

Taguchi M, Hartmann DL (2006) Increased occurrence of stratospheric sudden warmings during El Niño simulated by WACCM. J Clim 19:324–332. https://doi.org/10.1175/JCLI3655.1

Titchner HA, Rayner NA (2014) The Met Office Hadley Centre sea ice and sea surface temperature data set, version 2: 1. Sea ice concentrations. J Geophys Res Atmos 119:2864–2889. https://doi.org/10.1002/2013JD020316

Toniazzo T, Scaife AA (2006) The influence of ENSO on winter North Atlantic climate. Geophys Res Lett 33:L24704. https://doi.org/10.1029/2006GL027881

Trascasa-Castro P, Maycock AC, Scott Yiu YY, Fletcher JK (2019) On the linearity of the stratospheric and Euro-Atlantic sector response to ENSO. J Clim 32:6607–6626. https://doi.org/10.1175/JCLI-D-18-0746.1

Vallis GK (2017) Atmospheric and oceanic fluid dynamics: fundamentals and large-scale circulation, 2nd edn. Cambridge University Press, p 946

Van Loon H, Labitzke K (1987) The Southern oscillation. Part V: the anomalies in the lower stratosphere of the northern hemisphere in winter and a comparison with the Quasi-Biennial Oscillation. Mon Weather Rev 115(2):357–369

Voldoire A, Saint-Martin D, Sénési S et al (2019) Evaluation of CMIP6 DECK experiments with CNRM- CM6-1. J Adv Model Earth Syst 11:2177–2213. https://doi.org/10.1029/2019MS001683

Waugh D, Polvani LM (2010) Stratospheric polar vortices. In the stratosphere, dynamics, transport and chemistry. Geophys Monogr Ser 190:43–57

Weinberger I, Garfinkel CI, White IP, Oman LD (2019) The salience of nonlinearities in the boreal winter response to ENSO: Arctic stratosphere and Europe. Clim Dyn 53:4591–4610

4.1 Supplementary Material

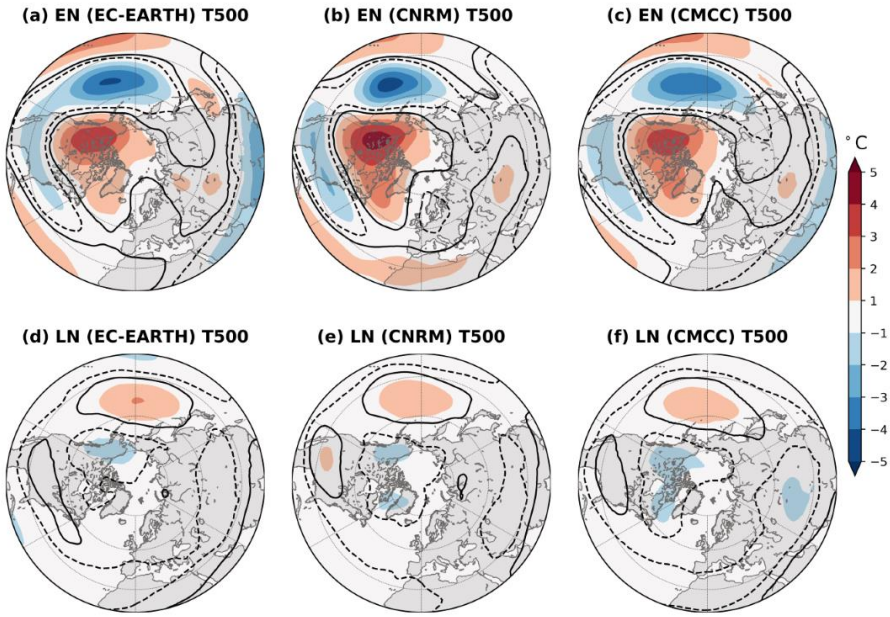

Figure S1. Ensemble-mean temperature anomalies at 500 hPa for EN (top row) and LN (bottom row) with respect to CTL in JFM: EC-EARTH (left), CNRM (middle), CMCC (right). Black contours (solid for positive, dashed for negative anomalies) indicate statistically significant areas at the 95% confidence level

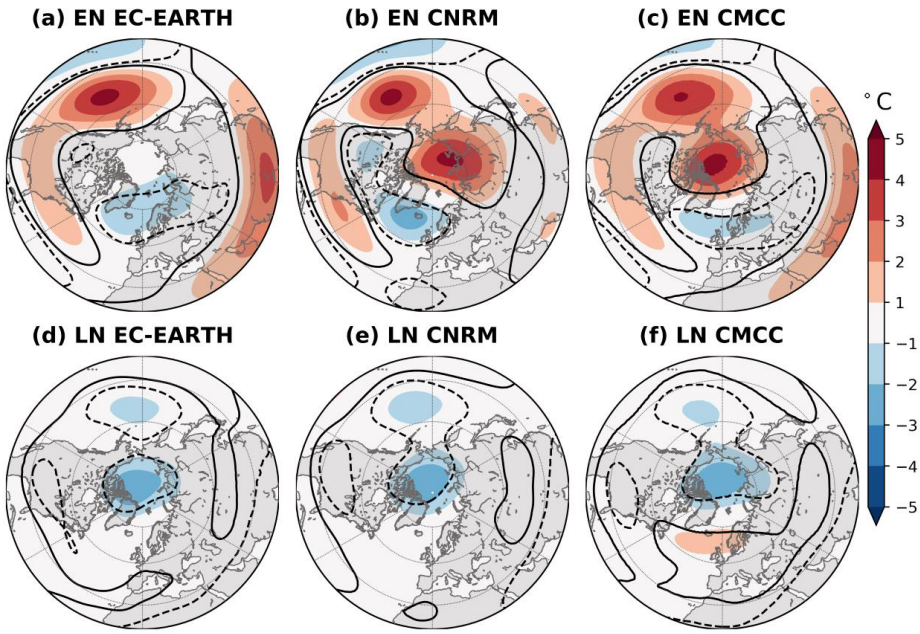

Figure S2. Temperature anomalies at 100 hPa estimated from the geopotential height at 200 and 50 hPa (see Sect. 2.2). EN (top) and LN (bottom) with respect to CTL in JFM: EC-EARTH (left), CNRM (middle), CMCC (right). Black contours (solid for positive, dashed for negative anomalies) indicate statistically significant areas at the 95% confidence level. To be compared with Figs. 5g-i and 6g-i.

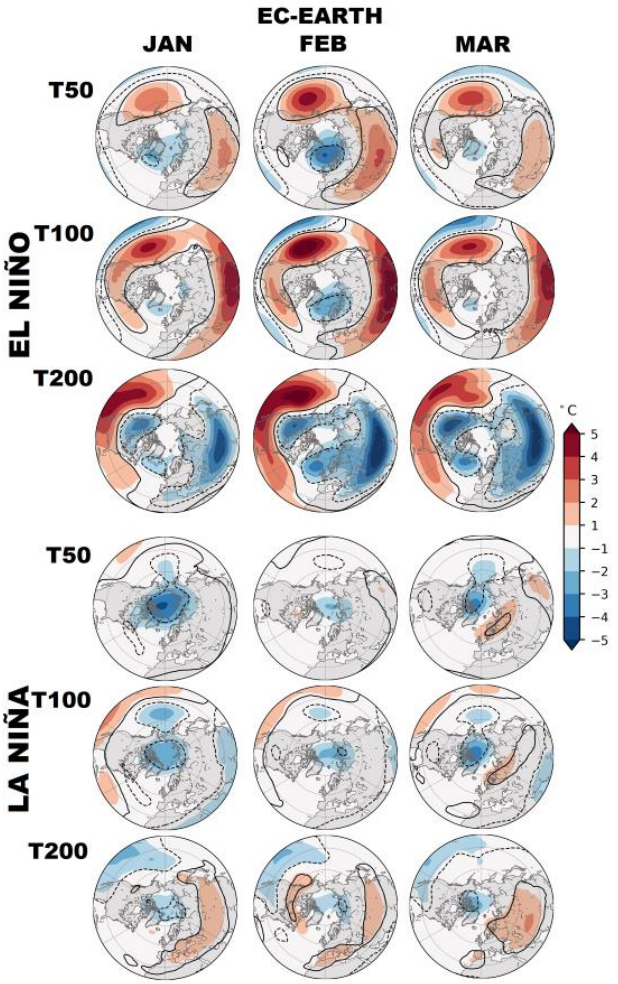

Figure S3. Monthly (January, February, March) temperature anomalies at 200, 100 and 50 hPa in EC-EARTH. EN (top) and LN (bottom) with respect to CTL. Black contours (solid for positive, dashed for negative anomalies) indicate statistically significant areas at the 95% confidence level.

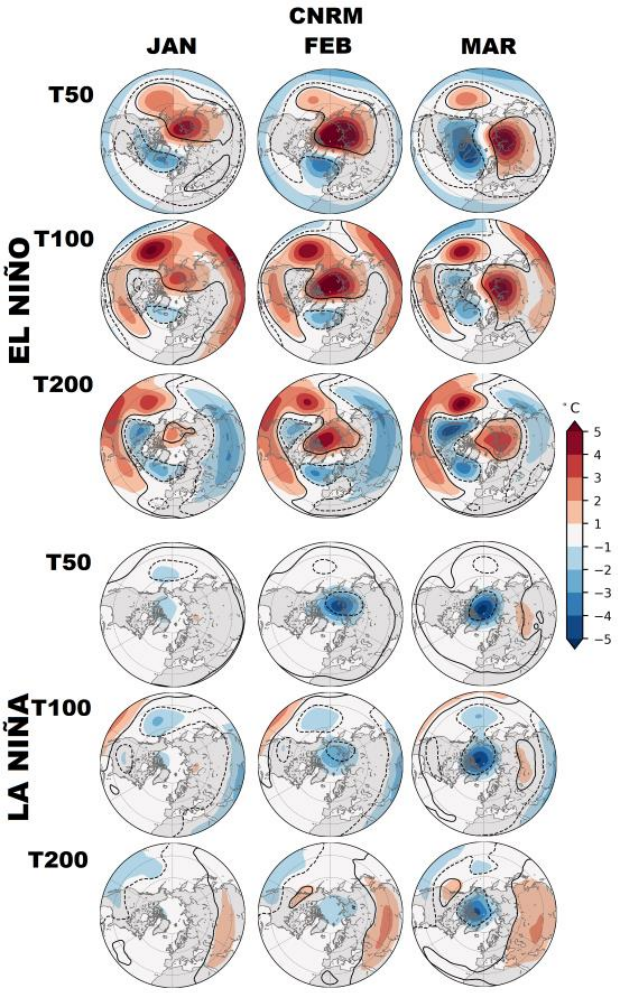

Figure S4. Same as Figure S3, but for CNRM.

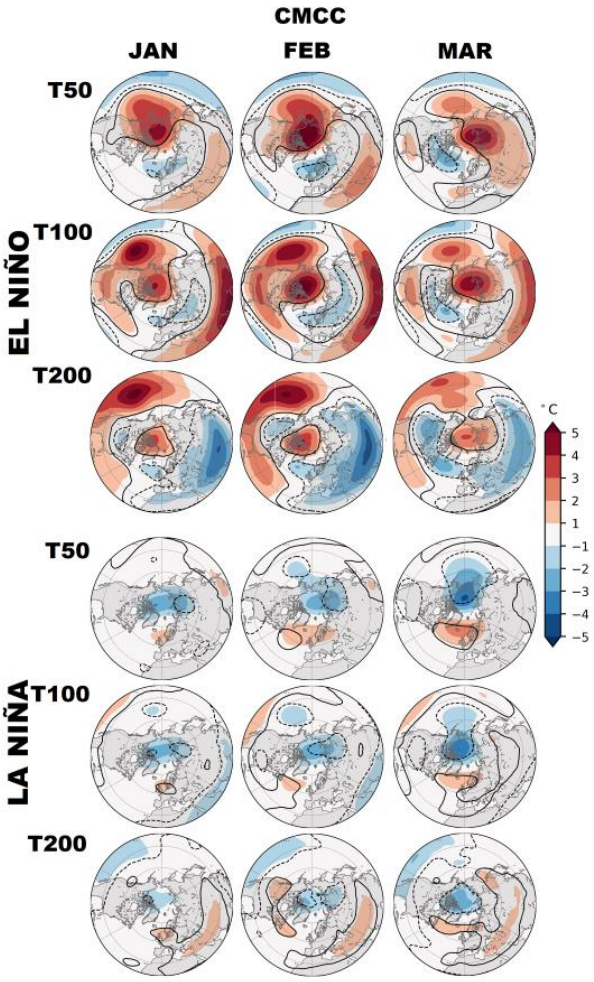

Figure S5. Same as Figure S3, but for CMCC.

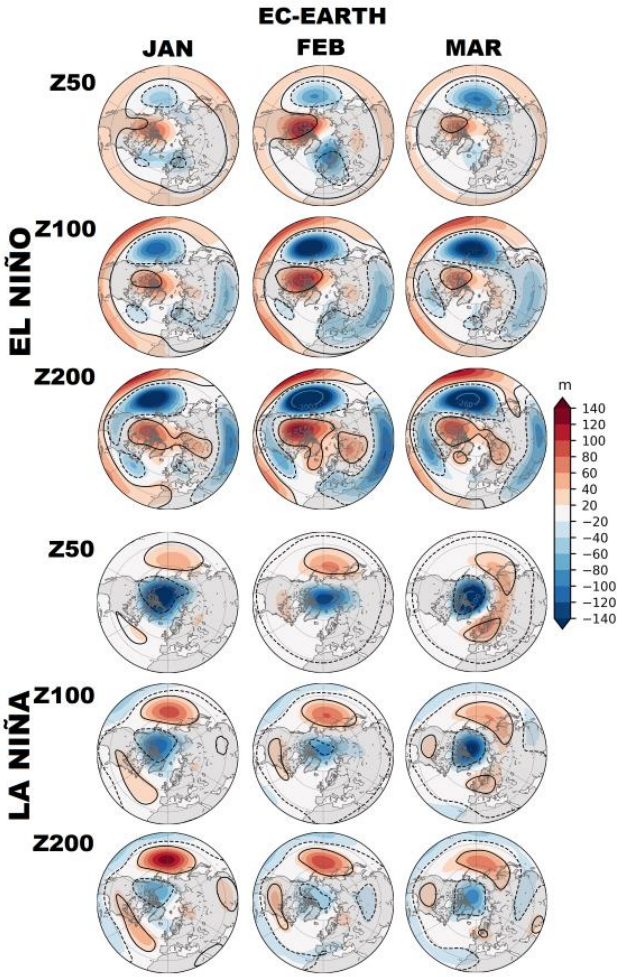

Figure S6. Same as Figure S3, but for geopotential height.

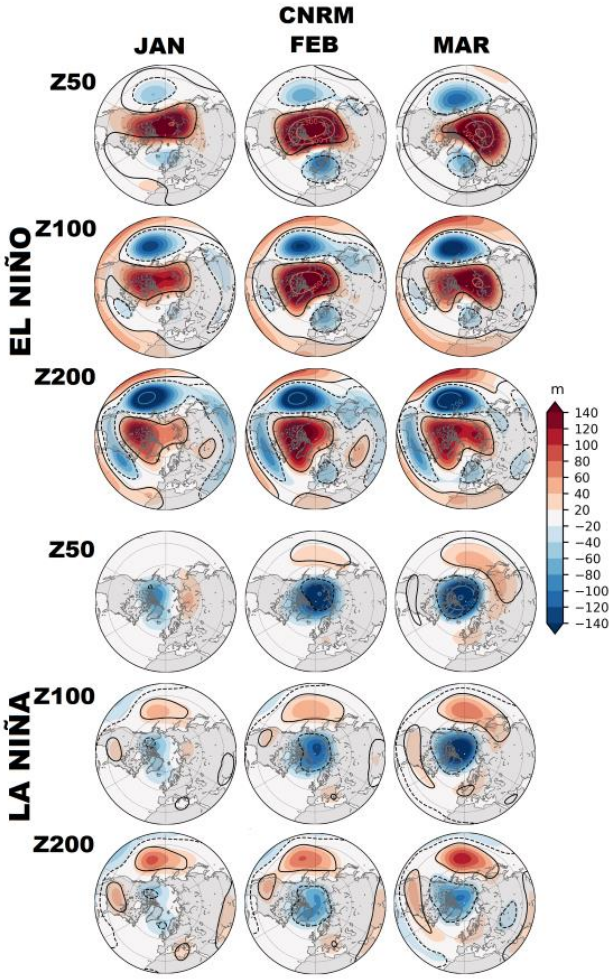

Figure S7. Same as Figure S4, but for geopotential height.

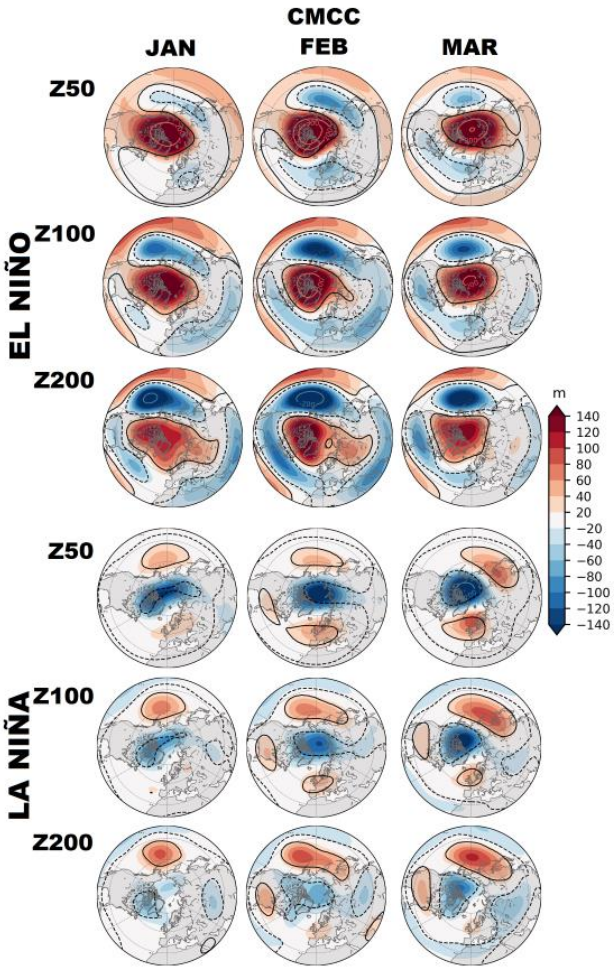

Figure S8. Same as Figure S5, but for geopotential height.

Chapter 5

Tropospheric pathways of the late-winter ENSO teleconnection to Europe

This chapter contains the research article Mezzina et al. 2022 and addresses objective 5 from Sect. 1.3.

Mezzina, B., García-Serrano, J., Ambrizzi, T., Matei, D., Manzini, E., & Bladé, I. (2022). Tropospheric pathways of the late-winter ENSO teleconnection to Europe. *Submitted to Environ. Res. Lett.*

Tropospheric pathways of the late-winter ENSO teleconnection to Europe

Bianca Mezzina[1,2], Javier García-Serrano[1,2], Tercio Ambrizzi[3], Daniela Matei[4], Elisa Manzini[4], Ileana Bladé[2]

[1]Barcelona Supercomputing Center (BSC), Barcelona, Spain
[2]Group of Meteorology, Universitat de Barcelona (UB), Barcelona, Spain
[3]Department of Atmospheric Sciences, Institute of Astronomy, Geophysics and Atmospheric Sciences, University of São Paulo, São Paulo, Brazil
[4]Max-Planck-Institut für Meteorologie, Hamburg, Germany

Abstract

The late-winter signal associated with the El Niño-Southern Oscillation (ENSO) over the European continent is unsettled. Two main anomalous patterns of sea-level pressure (SLP) can be identified: a "wave-like" pattern with two opposite-signed anomalies over Europe, and a pattern showing a single anomaly ("semi-isolated"). In this work, potential paths of the tropospheric ENSO teleconnection to Europe and their role in favoring a more wave-like or semi-isolated pattern are explored. Outputs from historical runs of two versions of the MPI-ESM coupled model, which simulate these two types of patterns, are examined. A novel ray-tracing approach that accounts for zonal asymmetries in the background flow is used to test potential propagation paths in these simulations and in observations; three source regions are considered: the tropical Pacific, the North America/North Atlantic, and the tropical Atlantic. The semi-isolated pattern is suggested to be related to the well-known Rossby wave train emanating from the tropical Pacific, either via a split over northern North America or via reflection due to inhomogeneities in the background flow. The wave-like pattern, in turn, appears to be related to a secondary wave train emerging from the tropical Atlantic. The competition between these two pathways contributes to determining the actual surface response.

1 Introduction

El Niño-Southern Oscillation (ENSO) has been associated with a late-winter (January-March) signal in the North Atlantic-European (NAE) region, a "canonical" sea-level pressure (SLP) dipole between mid and high latitudes (e.g. Brönnimann 2007). The western part of this dipole, which is located over the North Atlantic, is robust and has been shown to be mostly driven by tropospheric processes (e.g. Mezzina et al. 2020, 2021a). In contrast, controversy still exists concerning the eastern part of the signal, located over the European continent, since disagreement is present in both observations (Fig.1 top) and models (Fig. 1, bottom), also depending on the methodology and season used. In some cases, a "wave-like" pattern with two anomalies of alternating sign over Europe is present (Fig. 1a, e.g. Toniazzo and Scaife 2006, Hardiman et al. 2019). In others, a pattern with a single anomaly, negative for El Niño (e.g. Fraedrich and Müller 1992), is visible, sometimes appearing as an extension of the mid-latitude lobe of the canonical dipole (Fig. 1d, e), sometimes as a detached center (Fig. 1b,c,f); hereafter, we will refer to this pattern as "semi-isolated". The semi-isolated pattern is usually accompanied by an upper-level anomaly of the same sign over northern Europe (e.g. Blackmon et al. 1983, Brönnimann 2007, Brönnimann et al. 2007, García-Serrano et al. 2011, Mezzina et al. 2020), but the relationship between the lower-level and upper-level signatures has not been settled, nor their overall nature, robustness and dynamics.

It is well-known that the dominant feature of the ENSO teleconnection to the NH extra-tropics is a large-scale tropospheric Rossby wave train emanating from the tropical Pacific and propagating at upper levels, with a first center of action over the Aleutian Low (cyclonic for El Niño), a second one of opposite sign over Canada, and finally, as it bends south-eastward, a tail over eastern North America (again cyclonic for El Niño; see Trenberth et al. 1998 for a review). The surface projection of this tail has been related to the western portion of the canonical dipole with a vertically-tilted structure (e.g. Mezzina et al. 2020, 2021a). Similarly, the signal over Europe may be related to this "main" wave train through a split occurring over northern North America, as suggested by García-Serrano et al. (2011) following theoretical considerations by Hoskins and Karoly (1981) and Karoly et al. (1989), or via reflection over eastern North America by zonal inhomogeneities in the background flow (e.g. Branstator 1983, 1985; Trenberth et al. 1998 and references therein). A secondary wave train is also a plausible hypothesis: Toniazzo and Scaife (2006) identified, for strong El Niños, a source region in the tropical Atlantic possibly emerging from the response of the Walker circulation (see also García-Serrano et al. 2017), and linked it to the wave-like pattern over Europe. Additional ENSO-related wave sources have also been detected over the Gulf of Mexico-Caribbean Sea region (e.g. Rodríguez-Fonseca et al. 2016, Fereday et al. 2018, Ayarzagüena et al. 2018, Hardiman et al. 2019), suggesting the presence of a third wave train. On the other hand, the semi-isolated pattern has been proposed to be linked to the downward propagation of ENSO anomalies from the polar stratosphere (e.g. Cagnazzo and Manzini 2009). While we acknowledge a possible role of the stratosphere (see Mezzina et al. 2021b), in this work we pursue a comprehensive understanding of the ENSO-NAE teleconnection in terms of tropospheric dynamics, which appear to dominate in the western North Atlantic.

We will explore potential paths for the tropospheric ENSO teleconnection to Europe and try to reconcile the different observed/simulated responses with the theoretical basis of linear Rossby wave propagation using a novel ray tracing approach. Ray tracing is a concept borrowed from geometrical optics to describe the propagation of

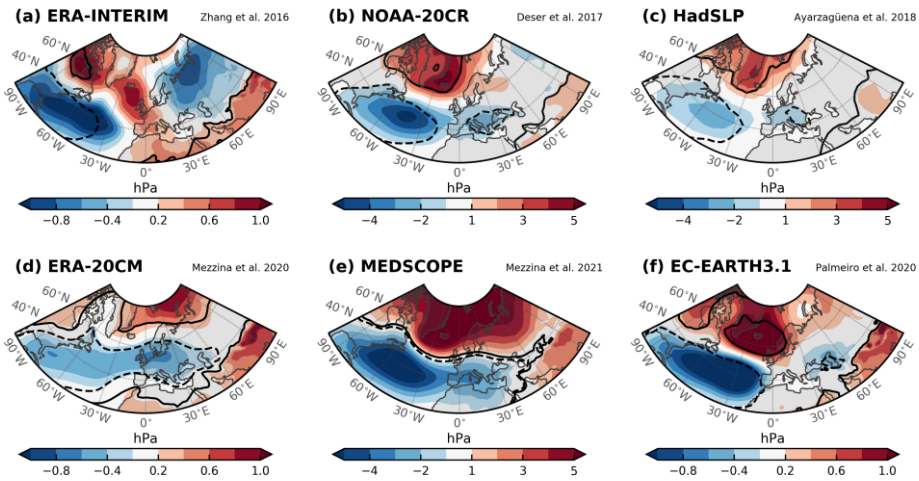

Figure 1: SLP anomalies associated with ENSO in several reanalyses (top) and models (bottom) reproduced from previous studies. (a) SLP×N3.4 (linear regression of SLP anomalies onto the Niño3.4-index), JFM, ERA-INTERIM, 1979–2014, as in Zhang et al. (2016) (b) EN–LN composites, DJF, NOAA-20CR, 1920–2013, as in Deser et al. (2017) (c) EN–LN composites, JF, HadSLP, 1873–2015, as in Ayarzagüena et al. (2018) (d) SLP×N3.4, JFM, ERA-20CM atmospheric model integrations, 1901–2010, as in Mezzina et al. (2020) (e) EN–LN experiments, JFM, MEDSCOPE multi-model mean (sensitivity experiments with El Niño- and La Niña-like SST forcing), as in Mezzina et al. (2021a) (f) SLP×N3.4, JFM, EC-EARTH3.1, 100-year coupled simulations as described in Palmeiro et al. (2020).

wave energy along "rays" aligned with the local group velocity. It was first consistently applied to atmospheric Rossby waves by Hoskins and Karoly (1981), who developed it in the framework of a zonally-symmetric basic state, a strong assumption to considerably simplify the equations. It was soon pointed out, however, that zonal asymmetries in the background flow, particularly those related to the local jets, can affect propagation by reflecting the wave trains (see Trenberth et al. 1998 for a review), but the extension of the theory to a "fully wavy" (i.e. in both zonal and meridional directions) mean flow is extremely complex (Karoly 1983). On the other hand, as noted by Branstator (1983), a longitudinally-varying flow can be viewed as a series of sub-regions in which the zonally-symmetric theory is locally valid, an argument used by Hoskins and Ambrizzi (1993) to qualitatively interpret results from a barotropic model with an observed mean state in terms of ray propagation. In this study, we have further extended this approach to develop a ray tracing algorithm that locally calculates the group velocity from a realistic, horizontally inhomogeneous flow, but in which reflection is treated similarly to the zonally-symmetric case. This approach, that is novel to the best of our knowledge, allows us to visually represent ray paths in a realistic flow, overcoming the limitations of using a strictly zonally-symmetric flow, albeit in a simplified manner.

We will consider outputs from two versions of the same state-of-the-art coupled model, both with a realistic mean flow, in which the ENSO response over Europe is different, and examine potential tropospheric pathways by using our ray-tracing approach and launching rays from several regions to test the various hypotheses related to the main and secondary wave trains. Our results may help understand the processes relevant for the ENSO teleconnection to the European continent and highlight which models' aspects need more attention in order for this teleconnection to be properly simulated and predicted (e.g. Dawson et al. 2011, Li et al. 2020).

2 Methods

2.1 Models, data and methods

We examine outputs from the CMIP5 historical runs (1850-2005, 3 members) of two versions of the MPI-ESM coupled model, with same horizontal resolution in the atmosphere (T63/1.9°), same top (0.01 hPa), but different vertical resolution: 47 levels in the low-resolution (LR) version and 95 in the mixed-resolution (MR) one (Giorgetta et al. 2013). Further details on the model, which has been long used as a seasonal forecast system, can be found in Baehr et al. (2015) and Domeisen et al. (2015) for LR, and Dobrynin et al. (2018) for MR. The forced ENSO response is estimated by computing the linearly detrended anomalies of the concatenated members and applying linear regression onto the Niño3.4 index (N3.4) obtained from sea surface temperature (SST). Results from the models are compared in Sect. 4 with observational ones using the NOAA-20CR reanalysis (Compo et al. 2011). January-to-March (JFM) is the target season. Statistical significance is assessed with a two-tailed t-test at the 95% confidence level.

2.2 "Hybrid" ray tracing

We consider large-scale, stationary Rossby waves and assume a constant zonal wavenumber k, as in the zonally-symmetric case (e.g. Hoskins and Ambrizzi 1993). The horizontal components of the group velocity, which determine the direction of the ray, are computed at each step from the climatological zonal wind $\overline{U}$ as:

$$c_x = \frac{2\beta^* k^2}{K_s^4} \qquad c_y = \frac{2\beta^* kl}{K_s^4} \tag{1}$$

where $\beta^* = \beta - \frac{\partial^2 \overline{U}}{\partial \overline{y}^2}$ is the meridional gradient of absolute vorticity, and $K_s^2 = k^2 + l^2 = \beta^*/\overline{U}$ is the total stationary wavenumber. Note that, for K_s to be real, positive β^* and $\overline{U}$ are required. Also, as observed by Hoskins and Karoly (1981), the slope of the ray is proportional to the meridional wavenumber l and inversely proportional to the zonal wavenumber k, so that shorter waves (larger k) are expected to have a more zonal trajectory (see also Hoskins and Ambrizzi 1993 for more details). In the case of a zonally-averaged $\overline{U}$, maps of l^2 (for a fixed k) would feature turning latitudes where $l^2 = 0$ that would act as barriers and reflect all the rays. However, when l^2 is computed from the full mean flow, 2D regions of negative l^2 appear, instead of simple turning latitudes (Figs. S1 and S2 in the Supplementary Material), and it is not straightforward to determine the trajectory of a ray approaching these "forbidden" areas. To overcome the problem, our hybrid approach consists in treating the forbidden regions as if they were local turning latitudes from

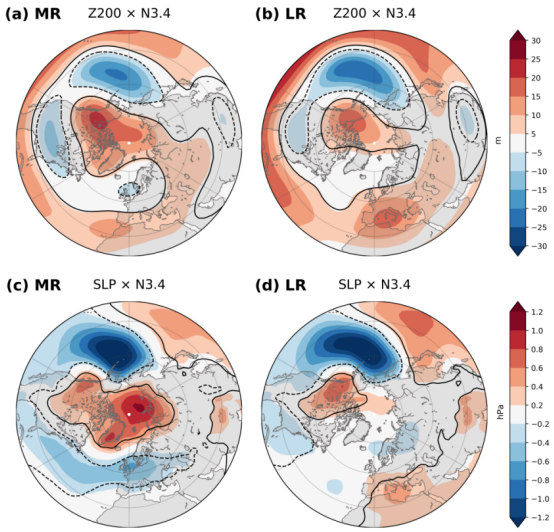

Figure 2: Linear regression onto N3.4 of 200-hPa geopotential height (top) and sea-level pressure (bottom) anomalies in the two model's versions: MR (left) and LR (right). JFM. Contours indicate statistically significant areas at the 95% confidence level.

the zonally-symmetric case. Namely, we build adjusted maps of positive l^2 by replacing point-by-point the negative values with the average from the nearest neighbors with $l^2 > 0$, and insert latitudinal – but zonally-asymmetric – barriers to roughly represent the original negative regions (for $k = 3$, compare the hatched regions and the thick horizontal lines in Fig. 4; see Fig. S1 for $k = 2, 4$). That is, a ray is free to propagate everywhere, with group velocity computed from the positively-adjusted l^2, until it eventually hits a barrier and undergoes total reflection (same angle of incidence). Despite its simplicity, this approach allows to bypass the unclear aspects of a ray entering an irregular region of negative l^2 , while maintaining some important aspects related to the zonal asymmetries (see Sect. 3.3). The basic state used in the analysis is the JFM climatology of the 200-hPa zonal wind smoothed with longitudinal running windows of 15°.

3 Results

3.1 Extra-tropical response

The deepening of the Aleutian Low related to the main wave train in the North Pacific is captured by both models (Fig. 2 bottom). In contrast, the SLP dipole over the North Atlantic is fully present only in MR (Fig. 2c), whereas in LR it is confined to North America, west of 60°W (Fig. 2d). Over the European continent, the extended negative lobe of the North Atlantic dipole dominates in MR (Fig. 2c), yielding an semi-isolated pattern, while in LR a more wave-like pattern is present, since a positive anomaly centered over the Mediterranean basin is accompanied by a weaker and non-significant anomaly of opposite sign over north-eastern Europe (Fig. 2d). This difference is partly reflected at upper levels, in the 200-hPa geopotential height (Z200; Fig. 2, top). The signal over Europe consists of a positive center of action over the Mediterranean in LR (Fig. 2b), which is also present in MR but shifted to the west and confined to lower latitudes (Fig. 2a). Moreover, a small but significant negative anomaly is evident over northern Europe in MR, roughly at the same location of the SLP anomaly (cf. Figs. 2a and 2c), as observed in previous studies (e.g. Blackmon et al. 1983, Brönnimann 2007, García-Serrano et al. 2011), suggesting a relationship between this upper-level center of action and the SLP semi-isolated pattern. In contrast, the upper-level response in the North Pacific and North Ameri-

ca/western North Atlantic regions differs very little between the two models (Fig. 2, top). In LR, it is slightly shifted westward, particularly the negative center over North America, which may explain why the SLP signal in the Atlantic is limited to the western part of the basin, assuming that the mid-latitude lobe of the canonical SLP dipole is related to the tail of the main wave train (e.g.Mezzina et al. 2020, 2021a).

These two versions of MPI-ESM constitute a good framework to investigate the reasons for the different ENSO signals reported over Europe, since they can be used to represent a more semi-isolated response, in the case of MR, or a wave-like pattern, in the case of LR.

3.2 Forcing, tropical response and mean flow

A distinct extra-tropical ENSO response in coupled simulations such as the ones examined could arise from variations in the oceanic forcing, but it does not appear to be the case here, since the SST patterns associated with the N3.4 are very similar (Fig. 3 bottom, shading). Likewise, the anomalous tropical upper-level divergence, represented by the 200-hPa velocity potential, is slightly stronger in LR (Fig. 3 bottom, contours) and is thus unlikely the cause for the different signal over Europe. Concerning a possible stratospheric influence, the ENSO response in the lower stratosphere is comparable in the two models (Fig. S3, bottom), which both show realistic anomalies in the 50-hPa geopotential height – although less significant in LR – that can be interpreted as a weakening and displacement of the polar vortex towards the North Atlantic sector (e.g. Mezzina et al. 2021b). Note also that the response in the middle-upper stratosphere (10 hPa) is less significant in MR (Fig. S3a), and not significant over the northern North Atlantic in either of the two models (Fig. S3, top). We thus also discard stratospheric processes as a main source of the MR/LR differences.

Alternatively, a different path for the tropospheric teleconnection is a reasonable hypothesis to explain the distinct surface response, since the propagation of large-scale stationary perturbations such as the main ENSO wave train is modulated by the atmospheric mean flow. Indeed, while both models show a realistic upper-level climatological zonal wind ($\overline{U}200$; Fig. 3a,b), they do exhibit some significant differences: in LR, the North Atlantic extra-tropical jet is more zonal and the subtropical jet is weaker, while the North Pacific jet is comparable, particularly over the western part of the basin (Fig. 3c). These differences in the zonal wind may alter the propagation of the tropospheric ENSO anomalies and lead to a different European response in MR and LR. In the next section, we will address this hypothesis with the ray tracing approach described in Sect. 2.2, considering various source regions.

3.3 Ray tracing results

For a fixed zonal wavenumber k, the meridional wavenumber l^2 computed from the full $\overline{U}$ displays some longitudinal differences between the two models, in particular concerning the forbidden regions ($l^2 < 0$) over the Mediterranean (Fig. 4, hatched regions, for $k = 3$; Fig. S1 for $k = 2, 4$ and for the full maps). In contrast, maps of l^2 obtained from the zonally-averaged $\overline{U}$ are rather

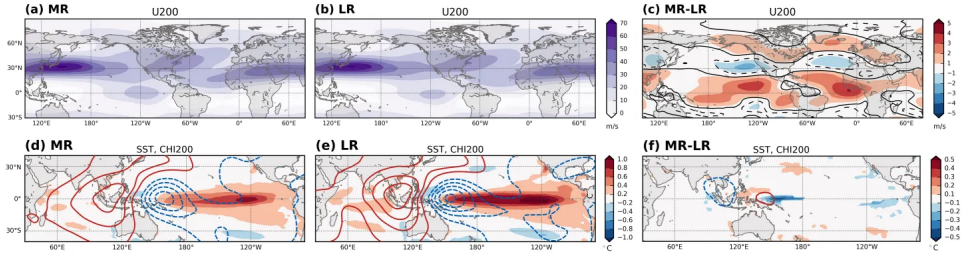

Figure 3: Top: 200-hPa zonal wind climatology in (a) MR (b) LR (c) MR-LR. Contours indicate statistically significant areas at the 95% confidence level. Bottom: linear regression onto N3.4 of SST (shading) and 200-hPa velocity potential (contours) anomalies in (d) MR (e) LR (f) MR–LR. Only statistically significant anomalies (95% confidence level) are plotted. All JFM.

similar (Fig. S2); hence, an approach that considers the longitudinally-varying flow is essential in this case. Using the "hybrid" ray tracing method, we now examine the pathways of large scale waves, with $k = 2, 3, 4$, from three key regions. These wavenumbers are chosen as they have been associated with tropical-extratropical teleconnections (e.g. Hoskins and Ambrizzi 1993), and correspond to the approximate longitudinal scale of the upper-level geopotential height anomalies.

3.3.1 Tropical Pacific (TP)

The main ENSO wave train is known to propagate towards higher latitudes with an eastward-arching route, reaching the western North Atlantic. Here, we consider the hypothesis of a mid-latitude split over North America, with part of the wave energy diverted to Europe rather than bending towards the North Atlantic (García-Serrano et al. 2011). Several source points in the central tropical Pacific have been selected (Fig. 4, top), none of which located west of the Date Line, as a region of negative l^2 in the western North Pacific would inhibit propagation after a few integration steps (see also Li et al. 2020). All rays are reflected at high latitudes, but at different longitudes and with different angles depending on the wavenumber, so that longer waves ($k = 2$, light green) roughly follow the arching structure of the main wave train, crossing Canada and reaching the western North Atlantic, while shorter waves ($k = 4$, dark green) bend at more eastern longitudes, around Greenland, and seem to reach Europe, with $k = 3$ (green) displaying an intermediate route. In principle, the main wave train should contain contributions from all these wavelengths, and the fact that the trajectories are rather similar

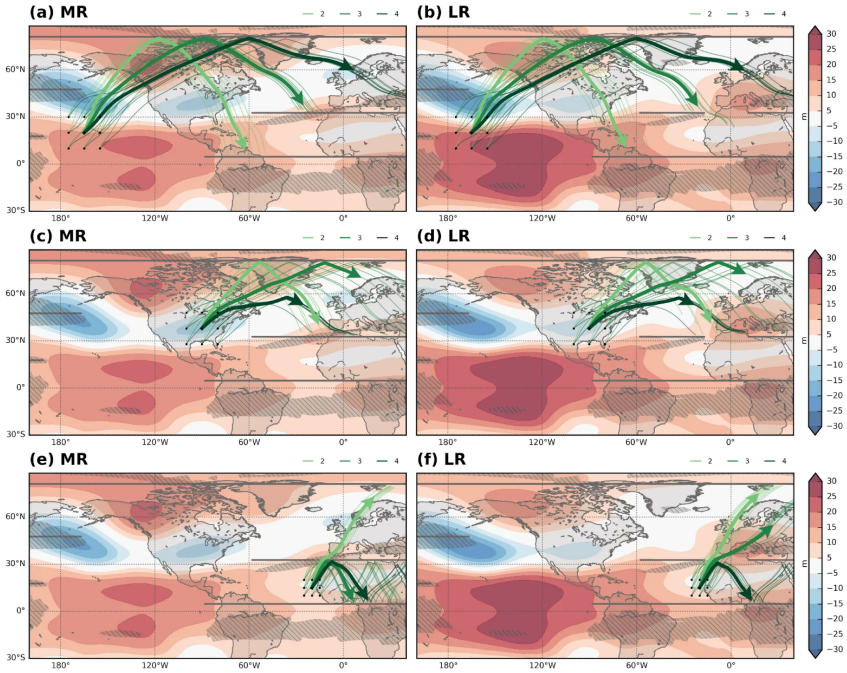

Figure 4: Ray paths for $k = 2$ (light green), 3 (green), 4 (dark green) in MR (left) and LR (right) from different source regions: TP (top), NANA (middle), TA (bottom). Central trajectories are plotted with thick arrows to indicate the mean propagating path of the envelope. Filled contours show the linear regression of 200-hPa geopotential height anomalies onto N3.4. Hatched regions indicate areas of negative l^2 for $k = 3$. Thick horizontal lines represent the "artificial" turning barriers for $k = 3$. Paths are truncated before second reflection, after leaving the domain or for display purposes (maximum: 20 days).

over the North Pacific/western North America but are well separated in the North Atlantic supports the possibility that a split such as that described by García-Serrano et al. (2011), who detected a bifurcation over eastern North America, could occur. Note also that, while there are no major differences between the rays in the two models, the smaller wavenumbers that are able to reach Europe ($k = 4$) are closer in scale to the negative center of action observed in MR at upper levels (Fig. 4a, shading) and less so to the positive anomaly in LR, which has a larger extension (Fig. 4b, shading), suggesting that this mechanism may be more relevant for the semi-isolated pattern.

3.3.2 North America/North Atlantic (NANA)

A series of launching points over western North America has been chosen to investigate the hypothesis of a secondary wave source over the Gulf of Mexico-Caribbean Sea region emerging from inter-basins effects, as proposed by Ayarzagüena et al. (2018) and Hardiman et al. (2019) (Fig. 4, middle). Rays launched from south of 30°N would propagate almost zonally due to the small values of l^2 (see Fig. S1) and end up trapped along the subtropical jet, hence the points have been distributed between 30°N and 50°N. Longer waves ($k = 2$, light green) propagate rather meridionally and turn equatorward at high latitudes, where they merge with shorter ones ($k = 4$, dark green) after reflection around 60°N. Although the end of the trajectories partially matches the location of the European anticyclone in LR, its amplitude is comparable to that of the high-latitude anomaly over Canada (15–20 m; Fig. 4d, shading). Such a relatively strong anomaly seems more likely to correspond to a wave train emitted by a closer source.

In contrast, it cannot be excluded that waves of intermediate size ($k = 3$, green) may be related to the negative anomaly appearing over northeastern Europe in MR (Fig. 4c). An alternative conjecture to that of a secondary wave train is that inhomogeneities in the basic state cause the main wave train to propagate through a wavier trajectory and experience a reflection (Branstator 1983, 1985,Trenberth et al. 1998) that is not captured by our simple approach.

3.3.3 Tropical Atlantic (TA)

The alternative secondary wave source suggested by Toniazzo and Scaife (2006) would be located in the tropical Atlantic. While they considered a source close to the Equator, we have chosen starting points at slightly higher latitudes, above the zonal barrier related to the equatorial easterlies (Fig. 4, bottom). The difference in the initial slope of the ray trajectories is less striking than in the previous cases, as all rays start with a quite meridional orientation. In both models, shorter waves ($k = 4$, dark green) are trapped in the subtropical jet, while longer ones ($k = 2$, light green) keep propagating towards high latitudes. Interestingly, intermediate waves ($k = 3$, green) are also trapped in the subtropics in MR (Fig. 4e), but not in LR (Fig. 4f), where, thanks to a discontinuity in the forbidden region, they propagate northwards. This difference in the propagation of $k = 3$ is consistent with the center of action of positive sign over the Mediterranean that dominates in LR, whose relatively strong amplitude also agrees well with a source in the TA, and which may cancel out a possible negative signal over Europe, explaining the difference in the two experiments.

4 Discussion and Conclusions

We have examined outputs from two models, MPI-ESM MR and LR, which represent examples where the surface ENSO signal over Europe is an semi-isolated and a wave-like pattern, respectively.

Based on our ray-tracing diagnostics, we suggest that the wave-like pattern is related to an upper-level anticyclone (for El Niño) over southern Europe belonging to a secondary wave train originating in the tropical Atlantic, which only reaches the region if the mean flow allows for the propagation of intermediate-scale ($k = 3$) waves. This is consistent with the results of Toniazzo and Scaife (2006), who identified a wave source in the tropical Atlantic linked to a wave-like response but did not specify the scale of the waves, nor did they provide further details on their ray tracing.

The semi-isolated pattern, in turn, seems to be linked to an upper-level negative anomaly (for El Niño) over northern Europe emerging from the split and/or reflection of the main wave train. This upper-level circulation associated with the semi-isolated pattern was already observed in very early studies, such as Blackmon et al. (1983), who forced an atmospheric model with perpetual El

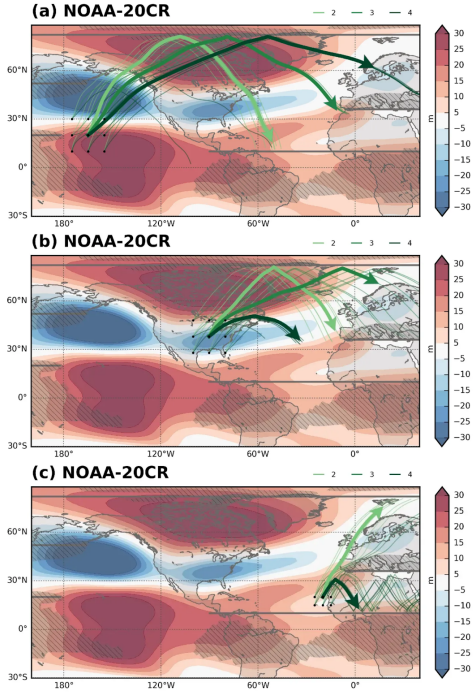

Figure 5: As in Fig. 4, but for NOAA-20CR. The bottom line of sources in Fig. 4 is discarded due to the higher latitudes of the Equatorial zonal barrier. The thick arrow is omitted for $k = 3$.

Niño January conditions. Branstator (1985) compared Blackmon et al.'s pattern to forced steady solutions of a linear barotropic model with different mean states and found that it was better reproduced when the total, zonally-asymmetric background flow was used: examining the distribution of normalized wavenumber vectors, he noticed a more meandering path in the energy propagation compared to the zonally-symmetric case, with a series of troughs and ridges crossing mid-latitudes and ultimately reaching Europe. That inhomogeneities in the background flow could be relevant for the propagation of the ENSO wave train to Europe is a hypothesis that was later reported in Trenberth et al. (1998)'s review (see their Fig. 8). We suggest that other regions previously suggested to play a role in the North Atlantic, such as the Gulf of Mexico-Caribbean Sea region (e.g. Ayarzagüena et al. 2018, Hardiman et al. 2019), may be interpreted in terms of this Branstator-type reflection, rather than being considered as sources of an additional wave train. Supporting this interpretation, note that the center of action over the western North Atlantic is usually weaker than that at subpolar latitudes, and its extension into North America at upper levels is upstream of these suggested wave sources. Our results are not conclusive regarding the Branstator-type reflection, since linear ray tracing does not identify a reflecting region, and further investigation is needed, possibly with the inclusion of non-linear effects.

Concerning the split hypothesis, it had been already noticed by Hoskins and Karoly (1981) that rays emanating from a source would follow different paths depending on the wavenumber and, as reported by Branstator (1983), "this dependence of propagation characteristics on wavenumber is manifested by a split in the energy as it disperses from the source". García-Serrano et al. (2011) returned to this idea in the context of the ENSO teleconnection to Europe in an effort to understand the semi-isolated pattern, since they had noticed, in their reanalysis dataset (ERA40), the

presence of the corresponding (negative) upper-level anomaly. They tested the hypothesis by computing the anomalous wave activity flux, as in Karoly et al. (1989), and observed two branches separating over eastern North America: one bending equatorward as the wave train tail, the other proceeding towards the North Atlantic and turning equatorwards later, around eastern Europe. Our results support this hypothesis by indicating that the first part of the main wave train path, from the tropical Pacific to Canada, is similar for all the wavenumbers considered, but a split may occur later, with shorter waves (i.e. larger wavenumbers) indeed reaching Europe. The split is potentially present in both of the models discussed here, but the approximate $k = 4$ scale of the semi-isolated anomaly over Europe in MR suggests that this pathway is more likely related to this type of response, as García-Serrano et al. (2011) speculated, rather than to the wave-like pattern.

Our modeling results are consistent with those obtained using the NOAA-20CR reanalysis over 1901-2014. The ENSO surface response in this dataset resembles the semi-isolated pattern (Fig. 1b for DJF; see Mezzina et al. 2020 for JFM), and the upper-level response is the expected same-signed anomaly over northern Europe (Fig. 5, shading). The ray trajectories are similar to those found in the models (see also Fig. S4 for l^2) and again support the split hypothesis (Fig. 5a) and endorse the possibility of Branstator-type reflection of the main wave train over North America (Fig. 5b). However, mixed results are found when considering sources in the tropical Atlantic, although the overall trajectories are similar to the ones in the models. All rays with $k = 2$ (light green) are propagating towards Europe, and all those with $k = 4$ (dark green) are reflected equatorward, but for $k = 3$ (green) both options occur, with the rays equally distributed (3 out of 6 are reflected). These results suggest that in the real world the wave source in the tropical Atlantic is effective in triggering a secondary wave train, but the amount of energy reaching Europe and its competition with the main wave train determine the observed signal.

We finally stress that the "hybrid" ray tracing approach used here is not strictly valid and caution is advised in the interpretation of the results. Despite that, we believe that it may constitute a valid tool for further applications beyond ENSO teleconnections, alternative or complementary to other diagnostics (e.g. Branstator 1985, García-Serrano et al. 2011, Benassi et al. 2021).

Acknowledgements

B.M. and J.G.-S. were supported by the "Contratos Predoctorales para la Formación de Doctores" (BES-2016-076431) and "Ramón y Cajal" (RYC-2016-21181) programmes, respectively. Technical support at BSC (Computational Earth Sciences group) is sincerely acknowledged.

References

Ayarzagüena, B., Ineson, S., Dunstone, N. J., Baldwin, M. P., & Scaife, A. A. (2018). Intraseasonal Effects of El Niño–Southern Oscillation on North Atlantic Climate. *J. Clim.*, *31*(21), 8861–8873. https://doi.org/10.1175/JCLI-D-18-0097.1

Baehr, J., Fröhlich, K., Botzet, M., Domeisen, D. I. V., Kornblueh, L., Notz, D., Piontek, R., ... Müller, W. A. (2015). The prediction of surface temperature in the new seasonal prediction system based on the MPI-ESM coupled climate model. *Clim. Dyn.*, *44*(9), 2723–2735. https://doi.org/10.1007/s00382-014-2399-7

Benassi, M., Conti, G., Gualdi, S., Ruggieri, P., Materia, S., GarcGarcía-Serranoa-Serrano, J., Palmeiro, F. M., ... Ardilouze, C. (2021). El Niño teleconnection to the Euro-Mediterranean late-winter: the role of extratropical Pacific modulation. *Clim. Dyn.*, 1–21. https://doi.org/10.1007/s00382-021-05768-y

Blackmon, M. L., Geisler, J. E., & Pitcher, E. J. (1983). A General Circulation Model Study of January Climate Anomaly Patterns Associated with Interannual Variation of Equatorial Pacific Sea Surface Temperatures. *J. Atmos. Sci.*, *40*(6), 1410–1425. https://doi.org/10.1175/1520-0469(1983)040⟨1410:AGCMSO⟩2.0.CO;2

Branstator, G. (1983). Horizontal Energy propagation in a Barotropic Atmosphere with Meridional and Zonal Structure. *J. Atmos. Sci.*, *40*(7), 1689–1708. https://doi.org/10.1175/1520-0469(1983)040⟨1689:HEPIAB⟩2.0.CO;2

Branstator, G. (1985). Analysis of General Circulation Model Sea-Surface Temperature Anomaly Simulations Using a Linear Model. Part I: Forced Solutions. *J. Atmos. Sci.*, *42*(21), 2225–2241. https://doi.org/10.1175/1520-0469(1985)042⟨2225:AOGCMS⟩2.0.CO;2

Brönnimann, S., Xoplaki, E., Casty, C., Pauling, A., & Luterbacher, J. (2007). ENSO influence on Europe during the last centuries. *Clim. Dyn.*, *28*(2), 181–197. https://doi.org/10.1007/s00382-006-0175-z

Brönnimann, S. (2007). Impact of El Niño–Southern Oscillation on European climate. *Rev. Geophys.*, *45*(3). https://doi.org/10.1029/2006RG000199

Cagnazzo, C., & Manzini, E. (2009). Impact of the Stratosphere on the Winter Tropospheric Teleconnections between ENSO and the North Atlantic and European Region. *J. Clim.*, *22*(5), 1223–1238. https://doi.org/10.1175/2008JCLI2549.1

Compo, G. P., Whitaker, J. S., Sardeshmukh, P. D., Matsui, N., Allan, R. J., Yin, X., Gleason, B. E., ... Worley, S. J. (2011). The Twentieth Century Reanalysis Project. *Q. J. R. Meteorolog. Soc.*, *137*(654), 1–28. https://doi.org/10.1002/qj.776

Dawson, A., Matthews, A. J., & Stevens, D. P. (2011). Rossby wave dynamics of the North Pacific extratropical response to El Niño: importance of the basic state in coupled GCMs. *Clim. Dyn.*, *37*(1), 391–405. https://doi.org/10.1007/s00382-010-0854-7

Deser, C., Simpson, I. R., McKinnon, K. A., & Phillips, A. S. (2017). The Northern Hemisphere Extratropical Atmospheric Circulation Response to ENSO: How Well Do We Know It and How Do We Evaluate Models Accordingly? *J. Clim.*, *30*(13), 5059–5082. https://doi.org/10.1175/JCLI-D-16-0844.1

Dobrynin, M., Domeisen, D. I. V., Müller, W. A., Bell, L., Brune, S., Bunzel, F., Düsterhus, A., ... Baehr, J. (2018). Improved Teleconnection-Based Dynamical Seasonal Predictions of Boreal Winter. *Geophys. Res. Lett.*, *45*(8), 3605–3614. https://doi.org/10.1002/2018GL077209

Domeisen, D. I. V., Butler, A. H., Fröhlich, K., Bittner, M., Müller, W. A., & Baehr, J. (2015). Seasonal Predictability over Europe Arising from El Niño and Stratospheric Variability in the MPI-ESM Seasonal Prediction System. *J. Clim.*, *28*(1), 256–271. https://doi.org/10.1175/JCLI-D-14-00207.1

Fereday, D., Chadwick, R., Knight, J., & Scaife, A. A. (2018). Atmospheric Dynamics is the Largest Source of Uncertainty in Future Winter European Rainfall. *J. Clim.*, *31*(3), 963–977. https://doi.org/10.1175/JCLI-D-17-0048.1

Fraedrich, K., & Müller, K. (1992). Climate anomalies in Europe associated with ENSO extremes. *Int. J. Climatol.*, *12*(1), 25–31. https://doi.org/10.1002/joc.3370120104

García-Serrano, J., Cassou, C., Douville, H., Giannini, A., & Doblas-Reyes, F. J. (2017). Revisiting the ENSO Teleconnection to the Tropical North Atlantic. *J. Clim.*, *30*(17), 6945–6957. https://doi.org/10.1175/JCLI-D-16-0641.1

García-Serrano, J., Losada, T., & Rodríguez-Fonseca, B. (2011). Extratropical Atmospheric Response to the Atlantic Niño Decaying Phase. *J. Clim.*, *24*(6), 1613–1625. https://doi.org/10.1175/2010JCLI3640.1

Giorgetta, M. A., Jungclaus, J., Reick, C. H., Legutke, S., Bader, J., Böttinger, M., Brovkin, V., ... Stevens, B. (2013). Climate and carbon cycle changes from 1850 to 2100 in MPI-ESM simulations for the Coupled Model Intercomparison Project phase 5. *J. Adv. Model. Earth Syst.*, *5*(3), 572–597. https://doi.org/10.1002/jame.20038

Hardiman, S. C., Dunstone, N. J., Scaife, A. A., Smith, D. M., Ineson, S., Lim, J., & Fereday, D. (2019). The Impact of Strong El Niño and La Niña Events on the North Atlantic. *Geophys. Res. Lett.*, *46*(5), 2874–2883. https://doi.org/10.1029/2018GL081776

Hoskins, B. J., & Ambrizzi, T. (1993). Rossby Wave Propagation on a Realistic Longitudinally Varying Flow. *J. Atmos. Sci.*, *50*(12), 1661–1671. https://doi.org/10.1175/1520-0469(1993)050⟨1661:RWPOAR⟩2.0.CO;2

Hoskins, B. J., & Karoly, D. J. (1981). The Steady Linear Response of a Spherical Atmosphere to Thermal and Orographic Forcing. *J. Atmos. Sci.*, *38*(6), 1179–1196. https://doi.org/10.1175/1520-0469(1981)038⟨1179:TSLROA⟩2.0.CO;2

Karoly, D. J. (1983). Rossby wave propagation in a barotropic atmosphere. *Dyn. Atmos. Oceans*, *7*(2), 111–125. https://doi.org/10.1016/0377-0265(83)90013-1

Karoly, D. J., Plumb, R. A., & Ting, M. (1989). Examples of the Horizontal Propagation of Quasi-stationary Waves. *J. Atmos. Sci.*, *46*(18), 2802–2811. https://doi.org/10.1175/1520-0469(1989)046⟨2802:EOTHPO⟩2.0.CO;2

Li, R. K. K., Woollings, T., O'Reilly, C., & Scaife, A. A. (2020). Effect of the North Pacific Tropospheric Waveguide on the Fidelity of Model El Niño Teleconnections. *J. Clim.*, *33*(12), 5223–5237. https://doi.org/10.1175/JCLI-D-19-0156.1

Mezzina, B., García-Serrano, J., Bladé, I., & Kucharski, F. (2020). Dynamics of the ENSO Teleconnection and NAO Variability in the North Atlantic–European Late Winter. *J. Clim.*, *33*(3), 907–923. https://doi.org/10.1175/JCLI-D-19-0192.1

Mezzina, B., García-Serrano, J., Bladé, I., Palmeiro, F. M., Batté, L., Ardilouze, C., Benassi, M., & Gualdi, S. (2021a). Multi-model assessment of the late-winter extra-tropical response to El Niño and La Niña. *Clim. Dyn.*, 1–22. https://doi.org/10.1007/s00382-020-05415-y

Mezzina, B., Palmeiro, F. M., García-Serrano, J., Bladé, I., Batté, L., & Benassi, M. (2021b). Multi-model assessment of the late-winter stratospheric response to El Niño and La Niña. *Clim. Dyn.*, 1–21. https://doi.org/10.1007/s00382-021-05836-3

Palmeiro, F. M., García-Serrano, J., Bellprat, O., Bretonnière, P.-A., & Doblas-Reyes, F. J. (2020). Boreal winter stratospheric variability in EC-EARTH: High-Top versus Low-Top. *Clim. Dyn.*, *54*(5), 3135–3150. https://doi.org/10.1007/s00382-020-05162-0

Rodríguez-Fonseca, B., Suárez-Moreno, R., Ayarzagüena, B., López-Parages, J., Gómara, I., Villamayor, J., Mohino, E., ... Castaño-Tierno, A. (2016). A Review of ENSO Influence on the North Atlantic. A Non-Stationary Signal. *Atmosphere*, *7*(7), 87. https://doi.org/10.3390/atmos7070087

Toniazzo, T., & Scaife, A. A. (2006). The influence of ENSO on winter North Atlantic climate. *Geophys. Res. Lett.*, *33*(24). https://doi.org/10.1029/2006GL027881

Trenberth, K. E., Branstator, G. W., Karoly, D., Kumar, A., Lau, N.-C., & Ropelewski, C. (1998). Progress during TOGA in understanding and modeling global teleconnections associated with tropical sea surface temperatures. *J. Geophys. Res. Oceans*, *103*(C7), 14291–14324. https://doi.org/10.1029/97JC01444

Zhang, T., Hoerling, M. P., Perlwitz, J., & Xu, T. (2016). Forced Atmospheric Teleconnections during 1979–2014. *J. Clim.*, *29*(7), 2333–2357. https://doi.org/10.1175/JCLI-D-15-0226.1

5.1 Supplementary Material

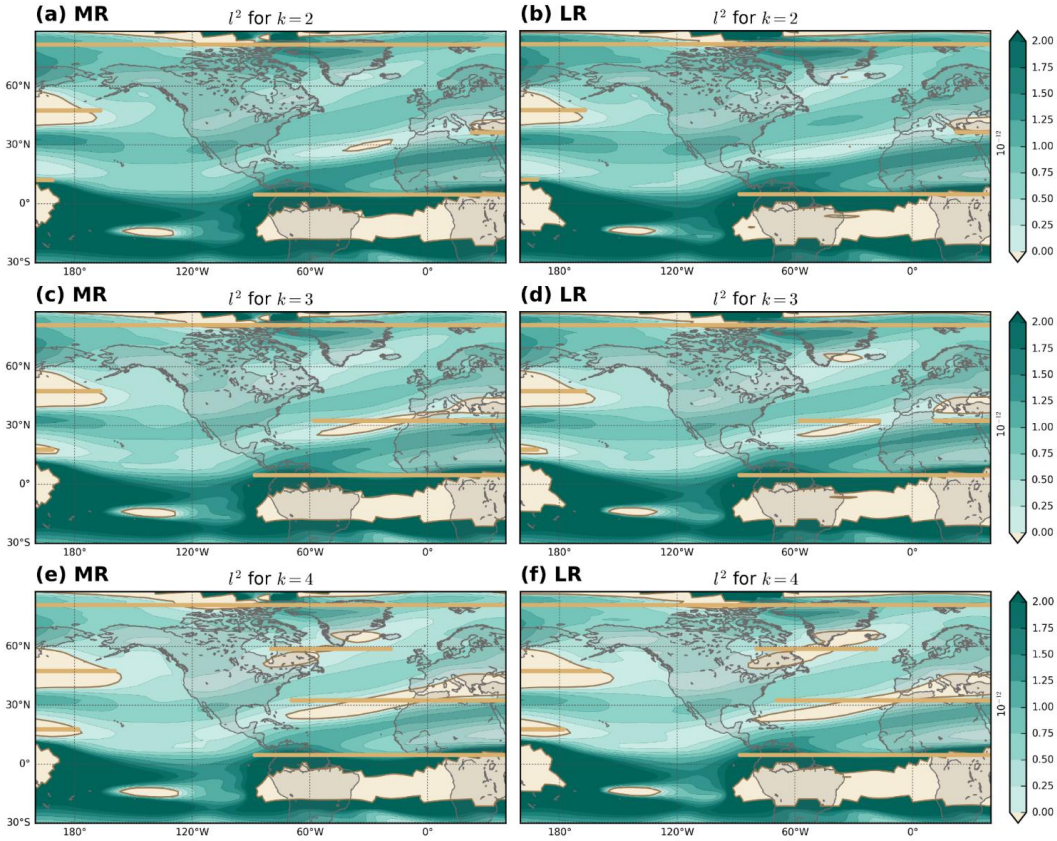

Figure S1. Meridional wave number squared (l^2) for a fixed zonal wave number *k*, computed from the total climatological zonal wind, in MR (left) and LR (right): *k=2* (top), *k=3* (middle), *k=4* (bottom). Units: m^{-2}. Thick horizontal lines represent the turning barriers built for the hybrid ray tracing.

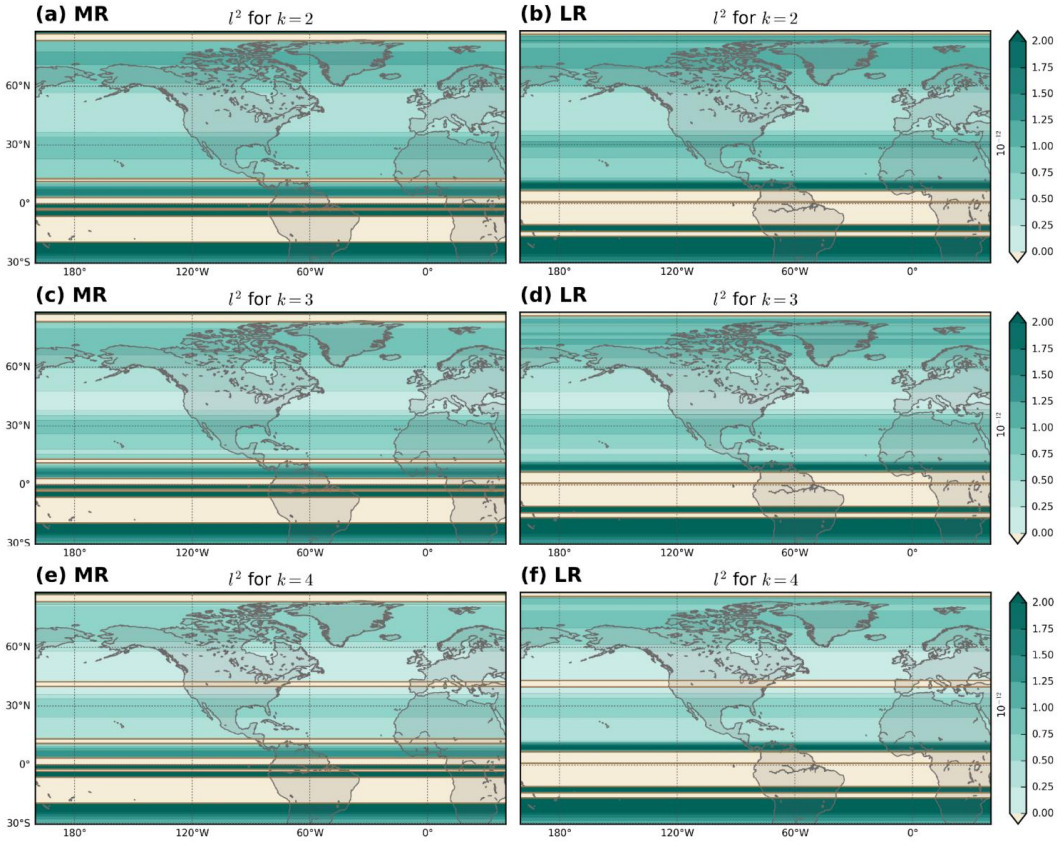

Figure S2. Meridional wave number squared (l^2) for a fixed zonal wave number *k*, computed from the total climatological zonal wind, in MR (left) and LR (right): *k=2* (top), *k=3* (middle), *k=4* (bottom). Units: m^{-2}.

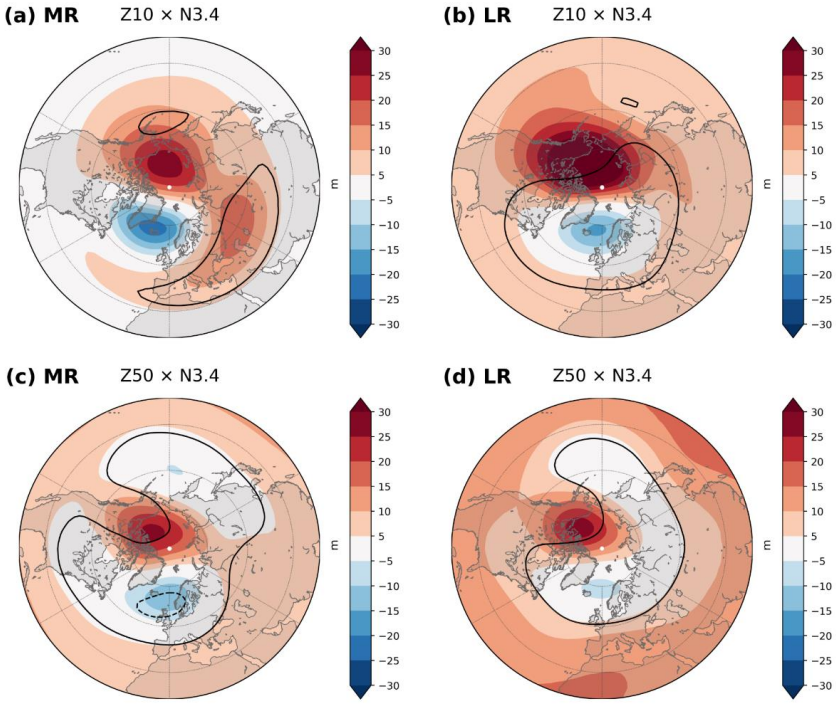

Figure S3. Linear regression onto N3.4 of 10-hPa geopotential height (top) and 50-hPa geopotential height (bottom) anomalies in the two model's versions: MR (left) and LR (right). JFM. Contours indicate statistically significant areas at the 95% confidence level.

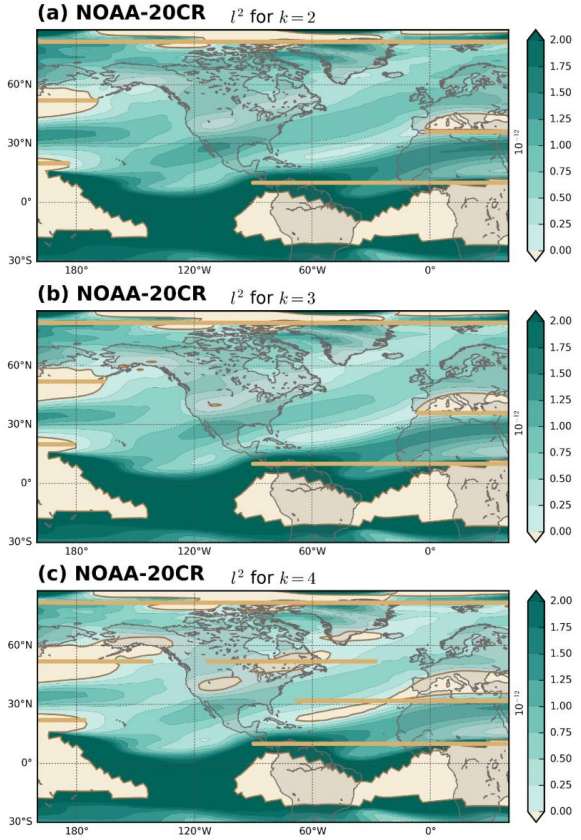

Figure S4. As in Fig. S1, but for NOAA-20CR.

Chapter 6

Conclusions

6.1 Summary of the main conclusions

The late-winter ENSO-NAE teleconnection has been deeply analyzed and the following conclusions have been drawn, one for each of the objectives listed in Sect.1.3:

1. The late-winter ENSO surface signal over the NAE region, the "canonical" SLP dipole between mid and high latitudes, is mostly driven by tropospheric dynamics.

   In particular, the mid-latitude lobe is primarily associated with the main Rossby wave train emanating from the tropical Pacific, whose tail is located over eastern North America at upper levels and, due to its westward tilt with height, projects on the SLP lobe in the North Atlantic at surface. Similarly, the other lobe at high latitudes is suggested to be linked to the second center of action of this main wave train situated over Canada, although the downward influence of lower-stratospheric circulation anomalies over the polar cap cannot be fully excluded.

2. The late-winter ENSO-NAE teleconnection is mostly unrelated to NAO variability, with different signatures, mechanisms and impacts in both the troposphere and stratosphere.

   While the ENSO teleconnection is dominated by the main Rossby wave train that crosses the North Pacific and North Atlantic, the NAO is a regional phenomenon that shows a hemispheric pattern linked to the zonal

propagation of disturbances into the jets, and its vertical structure in the North Atlantic is largely barotropic, with no westward tilt with height. Furthermore, transient-eddy dynamics is crucial for the internally-generated NAO variability, but appears to play a minor role in the ENSO-NAE teleconnection, which leads to different impacts in precipitation. In the stratosphere, the wavenumber-1 components related to ENSO and the NAO are almost in quadrature.

3. The tropospheric response to El Niño and La Niña in the North Pacific and NAE sector shows asymmetries in terms of amplitude and location, but the underlying mechanisms driving the ENSO-NAE teleconnection are the same for the two phases.

   The response associated with La Niña is weaker and shifted to the west with respect to the one linked to El Niño, both in the upper-level centers of action of the main wave train and in the surface anomalies. The asymmetry is arising from the different response in tropical convection due to the different total SST field and its gradient. This is related to a different tropical upper-level divergence, whose interaction with the subtropical mean flow explains the extra-tropical asymmetries.

4. The El Niño signal in the northern extra-tropical stratosphere is a well-known warming and weakening of the polar vortex, and the response to La Niña is symmetric in structure but with smaller amplitude. In the middle-upper stratosphere, the response projects on a wavenumber-1 pattern for both El Niño and, more weakly, La Niña.

   The ENSO stratospheric response appears to be primarily driven by the upward propagation of the main tropospheric Rossby wave train, and the center of action over Canada in particular. The lower-level temperature anomalies can be explained in terms of relative vorticity and thermodynamical adjustment associated with this center of action. The lower-stratospheric anomalies propagate upwards to the middle-upper stratosphere with a predominant wavenumber-1 component and a westward tilt with height, indicating that wave-breaking is not associated with this response.

5. The surface ENSO signal over Europe tends to present two types of pattern, which can be linked to two main potential tropospheric pathways: from the tropical Pacific and from the tropical Atlantic. The predominance of one pathway with respect to the other determines the surface response.

A wave-like pattern, with two SLP anomalies of opposite sign over Europe, is related to a secondary wave train emanating from the tropical Atlantic. The other type of response, with a single anomaly dominating over Europe, could be linked to the main wave train via a split over northern North America or via reflection due to inhomogeneities in the background flow.

6.2 Future perspectives

Several open questions concerning the late-winter ENSO-NAE teleconnection remain. The main points emerging from the previous chapters are reported here, with some insights for future research:

- As mentioned in Chapter 3, further work is needed to reconcile the tropical and extra-tropical responses linked to ENSO. In fact, the relationship between the extra-tropical main wave train, which is largely barotropic, and the tropical, mostly baroclinic, Gill-type response is not clear. Even the longitudinal shift of the main wave train between El Niño and La Niña (see conclusion 3 in Sect. 6.1) is not evident in the tropics, further questioning the relationship between the tropical and extra-tropical responses: whether they are part of the same large-scale structure may have to be revisited both theoretically and observationally.

- It has been shown in Chapters 2 and 3 that the canonical SLP dipole is mainly driven by tropospheric dynamics. However, the lower-stratospheric circulation anomalies over the polar cap, assessed in Chapter 4, may marginally contribute to the ENSO signal in the NAE region (see conclusion 1 in Sect. 6.1). This issue could be elucidated by comparing experiments with a stratosphere nudged to climatology and experiments with a free stratosphere, which would allow us to separate the stratospheric and tropospheric contributions to the ENSO-NAE signal.

- In Chapter 5, it is speculated that one of the possible pathways for the ENSO signal over the European continent may involve a reflection of the main wave train due to inhomogeneities in the mean flow (as suggested by Branstator 1983; see conclusion 5 in Sect. 6.1). This reflection is not detected by the linear approach used here, and the development of a more complex ray tracing method, possibly including non-linear effects, could help clarify this point.

– The ENSO tropospheric pathways to Europe identified in Chapter 5 in historical simulations and reanalyses should be analyzed in seasonal forecast systems, to assess their contribution to the models' predictive skill and determine which models' aspects (e.g. mean flow) are relevant for the teleconnection to be properly captured.

Bibliography

Bladé, I., Newman, M., Alexander, M. A., & Scott, J. D. (2008). The Late Fall Extratropical Response to ENSO: Sensitivity to Coupling and Convection in the Tropical West Pacific. *J. Clim.*, *21*(23), 6101–6118. https://doi.org/10.1175/2008JCLI1612.1

Branstator, G. (1983). Horizontal Energy propagation in a Barotropic Atmosphere with Meridional and Zonal Structure. *J. Atmos. Sci.*, *40*(7), 1689–1708. https://doi.org/10.1175/1520-0469(1983)040<1689:HEPIAB>2.0.CO;2

Brönnimann, S. (2007). Impact of El Niño–Southern Oscillation on European climate. *Rev. Geophys.*, *45*(3). https://doi.org/10.1029/2006RG000199

Capotondi, A., Wittenberg, A. T., Newman, M., Di Lorenzo, E., Yu, J.-Y., Braconnot, P., Cole, J., … Yeh, S.-W. (2015). Understanding ENSO Diversity. *Bull. Am. Meteorol. Soc.*, *96*(6), 921–938. https://doi.org/10.1175/BAMS-D-13-00117.1

Domeisen, D. I. V., Garfinkel, C. I., & Butler, A. H. (2019). The Teleconnection of El Niño Southern Oscillation to the Stratosphere. *Rev. Geophys.*, *57*(1), 5–47. https://doi.org/10.1029/2018RG000596

Hoerling, M. P., Kumar, A., & Xu, T. (2001). Robustness of the Nonlinear Climate Response to ENSO's Extreme Phases. *J. Clim.*, *14*(6), 1277–1293. https://doi.org/10.1175/1520-0442(2001)014<1277:ROTNCR>2.0.CO;2

Horel, J. D., & Wallace, J. M. (1981). Planetary-Scale Atmospheric Phenomena Associated with the Southern Oscillation. *Mon. Weather Rev.*, *109*(4), 813–829. https://doi.org/10.1175/1520-0493(1981)109<0813:PSAPAW>2.0.CO;2

Hoskins, B. J., & Karoly, D. J. (1981). The Steady Linear Response of a Spherical Atmosphere to Thermal and Orographic Forcing. *J. Atmos. Sci.*, *38*(6), 1179–1196. https://doi.org/10.1175/1520-0469(1981)038<1179:TSLROA>2.0.CO;2

Hurrell, J. W., & Deser, C. (2009). North Atlantic climate variability: The role of the North Atlantic Oscillation. *J. Mar. Syst.*, *78*(1), 28–41. https://doi.org/10.1016/j.jmarsys.2008.11.026

King, M. P., Herceg-Bulić, I., Bladé, I., García-Serrano, J., Keenlyside, N., Kucharski, F., Li, C., & Sobolowski, S. (2018). Importance of Late Fall ENSO Teleconnection

in the Euro-Atlantic Sector. *Bull. Am. Meteorol. Soc.*, *99*(7), 1337–1343. https://doi.org/10.1175/BAMS-D-17-0020.1

Mezzina, B., García-Serrano, J., Ambrizzi, T., Matei, D., Manzini, E., & Bladé, I. (2022). Tropospheric pathways of the late-winter ENSO teleconnection to Europe. *Submitted to Environ. Res. Lett.*

Mezzina, B., García-Serrano, J., Bladé, I., & Kucharski, F. (2020). Dynamics of the ENSO Teleconnection and NAO Variability in the North Atlantic–European Late Winter. *J. Clim.*, *33*(3), 907–923. https://doi.org/10.1175/JCLI-D-19-0192.1

Mezzina, B., García-Serrano, J., Bladé, I., Palmeiro, F. M., Batté, L., Ardilouze, C., Benassi, M., & Gualdi, S. (2021a). Multi-model assessment of the late-winter extra-tropical response to El Niño and La Niña. *Clim. Dyn.*, 1–22. https://doi.org/10.1007/s00382-020-05415-y

Mezzina, B., Palmeiro, F. M., García-Serrano, J., Bladé, I., Batté, L., & Benassi, M. (2021b). Multi-model assessment of the late-winter stratospheric response to El Niño and La Niña. *Clim. Dyn.*, 1–21. https://doi.org/10.1007/s00382-021-05836-3

Nigam, S., & Baxter, S. (2015). General Circulation of the atmosphere| Teleconnections. *Encyclopedia of Atmospheric Sciences (Second Edition)* (pp. 90–109). Academic Press. https://doi.org/10.1016/B978-0-12-382225-3.00400-X

Poli, P., Hersbach, H., Dee, D. P., Berrisford, P., Simmons, A. J., Vitart, F., Laloyaux, P., ... Fisher, M. (2016). ERA-20C: An Atmospheric Reanalysis of the Twentieth Century. *J. Clim.*, *29*(11), 4083–4097. https://doi.org/10.1175/JCLI-D-15-0556.1

Sardeshmukh, P. D., & Hoskins, B. J. (1988). The Generation of Global Rotational Flow by Steady Idealized Tropical Divergence. *J. Atmos. Sci.*, *45*(7), 1228–1251. https://doi.org/10.1175/1520-0469(1988)045<1228:TGOGRF>2.0.CO;2

Timmermann, A., An, S.-I., Kug, J.-S., Jin, F.-F., Cai, W., Capotondi, A., Cobb, K. M., ... Zhang, X. (2018). El Niño–Southern Oscillation complexity. *Nature*, *559*, 535–545. https://doi.org/10.1038/s41586-018-0252-6

Titchner, H. A., & Rayner, N. A. (2014). The Met Office Hadley Centre sea ice and sea surface temperature data set, version 2: 1. Sea ice concentrations. *J. Geophys. Res. Atmos.*, *119*(6), 2864–2889. https://doi.org/10.1002/2013JD020316

Trenberth, K. E., Branstator, G. W., Karoly, D., Kumar, A., Lau, N.-C., & Ropelewski, C. (1998). Progress during TOGA in understanding and modeling global teleconnections associated with tropical sea surface temperatures. *J. Geophys. Res. Oceans*, *103*(C7), 14291–14324. https://doi.org/10.1029/97JC01444

Acknowledgements

This PhD has been supported by the "Contratos Predoctorales para la Formación de Doctores" (BES-2016-076431) related to the DANAE project (CGL2015-68342-R) from the Ministerio de Economía y Competitividad. Most of the work has been carried out at the Barcelona Supercomputing Center (BSC), Earth Sciences Department. The work presented in Chapters 3 and 4 was supported by the MEDSCOPE project. MEDSCOPE is part of ERA4CS, an ERA-NET initiated by JPI Climate, and funded by AEMET (ES), ANR (FR), BSC (ES), CMCC (IT), CNR (IT), IMR (BE) and Meteo-France (FR), with co-funding by the European Union (Grant 690462). Part of the research in Chapter 5 has been developed at the Max Planck Institute for Meteorology (MPI-M). Some figures in Chapter 1 have been been designed using resources from Flaticon.com.

With little surprise, I first have to mention my advisors, Javi and Ileana. Thanks for guiding me through this PhD with infinite patience, for your constant support, and for all the invaluable teachings that go far beyond the pure scientific aspects. I consider myself very lucky.

Thanks to all the amazing – current or former – members of the Earth Sciences Department at BSC, which was a great environment to develop my research, both from the technical and personal points of view. I will always keep a great memory of this place.

I would also like to thank Daniela, Elisa and all the people at MPI-M for making my research visit an experience to treasure forever. I really hope to visit again, someday.

Finally, thanks to the co-authors of the research articles that are part of this thesis, for all your inputs and the inspiring discussions. I have learned something from each of you.

More Acknowledgements

Creo que tengo otra vez que mencionar a Javi, por ser mucho más que un director de tesis: un amigo, y una persona en la que siempre he podido confiar bajo cualquier punto de vista. Gracias por creer siempre en mí, por ayudarme en los momentos de crisis, por la paciencia en contestar a mis preguntas (y enseñarme que *there's no silly question*), y por el continuo estímulo científico e intelectual. No sé como debería ser el doctorado ideal, pero creo que has conseguido encontrar el justo balance entre acompañarme y dejarme caminar con mis propias piernas. Ahora, estoy lista para salir allí fuera... Bueno, casi. Gracias, de todo corazón.

Y, ya que estamos "en la UB", gracias a Froila, esta amiga imprescindible que te puede entender al 100%, que escucha y nunca juzga, y que siempre tiene una buena palabra para animarte. Nuestros viajes juntas serán de los recuerdos más bonitos de estos años, y espero hacer más en el futuro, a pesar de donde estemos. Gracias por todo, y mucha suerte.

Thanks to my fellow (PhD) students, those who welcomed me at the very beginning, and those who joined later: Bala, Vero, Jaume, Carlos, Cristina, Rubén, Lluís (V. and P.), Elisa, Dani, Vincenzo... It has always felt like being in a strange but very loving family, which I am definitely going to miss. Thanks for all the laughs together and for your support through good and bad times. And this seems like the right place to also thank Aude, it has been great having you around during the last year. Good luck to all of you!

Grazie ai compagni del Bar Sport, non solo per i caffé e le prelibatezze in esclusiva, ma per l'amicizia, le risate e i saggi consigli. Un ringraziamento speciale a Stella, il mio baluardo di normalità in questo anno e mezzo di pandemia: so che vomiterai a leggerlo, ma l'amicizia è solo un'altra forma di amore.

Gracias a todos los amigos que han enriquecido mi experiencia en Barcelona. A los Zombies de ayer y de hoy: me habéis alegrado cada maldito jueves durante casi cinco años. Y, claro, me habéis dado mucho más. Gracias por adoptar a esta niña tímida, os voy al llevar en el corazón. Gracias a Miriam, por su sincera y valiosa amistad durante todos estos años. Y gracias también a los amigos del Cor de Farmàcia por acogerme en ese grupo tanto bonito.

Grazie a Karin e Nico, dico sempre che siete "la mia famiglia di qui", e lo intendo sul serio: so che su di voi potrò sempre contare, e ve ne sono grata. Grazie alla pandemia e al mio condominio degli orrori per avermi fatto conoscere Aquiles, il vicino che tutti sognano e, soprattutto, un amico fidato. Grazie anche a Oriele, tra le prime persone ad accogliermi in questa città allora sconosciuta.

Grazie, ovviamente, anche a tutti gli amici lontani, ma solo geograficamente: a Monica, Anna, Irene e tutte le Babezzone del mio cuore; ad Edo, Anna e gli altri Fisici Che Vale la Pena Conoscere; ad Amanda e Laura, a Costanza, a Marco. Grazie per esserci sempre.

Infine, un grazie di cuore alla mia famiglia: a mia madre, mio padre e mio fratello. Grazie sopratutto per non aver mai, mai dubitato di me. Questa tesi è per voi.